In vivo dynamic contrast-enhanced magnetic resonance imaging and diffusion-weighted magnetic resonance imaging in treatment response monitoring of CWR22 prostate cancer xenografts in athymic mice following radiation therapy and androgen deprivation therapy

Alexander Kristian

Master of Physics

Submission date: 15th of August 2009

Supervisor: Dag Rune Olsen, University of Oslo, Institute for cancer research, Oslo University hospital

Co-supervisor: Kathrine Røe, Institute for cancer research, Oslo University hospital

University of Oslo

Faculty of Mathematics, Natural science and Technology

Physics Institute

Department of Biophysics and Medical Physics

Abstract

The goal of this project was to study the difference between CWR22 prostate cancer xenografts with full androgen supply and after undergoing androgen deprivation and/or radiation therapy in immunedeficient mice by applying the non-invasive visualization methods dynamic contrast-enhanced magnetic resonance imaging (DCE-MRI) and diffusion-weighted magnetic resonance imaging (DW-MRI).

The experiment consisted of 32 male mice (25-35g, 6-8 weeks) with subcutaneously implanted CWR22 xenografts randomized into 4 groups of 8 mice: mice with control and irradiated CWR22 xenografts (group 1 and 2) and castrated mice with control and irradiated CWR22CA xenografts (group 3 and 4). Mice in group 1 and 2 were included in the experiment when the tumors' shortest diameter reached 8 mm. Mice in group 3 and 4 were castrated when the shortest tumor diameter was 13 mm, and inclusion was made when the shortest diameter reached 8 mm. The day of inclusion is called day 0. MRI was performed at day 0, day 1 (24 h) and day 9. The imaging protocol included sequences for DW-MRI, proton density images, dynamic T1-weighted images (DCE-MRI) and T2-weighted images. The transfer constant K^{trans}, the extracellular extravascular volume, Ve, and the fraction of unfitted voxels were calculated from DCE-MRI data using Tofts and Kermode pharmacokinetic modeling. The mean apparent diffusion coefficient (ADC) was calculated from manually selected ROIs. Blood for PSA analysis was collected at all MRI days and at the last day of the experiment. The tumors in the irradiation groups were irradiated with a single fraction of 15 Gy after the baseline MRI at day 0. In group 1 and 2 mice were sacrificed when 2 of tumor in the group reached 16 mm in biggest diameter, in group 3 and 4 - 30 days after initial MRI. Additionally 8 mice with identical weight as the other mice in the experiment were used to obtain vascular input functions (VIFs) by imaging the left ventricle.

Exponentially growing CWR22 control tumors reached the endpoint of the experiment in 28 days, and irradiated CWR22 tumors in 69 days. The tumors in the CWR22 irradiated group showed a 31% volume decrease ($p<0.01$), before the regrowth started at day 41. At day 23 the mean tumor volume of irradiated tumors was 5.3-fold less ($p<0.01$) than the mean tumor volume of CWR22 control tumors. In the CWR22 groups, tumor volume decreased during the whole experiment, reaching a 47% ($p<0.01$) and 70% ($p<0.01$) reduction at day 26 for control and irradiation groups, respectively. The mice in the CWR22CA groups reached the experiment endpoint after 31±1 days after pre-treatment MRI.

Total PSA concentration for the CWR22 control group increased at all consecutive measurements, while the CWR22 irradiated group showed a plateau between day 1 and 9. The mice bearing CWR22CA tumors showed reduced total PSA concentration at all measurement days compared to CWR22 groups. The decrease in total PSA concentration from day 9 to the end-point of the experiment was significant for both the control and the irradiation group (63% decrease, $p < 0.01$ and 94 % decrease, $p = 0.01$, respectively). There was a significant positive correlation ($r=0.62$, $p<0.01$) between tumor volume and total PSA blood concentration. The correlation was stronger for animals with CWR22 tumors ($r = 0.73$, $p < 0.01$) than for animals with CWR22CA tumors ($r = 0.27$, $p =0.02$)

At day 0, K^{trans} of CWR22CA tumors was 47 % higher than of pre-radiation CWR22 tumors ($p = 0.01$). Androgen-ablated CWR22CA tumors showed no significant changes in K^{trans} following radiation, whereas K^{trans} in fully androgen supplied tumors decreased from day 0 to day 1 ($p = 0.01$), followed by an increase from day 1 to day 9 ($p < 0.01$). For the CWR22 irradiated group, a 42% increase ($p=0.03$) of Ve was observed at day 9 compared to pretreatment values. For the CWR22 irradiated group, the fraction of unfitted voxels showed a 211% increase ($p=0.01$) followed by a 57% decrease from day 1 to day 9 ($p=0.03$). A significant negative correlation between K^{trans} and the fraction of unfitted voxels for the CWR22 irradiated group ($r = -0.69$, $p < 0.01$), as well as using all tumors at all time points ($r = -0.62$, $p < 0.01$) was found

Using a b-value of 300 s/m^2, the CWR22 irradiated group showed a 39% ($p<0.01$) and 63% ($p<0.01$) increase in ADC at day 9 compared to pretreatment value and value at day 1, respectively. For b=600 s/m^2, the increase was 35% ($p=0.05$) and 58% ($p<0.01$).For both b-values at day 9, the ADC for the CWR22 irradiated group was 1.5-fold ($p<0.01$) and 1.6-fold ($p<0.01$) higher than for the CWR22 control group (b=300 s/m^2 and b=600 s/m^2 respectively). No significant changes in ADC values for CWR22CA control and irradiated groups were observed.

In conclusion, changes in vascularization, vessel permeability, surface area and volume fraction of EES as a result of androgen deprivation and/or radiation therapy were observed. Increase in ADC for CWR22 xenografts after radiation treatment suggest structural changes at the last day of observation. As a result of androgen deprivation CWR22 xenografts developed a radiation resistant phenotype. The study suggests that serial monitoring of K^{trans} could be a useful indicator of therapy responses in prostate cancer.

Preface

This report documents my work on my final master thesis at the Department of Biophysics and Medical physics, Institute of Physics, faculty of Mathematics, Natural Science and Technology, at the University of Oslo, autumn semester 2009.

The work was carried out at the Department of Radiation biology at Institute for cancer research, Oslo university hospital under the kind supervision of professor, PhD Dag Rune Olsen and M.Sc., PhD student Kathrine Røe. I would like to thank Dag Rune for his time and guidelines I received. I would like to thank Kathrine Røe for her valuable help with theses writing and experimental work, useful practical and theoretical guidance during the experiments.

I would like to thank Professor E. Paus and coworkers at Central Laboratory, Department of Medical Biochemistry, Oslo University Hospital, for technical assistance with PSA analysis, Professor F. Saatcioglu at Department of Molecular Biosciences, University of Oslo, for providing the CWR22 xenograft, Meng Yu Wang at Department of Tumor Biology, Oslo University Hospital, for help with interpretation of histology results, Therese Seierstad at Department of Radiation Biology, Oslo University Hospital for her suggestion during the experiment conduction.

Oslo, August 15, 2009

Alexander Kristian

Nomenclature

ADC - apparent diffusion coefficient

ADC map – a map showing parametric images containing the ADC

Adenocarcinoma – a cancer originating from glandular tissue

AIF – Arterial Input Function

Androgen – male sex hormones

AR - Androgen Receptor

Androgen deprivation therapy– a suppression of androgen production or utilizing of androgen by cells.

AUGC - Area Under Gadolinium Contrast concentration curve

Brachytherapy - delivery of radiation directly into the prostate

Cryosurgery – a surgery, where tissue destruction is made by extreme low temperature

CT – Computer Tomography

CWR22 – an androgen-dependent human prostate cancer xenograft

CWR22CA – an androgen-dependent human prostate cancer xenograft undergoing androgen deprivation therapy

DCE-MRI – Dynamic Contrast Enhanced Magnetic Resonance Imaging

DNA - Deoxyribonucleic Acid

DW-MRI – Diffusion Weighted Magnetic Resonance Imaging

EBRT - External Beam Radiotherapy

EPI – Echo Planar Imaging

EES - Extravascular Extracellular Space

Fraction of unfitted voxels – fraction of volume element that failed the approximation with a model

FID – Free Induction Decay

FOV – Field Of View

Gd-DTPA - Gadolinium DiethyleneTriaminePentaacetic Acid

Gleason score – quantitative characteristic of the cancer tissue appearance under microscopy

Gray – the SI unit of absorbed radiation dose due to ionizing radiation

HIFU - High-Intensity Focused Ultrasound

in vitro - the technique, where a procedure is performed outside a living organism. Cell experiments considered as in vitro

in vivo – the technique, where a procedure is performed in a living organism

K_{ep} - a transport constant describing backflux from EES to plasma

K^{trans} - a constant describing the transport of contrast agent from plasma into the EES

MVD - Microvessel Density

MRI – Magnetic Resonance Imaging

NMR - Nuclear Magnetic Resonance

Nude mice - is a mouse with absence of thymus, resulting in an inhibited immune system due to a reduced number of T cells

PSA – Prostate Specific Antigen

Radical Prostatectomy - surgical elimination of prostate

RF coil – a radiofrequent coil

ROI – Region Of Interest

SNR - Signal to Noise Ratio

SSFSE - Single Shot Fast Spin Echo

s.c. - subcutaneous

TRUS - Transrectal Ultrasound

VEGF - Vascular Endothelial Growth Factor

V_e – fraction of extravascular extracellular space in tissue volume

Xenograft – a transplanted cells, tissue or organs from one species to another, e.g. human tumor grown in mice

Contents

1. Introduction **10**

2. Theoretical Background **13**

2.1. Cancer – biology and clinic **13**
2.1.1 Cancer as disease 13
2.1.2. Cancer statistics 13
2.2. Prostate cancer **18**
2.2.1. Causes 18
2.2.2. Diagnosis 19
2.2.3. Prostate cancer angiogenesis 19
2.2.4. Prognostic factors in prostate cancer 20
2.2.5. Treatment of prostate cancer 22
2.2.5.1 Radical prostatectomy 22
2.2.5.2 Radiation therapy 23
2.2.5.3 External beam radiation therapy (EBRT) 25
2.2.5.4 Brachytherapy 25
2.2.5.5. Hormone therapy 25
2.2.5.6 Chemotherapy 26
2.2.5.7 Alternative treatment 26
2.2.6. Treatment strategy 27
2.3. Prostate cancer research models **29**
2.3.1. In vivo models 29
2.3.2. Xenograft models for prostate cancer 29
2.3.3. The orthotopic PC xenograft model 31
2.3.4. Tumor characteristics of PC xenografts 32
2.3.5 Androgen responsiveness in prostate cancer xenografts 32
2.3.6. CWR22 xenograft model 32
2.4 Magnetic resonance imaging **34**
2.4.1. Physics of magnetic resonance imaging 34
2.4.2. Dynamic contrast enhanced MRI 44
2.4.3. Diffusion-weighted MR Imaging 47

3. Materials and Methods **52**

3.1. Description of the experiment **52**
3.2. Substances used in experiment **53**
3.2.1. Anesthesia 53
3.2.2. Analgesia 53
3.2.3. Contrast agent 54
3.3. Animal model **54**
3.3.1. Mice 54
3.3.2. Xenografts 54
3.4. PSA analysis **54**
3.5. Radiation therapy **56**

3.6. MR **58**
3.6.1. Preparation for MR acquisition. 58
3.6.2. MRI acquisition 59
3.6.3 DCEMRI analysis 62
3.6.4 Diffusion analysis 64
3.7. Statistical analysis **64**

4. Results **65**

4.1 Animals used in experiment **65**
4.2. Tumor growth **65**
4.3 Histology **67**
4.4. PSA analysis **69**
4.5. DCEMRI results **74**
4.5.1. Qualitative assessment of DCEMRI 74
4.5.2. Quantitative results of DCEMRI 81
4.6 DW-MRI results **85**

5. Discussion **87**

5.1. Experimental Animals **87**
5.2. The xenograft **88**
5.3 Histology **89**
5.4. PSA **89**
5.5. Radiation **91**
5.6. MRI in cancer **91**
5.6.1 Dynamic contrast enhanced MRI. 91
5.6.2 DW-MRI and ADC 96

6. Conclusion and suggestions for further work **99**

7. References **101**

8. Appendix **114**

Chapter 1

Introduction

Prostate cancer is an adenocarcinoma of the prostate. The specific causes of its appearance remain unknown, but the risk factors are related to age, genetics and family history. Prostate cancer is responsible for 27% of new cases of cancer among men in Norway each year, being the most common type of cancer for men. In 2005, 3631 new cases were registered (Bray 2006). Norway is among the countries with the highest frequency and mortality rates of patients with prostate cancer. In some cases, especially in elderly patients, prostate cancer can be a moderate non-lethal disease that does not require treatment, but in other cases it is aggressive and lethal (Harris and Lohr 2002). The difficulty for clinicians is in deciding which men have fast-growing cancers that need advanced treatment and which have slow-growing cancers not requiring therapy. The clinical pattern of prostate cancer diagnosis has changed during the past few years. The proportion of men diagnosed at ages younger than 70 years has increased, as has the proportion of moderately differentiated tumors. These trends are consistent with the effect of increased use of screening. Thus, it is important to have reliable methods, preferably non-invasive, to determine the disease aggressiveness. A large number of patients and few reliable markers that predicts treatment response is a recurring challenge in the clinic.

Currently, treatment strategy for prostate cancer consists of, depending on disease stage and aggressivity, one or several of the following modalities: surgery (radical prostatectomy), radiation therapy (external beam radiotherapy or brachyterapy), hormone therapy or chemotherapy. In recent years some alternative treatment modalities like high-intensity ultrasound or cryosurgery have been suggested for patients, but the popularity of these methods is low. About 1/3 of all patients diagnosed with prostate cancer are included into curative treatment in form of surgery and/or radiation therapy. One third of all patients diagnosed with prostate cancer will die of it (Bray 2006). Thus, it is important to find a marker and determine the mechanisms in prostate cancer that have consequences for treatment effect. This knowledge will make it possible to tailor-made the treatment plan for each patient and, eventually, increase the survival.

The majority of primary diagnosed prostate cancer is androgen sensitive, requiring male sex hormones (androgens) to grow. By stopping the production of androgens or by blocking the androgen’s influence on cancer cells, the disease progression can be slowed down and the tumor burden reduced. This is called androgen deprivation therapy and can be done by medicaments or surgical castration. Androgen deprivation therapy alone cannot cure prostate cancer. Radiation therapy is another important modality in prostate cancer management. Combination of androgen deprivation therapy with radiation therapy improves local control and disease-free survival for prostate cancer patients as compared to radiation therapy alone (Lee 2006, Widmark et al 2009). For successful application of radiation treatment a non-invasive technique for localization of treatment volumes (tumor volume and safety margins) and volumes of risk is needed. Use of MRI, CT and ultrasound in planning and administration of intensity-modulated radiation therapy and high dose-rate brachytherapy has become a clinical standard.

After a period of 2 to 5 years, elevation of prostate specific antigen (PSA) concentration in blood shows an initial stage of prostate cancer relapse (Bruchovsky et al 1990, Trachtenberg 1987). The disease becomes hormone resistant and the cells will proliferate without androgen stimulation. The mechanisms involved in the early transition from androgen-dependent to androgen-independent prostate cancer are not fully understood. Today no curative treatment for patients with hormone resistant prostate cancer exists.

Angiogenesis is very important in prostate cancer progression. The angiogenic process is a complex multistep sequence involving many growth factors (cytokines) and interactions between varieties of cell types (Alonzi et al 2007). Expression of angiogenic cytokines in prostate cancer can be induced as a response to hypoxic stress or hormonal stimulation. The angiogenic process in prostate cancer is highly dependent on the vascular endothelial growth factor (VEGF). Androgens seem to regulate VEGF expression in prostate cancer cells and benign prostatic tissues (Joseph et al 1997).

One of the most promising non-invasive methods for imaging of viable tissue is functional magnetic resonance imaging (fMRI). In addition to obtain detailed anatomical images, MRI is increasingly being used to obtain biological information about vascularisation (dynamic contrast enhanced MRI) and molecular thermal motion (MR diffusion). These methods are promising in individualized, adaptive cancer treatment in the future.

Dynamic contrast enhanced magnetic resonance imaging (DCE-MRI) is a non-invasive technique implementing a series of MR-images before, during and after intravenous injection of contrast agent. Contrast agents administrated intravenously can enhance MR image contrast by altering the $T_{1,}$ T_2 and T_2^* relaxation times. Paramagnetic ions with a number of unpaired electrons such as Gd^{3+} and Mn^{2+} are used as contrast agents because of their high relaxivities. To reduce the toxicity of these ions for *in vivo* applications, they are chelated to special molecules. Gadolinium pentetate (Gd-DTPA), the currently most used MRI contrast agent, is a chelate composed of gadolinium ions and diethylenetriaminepentaacetic acid (DTPA). In tumor this low molecular weight contrast agent can leak through the capillary membrane into extravascular extracellular space EES, but it cannot penetrate into the cells. Signal enhancement is dependent on microvessel density, blood flow, vessel permeability and surface area. To monitor treatment response using DCE-MRI a quantitative pharmacokinetic Tofts and Kermode model can be applied (Tofts and Kermode 1991). It is a two-compartment model with a constant describing the transport of contrast agent from plasma into EES, K^{trans}, and a transport constant describing the backflux from EES to plasma, K_{ep}. This constants relates to each other as $K_{\mathrm{ep}}=K^{\mathrm{trans}}/\mathrm{V}_{\mathrm{e}}$, where V_{e} is the fraction of extravascular extracellular space in tissue volume. Advantages of the Tofts and Kermode model is that it utilizes a bolus injection, a theoretical expression that only has concentration of contrast agent in tissue as an unknown, and fits well to gradient echo data from both human tumors and transplanted tumors (Tofts 1997).

Diffusion weighted magnetic resonance imaging (DW-MRI) is a technique that visualizes water molecules motion in biological material. The diffusion signal is dependent on molecular viscosity and membrane permeability between intra- and extracellular compartments, active transport and flow, compartment shape and size (Moffat et al 2003, Kauppinen 2002). DW-MRI gives information about microstructure and can be used for detection of molecular and cellular treatment-related changes in tumor before the clinical parameters like reduction of tumor size can be observed. The majority of DW-MRI performed clinically is focusing on the extracellular water diffusion. In highly cellular tissues, such as tumors, extracellular water diffusion is restricted, leading to a short diffusion path and a reduced apparent diffusion coefficient (ADC). Cystic or necrotic portions of tumors have few structural barriers present and have a high ADC. ADC maps, derived from diffusion-weighted imaging, can therefore provide a non-invasive measure of cellularity (Herneth et al 2003), being a promising tool in diagnosis, treatment planning and monitoring.

One of the well established models in clinical experiments is the subcutaneous human xenograft (human tumor tissue implanted into an animal of other species) in immunodeficient mice (nude mice). It can be used to investigate biological and physiological properties of tumor tissue and to test treatments. The advantages of the model are easy establishment and manipulations of the tumor, positioning for imaging and obtaining of samples for histology. In addition, extrapolation of experimental data into clinical use is possible.

The CWR22 xenograft is an androgen-dependent, human prostatic carcinoma xenograft established from a transurethral resection and grown subcutaneously in male athymic nude mice (Pretlow et al 1993). The CWR22 xenograft was taken from a stage D, Gleason score 9, prostatic carcinoma with osseous metastases and was the first serially growing primary prostatic carcinoma (Pretlow et al 1993). Upon androgen withdrawal, CWR22 PSA mRNA and protein decrease rapidly, cells undergo apoptosis and tumors regress in size (Wainstein et al 1994, Gregory et al 1995). After several months they recur in the absence of testicular androgens in a manner characteristic of human androgen-independent prostate cancers (Wainstein et al 1994, Gregory et al 1995). Thus, the CWR22 model allows the study of tumor behavior in both androgen-dependent and -independent states. In nude mice bearing CWR22 xenografts, Wainstein et al (Wainstein et al 1994) observed that serum PSA concentrations correlated with tumor size and that blood levels of PSA decreased after androgen withdrawal.

The goal of this project was to study the difference between prostate cancer CWR22 xenografts with normal androgen supply and undergoing androgen deprivation treatment in immunodeficient mice by applying noninvasive visualization methods, like DCE-MRI and DW-MRI. The specific aim was to determine if tumor vasculature represented by K^{trans}, fraction of EES represented by Ve and tissue structure represented by ADC in prostate cancer xenografts with full androgen supply will change following androgen deprivation, and if it will affect the radiation response. It was investigated whether the functional MRI methods gave more information about treatment response than classical clinical marker for prostate cancer, like PSA and tumor volume.

Chapter 2

Theoretical Background

2.1. Cancer – biology and clinic

2.1.1. Cancer as disease

By definition of World Health Organization (WHO), cancer is a generic term for a large group of diseases that can affect any part of the body. One defining feature of cancer is the rapid creation of abnormal cells that grow beyond their usual boundaries, and which can invade adjoining normal tissue and spread to other organs through lymphatic channels or blood. This process is referred to as metastasis. Metastases are the major cause of death from cancer (WHO http://www.who.int/mediacentre/factsheets/fs297/en/).

2.1.2. Cancer statistics

Cancer is a major public health problem. Currently, one in 4 deaths in the United States is due to cancer (Jemal et al 2008). In Norway in 2006 it was 24488 incidences of cancer, of which 12903 occurred among men and 11585 among women. The four most common types are cancer of prostate, female breast, colon and lung, and they are responsible for half of the total cancer burden (12227 new cases). Cancer rates increase rapidly with age, and the vast majority in Norway, about 85% in men and 75% in women, occur in persons aged over 55 (Figure 2.1) (Bray 2006).

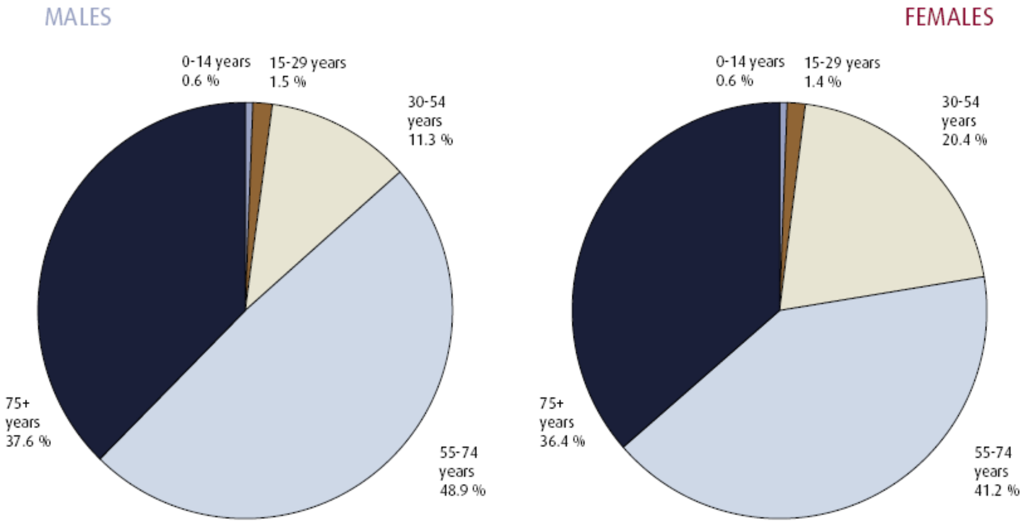

Figure 2.1. Percentage distribution of cancer incidences by age in Norway in 2002-2006 (Figure from Bray, 2006)

The relative impact of different types of cancer varies considerably with age. Figure 2.2 shows an age-related distribution of cancer types in Norway from 2002 to 2006, with prostate cancer being the type of cancer with the highest incidence for men over 55 years. The 2006 report from the Cancer Registry of Norway (Bray 2006) reveals a constant increase in new cases of prostate cancer. It also shows the rise in prostate cancer incidence since 1990, due to increased use of the prostate specific antigen (PSA) test, which became commercially available in 1989. A large proportion of the increasing burden can be attributed to demographic effects of population growth and ageing.

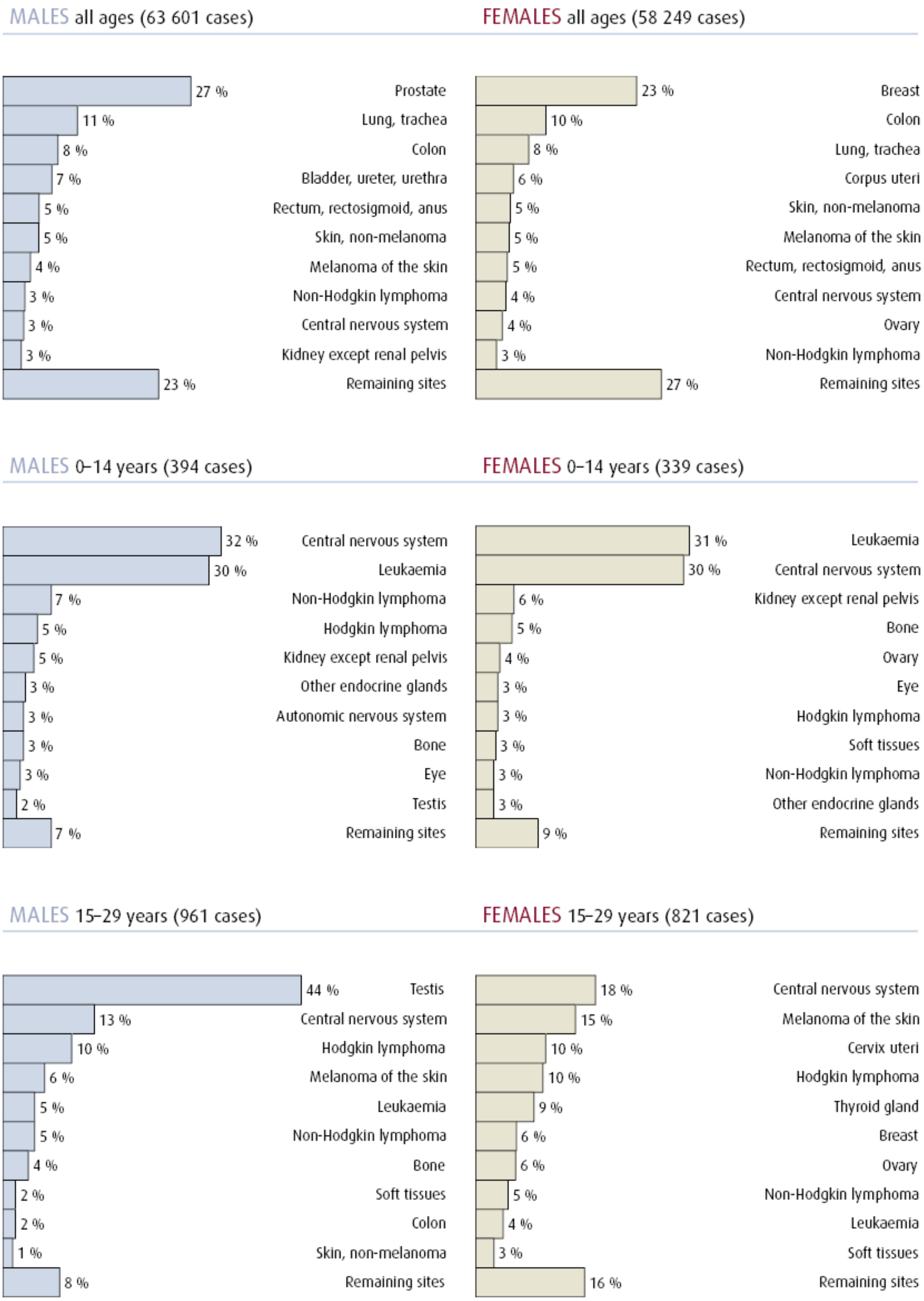

MALES all ages (63 601 cases)

FEMALES all ages (58 249 cases)

MALES 0–14 years (394 cases)

FEMALES 0–14 years (339 cases)

MALES 15–29 years (961 cases)

FEMALES 15–29 years (821 cases)

Table 2.2 Beginning, continues on next page

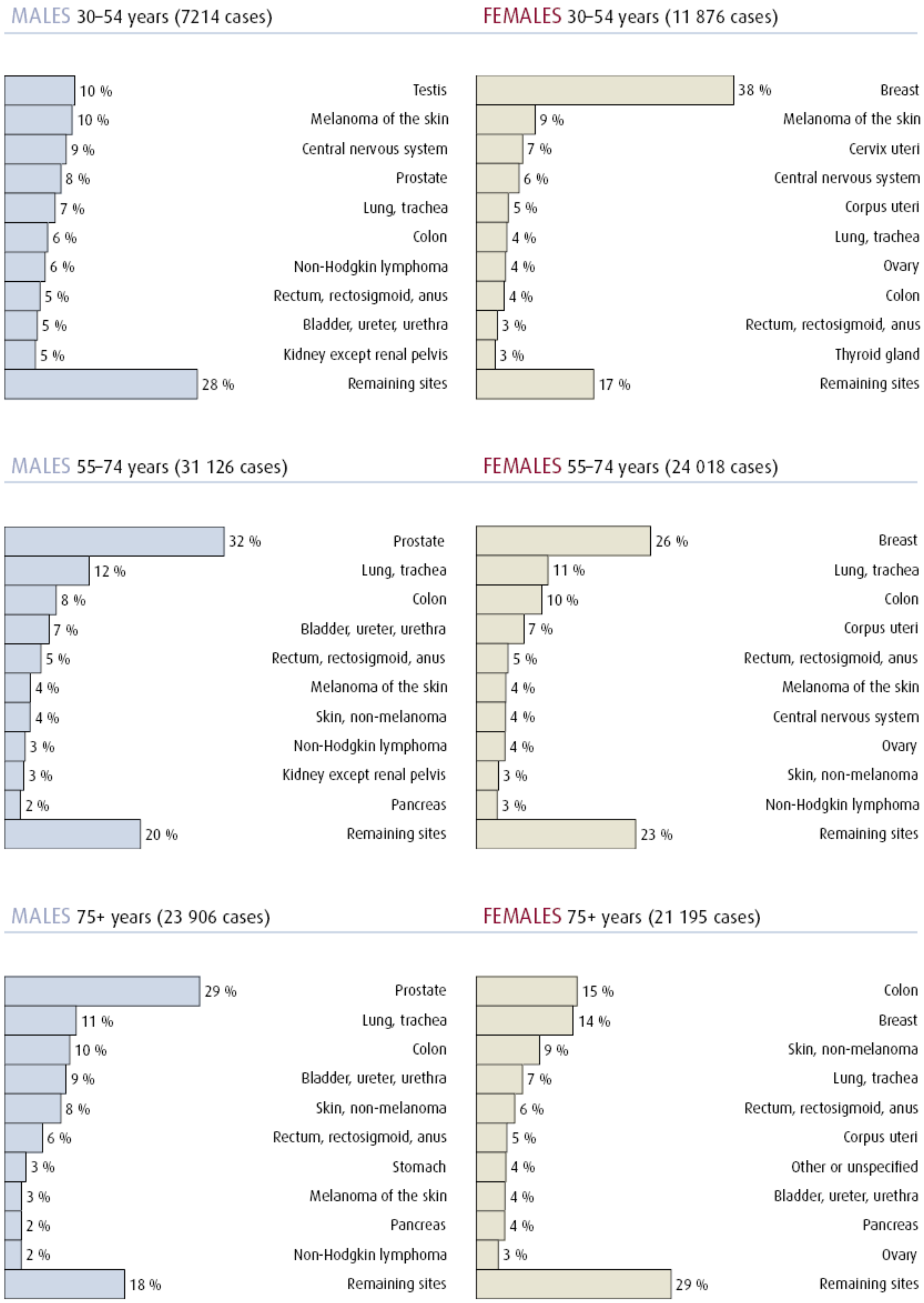

Figure 2.2. The most frequent incident cancers by age and sex in Norway in, 2002-2006 (Figure from Bray, 2006)

In 2004, there were 10489 cancer deaths in Norway, 5589 in men and 4900 in women. Lung (1174 deaths), colorectal (806 deaths), prostate (1074 deaths) and female breast cancer (694 deaths) were responsible for about half of the total cancer mortality burden (Bray 2006). Lung cancer is the leading cause of cancer death in both men and women (Figure 2.3).

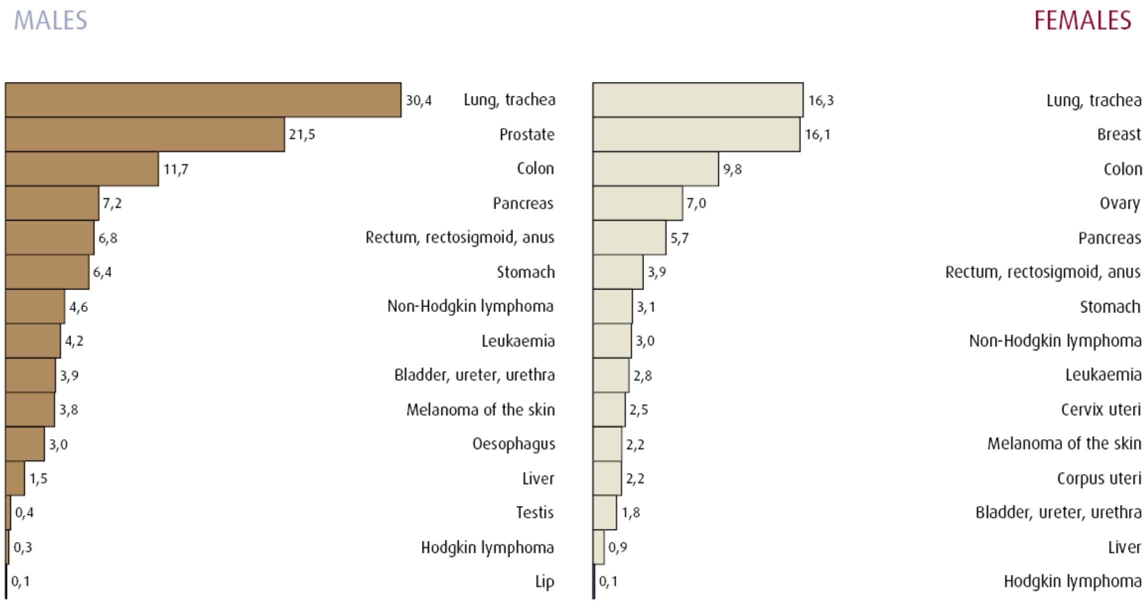

Figure 2.3. Age-standardized mortality rate in Norway 2004 for selected cancers (Figure from Statistics Norway, Bray 2006)

In men, there has been a steady increase in mortality rates of lung, prostate and colorectal cancer in Norway, since the 1970s. There is some evidence that resent mortality trends are more favorable for these cancer forms, with trends plateauing or beginning to decline (Bray 2006). In women, lung cancer mortality has been rising rapidly in the last decades relative to other cancers, but both breast and rectal cancer mortality rates have been decreasing. There are declines in mortality among younger population of several common cancers, including testicular cancer in men and leukemia in both sexes.

Overall survival five years after a cancer diagnosis was estimated to 57% and 63% for men and women, respectively. The five-year survival probabilities in Norway are shown in Figure 2.4. Survival probabilities in men have doubled from the late 1950s in men (Figure 2.5) and increased by 50% in women. Advances in cancer care, including the development of new treatment regimens and a multidisciplinary approach to cancer are contributors to this favorable trend.

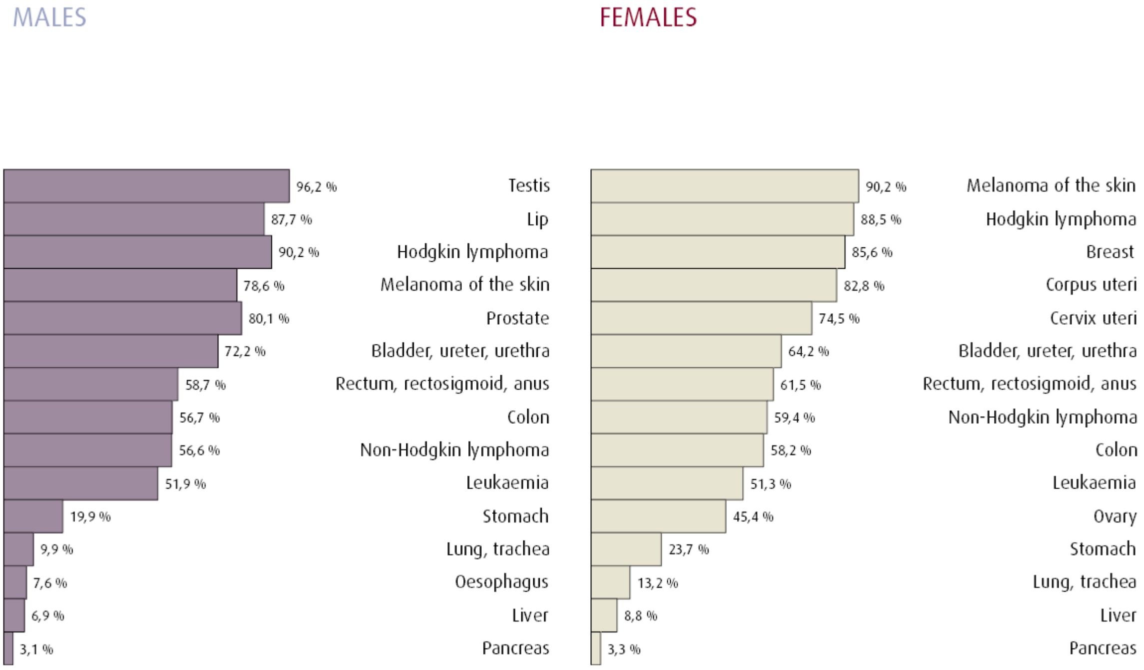

Figure 2.4. Five-year relative survival probabilities in Norway for selected cancers, diagnoses 1997-2001 (Figure from Bray, 2006)

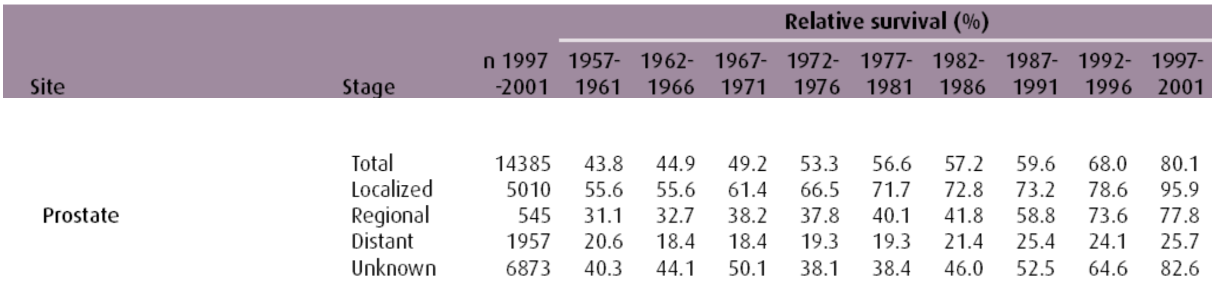

			Relative survival (%)								
Site	Stage	n 1997 -2001	1957-1961	1962-1966	1967-1971	1972-1976	1977-1981	1982-1986	1987-1991	1992-1996	1997-2001
Prostate	Total	14385	43.8	44.9	49.2	53.3	56.6	57.2	59.6	68.0	80.1
	Localized	5010	55.6	55.6	61.4	66.5	71.7	72.8	73.2	78.6	95.9
	Regional	545	31.1	32.7	38.2	37.8	40.1	41.8	58.8	73.6	77.8
	Distant	1957	20.6	18.4	18.4	19.3	19.3	21.4	25.4	24.1	25.7
	Unknown	6873	40.3	44.1	50.1	38.1	38.4	46.0	52.5	64.6	82.6

Figure 2.5 Five-year relative survival probabilities in Norway for prostate cancer in men (Table from Bray 2006)

2.2. Prostate cancer

2.2.1. Causes

Prostate cancer is an adenocarcinoma of prostate. The specific causes of prostate cancer remain unknown, but risk factors are related to age, genetics and family history. It is further reported that obesity, hormones, smoking, dietary factors, physical inactivity, occupation, vasectomy, genetic susceptibility and sexual factors are of importance (Hsing and Chokkalingam 2006).

Several studies have shown a familial aggregation of prostate cancer (Steinberg et al 1990, Cannon et al 1982, Grönberg et al 1996). A possible reason for this aggregation is inheritance of genes causing prostate cancer, some of which show high penetrance, whereas other genes show polymorphism and low penetrance. An important breakthrough in prostate cancer research was the finding of fusion oncogenes (Tomlins et al 2005).

The big difference in the incidence of prostate cancer between men in developed countries and in Asia is attributed to differences in lifestyles. Diet, pattern of sexual behavior, alcohol consumption and exposure to sun radiation are all important etiological factors (Kolonel et al 2004). The importance of nutritional factors for development of prostate cancer was noted in a Swedish study, in which both body-mass index and lean body mass were positively associated with the risk of prostate cancer, and were more strongly related to mortality than to incidence (Andersson et al 1997).

The relation between physical exercise and prostate cancer has been studied without any firm conclusions (Damber et al 2008). Smoking probably results in a small increase in the risk (Plaskon et al 2003), whereas the relation with alcohol consumption is unknown. The strong antioxidants lycopenes, found in tomatoes, have been studied as possible protective agents for the development of prostate cancer (Etminan e al 2004). Some other micronutrients and vitamins, such as selenium, vitamin E, and vitamin D, have been associated with decreased risk for prostate cancer (Duffield et al 2003, Dagnelie et al 2004, Hartman et al 1998).

2.2.2. Diagnosis

Prostate cancer frequently grows slowly and does not cause a problem (Harris and Lohr 2002). The difficulty for clinicians is in deciding which men have fast-growing cancers that need treatment and which have slow-growing cancers not requiring therapy. The clinical pattern of prostate cancer has changed during the past few years (Mettlin et al 1996). The proportion of men diagnosed at ages younger than 70 years has increased, as has the proportion of moderately differentiated tumors. These trends are consistent with the effect of increased use of screening.

Prostate cancer is diagnosed as localized or locally advanced. Diagnosis is based on examination of histopathological or cytological specimens from the gland (Hodge et al 1989). There is no accepted universal standard on how the samples should be taken (Aus et al 2005, Damber 2008). Staging of prostate cancer is mainly done on the basis of a digital rectal examination (Sobin and Wittekind 2002). Imaging modalities such as MRI and CT are currently not in wide-spread use in staging. Instead common clinical features, such as serum PSA concentration, tumour grade (Gleason score) of the biopsy, and stage from digital rectal examination, are used to establish the patient’s risk of having microscopic extracapsular extension of the tumour (Partin et al 2001, Ohori et al 2004) The risk that a prostate cancer will have metastasized is closely associated with a high serum PSA concentration, a locally advanced prostate cancer, or a poorly differentiated tumor (Aus et al 2005).

2.2.3. Prostate cancer angiogenesis

Angiogenesis involves a cascade of events in which mature, resting host endothelial cells are stimulated to proliferate, degrade their basement membranes and to form new blood vessels. The angiogenic process is a complex multistep sequence involving many growth factors (cytokines) and interactions between varieties of cell types (Alonzi et al 2007).

Expression of angiogenic cytokines in prostate cancer can be induced as a response to hypoxic stress or hormonal stimulation, but can also result from activation of oncogenes. The angiogenic process in prostate cancer is highly dependent on vascular endothelial growth factor (VEGF). It has been shown that VEGF is produced in abundance by the prostatic secretory epithelium of normal, hyperplasic, and tumor containing glands (Jackson et al 1997). The physiological roles of VEGF in the prostate are poorly understood and targets may include cells other than the vascular endothelium. Androgens seem to regulate VEGF expression in prostate cancer cells and benign prostatic tissues (Joseph et al 1997).

Increased microvessel density (MVD) is a potential prognostic factor that has been correlated with clinical and pathological stage, metastasis and histological grade in prostate cancer (Alonzi et al 2007). MVD has also been correlated with disease-specific survival and progression after treatment (Bettencourt et al 1998, Borre et al 1998, Hall et al 1994). MVD has not been shown to correlate consistently with outcome after radical prostatectomy (Rubin et al 1999).

2.2.4. Prognostic factors in prostate cancer

The most commonly used markers are PSA, stage (extent of the cancer within and beyond the prostate) and histopathological evaluation the biopsy, including Gleason score (appearance of the cancer tissue in a biopsy specimen).

Prostate specific antigen

The most well-known prognostic marker that has been used to assess prognosis (as well as detection of early increase) is prostate specific antigen (PSA). PSA is a 30 to 33 kDa (237 amino residue in mature form) belonging to the human tissue kallikrein family. It is a serine protease with a chymotrypsin-like activity (Diamandis et al 2000). PSA is mainly produced by the glandular epithelium of the prostate and secreted into the seminal fluid at high concentrations. PSA blood concentration, as a result of leakage from prostate gland is one million times lower than in seminal plasma. The biological role of PSA is the proteolytic cleavage of the gel-forming proteins of the seminal fluid to promote the release and motility of the sperms. (Christensson et al 1990, Lilja et al 1989) In serum, PSA detectable by immunochemical methods is predominantly found as a complex with alpha-1-antichymotrypsin (ACT). The free PSA represent about 5-30% of total immunoaccessible PSA in serum. A small amount of PSA complexed with other proteins is unavailable for immunochemical detection (Stenman et al 1991).

A large number of men are being diagnosed with early-stage prostate cancer as a result of the increased use of PSA screening (Hughes et al 2005). There is no proof that PSA screening in USA is the reason for reduced mortality (Mettlin 2000, Potosky et al 2001). But, in one non-randomized screening project in Tyrol, Austria, an early detection program along with free availability of treatment showed a 20% risk reduction in mortality (Oberaigner et al 2006).

Efforts have been made to find markers for early detection of prostate cancer, other than total serum PSA. In 2004, WHO arranged and international consultation to assess new markers (Stenman e al 2005). Despite total serum PSA still being the best marker, some urinary markers are being developed (Müller and Brenner 2006).

The change over time in the serum concentrations of PSA (PSA doubling time or PSA velocity) has shown promise in prediction of outcome in patients with non-metastatic prostate cancer. A high pre-treatment PSA velocity has been associated with a high risk of disease recurrence and death from prostate cancer (D'Amico et al 2005). A short PSA doubling time (i.e., a rapidly increasing PSA) after treatment is similarly associated with a poor prognosis (D'Amico et al 2003, Maffezini et al 2007).

Stage of disease

The TNM system is a cancer staging system describing the extent of cancer in the body. The system has existed for more than 50 years (Gospodarowicz et al 2003), and was last updated in 2002 (Sobin and Wittekind 2002). TNM is an abbreviation for the extent of primary tumor (T), regional lymph node involvement (N) and spread of distant metastasis (M). The TNM staging aid medical staff to plan and evaluate the treatment, give an indication of prognosis, and enable clinics in different countries to collate information.

Gleason score

Gleason score of a prostate cancer reports the histological grade based upon microscopic appearance of a biopsy. From microscopic analysis a grade is assigned to the most common tumor pattern, and a second grade to the next common tumor pattern. The two grades are added to get the Gleason score. For example, a most common pattern graded as 2 and a next common pattern graded as 3, reveals a Gleason score of 2 + 3 = 5. There are five possible tissue patterns (grades) with 1 being well differentiated (good prognosis) and 5 being poorly differentiated (poor prognosis). Thus, the Gleason score ranges from 2 to 10, with 10 having the worst prognosis.

Prognostic risk groups are now commonly used for patients with localized prostate cancer. These groups are usually based on pre-treatment variables such as TNM staging, serum PSA and biopsy grade or Gleason score. Table 2.1 shows a frequently used risk grouping (D'Amico et al 1998, Thompson et al 2007), being used to establish post-treatment outcome after various curative treatments. These clinical variables are also used as validated risk calculators for which the 5-year outcome after treatments can be related to each patient's clinical characteristics (risk factors).

Table 2.1. Risk group classification for localized prostate cancer (Damber 2008)

	Stage	PSA	Gleason score
Low risk	T1c to T2a	10 ng/ml or less	6 or less
Intermediate risk	T2b	10-20 ng/ml	7
High risk	T2c	20 ng/ml or greater	8 or greater

2.2.5. Treatment of prostate cancer

One third of those diagnosed with prostate cancer receives curative treatment including surgery and/or radiotherapy. Depending on the extension and aggressiveness of the disease the treatment is often extended with androgen deprivation and/or chemotherapy.

2.2.5.1 Radical prostatectomy

Radical perineal prostatectomy was first described in 1905 for the treatment of prostate cancer (Young 1905). In 1947, Millin described a retropubic approach for radical prostatectomy (Millin 1947). Both radical retropubic prostatectomy and radical perineal prostatectomy are associated with significant intraoperative and postoperative morbidity (Catalona and Scott 1986). Major complications included rectal injury, urethral injury, massive hemorrhage, pulmonary embolus, anastomotic leaks, lymphoceles, wound infections and incontinence. Virtually all men were rendered impotent. Therefore, many surgical candidates rather opted for radiation therapy because of the lower risk of erectile dysfunction.

Robotic prostatectomy (RP) represents the latest advancement in surgical treatment of prostate cancer, being a minimally invasive surgical approach augmented by robotic technology. Schuessler and colleagues (Schuessler et al 1997) first performed laparoscopic radical prostatectomy in 1991, but they failed to demonstrate advantages versus open prostatectomy, and the procedure was abandoned. It was not until Guillonneau and Vallancien (Guillonneau and Vallancien 2000) and Abbou and colleagues (Abbou et al 2000) described and validated their techniques of laparoscopic prostatectomy that interest resurged in minimally invasive surgical treatment of prostate cancer.

In a standard laparoscopic approach the instruments are controlled directly by the surgeon. The da Vinci® robot (Intuitive Surgical, Sunnyvale, CA, USA) is a master-slave robotic system consisting of a free-standing robotic tower and a remote console in which the surgeon sits at and controls the robotic arms.

2.2.5.2 Radiation therapy

(Based on Hall and Giacca (Hall and Giacca 2006) if else is not stated)

Radiation therapy is the medical use of ionizing radiation to control malignant cells by altering the genetic code in the deoxyribonucleic acid (DNA). The cell cycle consists of four phases: G_1 (first growth), S (synthesis), G_2 (second growth) and M (mitosis, cell division). These phases are characterized by the structure of the chromosomes, which contain the genetic material. During the cell cycle each DNA molecule is replicated into two identical daughter DNA molecules. A higher fraction of malignant cells are cycling in the cell cycle compared to normal cells. Normal cells are generally in the resting phase (G_0), continuously dividing to renew and replace cells. The damaging effect of radiation is most pronounced on proliferating cells and radiosensitvity describes how vulnerable a cell is to radiation damage. Cells in G_0 are resistant to ionizing radiation and damages to the normal cells cause side effects.

The therapeutic index is a comparison of the amount of radiation that causes the therapeutic effect to the amount that causes death. The balance of the therapeutic index is to ablate the tumor compartment with as limited impact as possible to the normal tissue. Therapies that either make the tumor more sensitive to radiation treatment or protect normal tissue from radiation therapy increase the therapeutic index.

Radiation therapy delivers lethal or sublethal damage to the tumor. Sublethal damage can be intrinsically repaired by cells. Many cell systems have limited or no capacity to repair sublethal events, while other compartments have significant capability of sublethal repair. Prostate cancer is thought to have a significant capacity to repair sublethal events (FritzGerald et al 2008). There exist treatment protocols that modify the environment for repair and convert sublethal treatment into lethal treatment.

The radiation response of normal cells and tumor cells are often described with a linear-quadratic cell survival model.

$$S = e^{-\alpha D - \beta D^2} \tag{2.1}$$

where S is the surviving fraction of cells, D is the radiation dose, and α and β is constants.

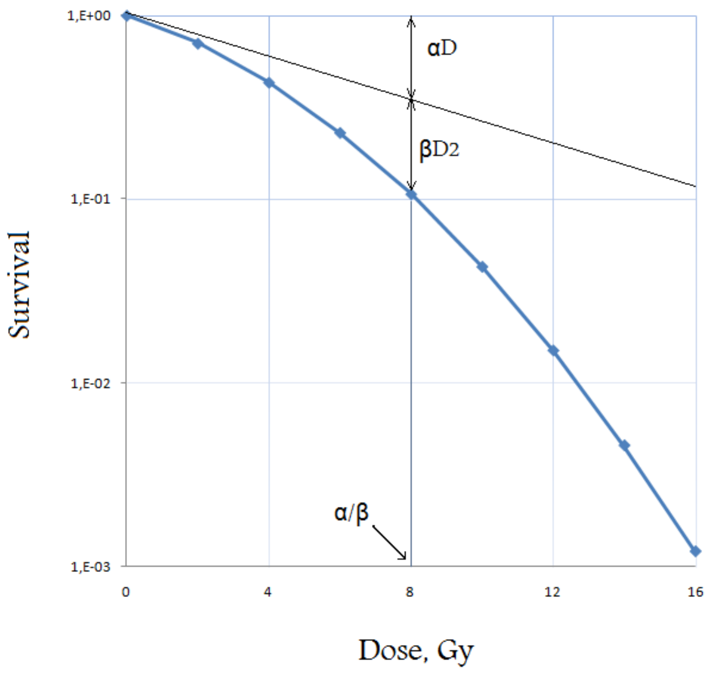

Figure 2.6. Cell survival curve representing the linear quadratic model. The dose at which the linear and quadratic components are equal is the ratio α/β (based on figure from Hall and Giacca (Hall and Giacca 2006)).

In Figure 2.6 cell death as function of radiation dose is displayed on a semi-log Y-axis with increasing dose on the X-axis since cell death is linear at low dose, and then exponential when the radiation dose increases. The α-component of cell death is the linear component and equals the logarithm of cell death per dose. The β component is the exponential phase and equals the logarithm of cell death per dose squared. The linear-quadratic model describes variances in normal tissue and tumor response to radiation therapy. The ratio of α to β is often used to describe the radiation response of cells. Prostate cancer cells are thought to have a low α/β ratio, which means that they have a more protracted response to radiation therapy and require a high radiation dose over an extended period of time to achieve complete cell death. The linear-quadratic model permits evaluation of therapies both *in vitro* and *in vivo* and determine which phase of cell death therapies influence. Sequential or combination therapies may be used as to influence either the α (linear) and/or the β (exponential) component, or both components simultaneously.

Certain tissues are extremely sensitive to radiation therapy and shows exponential cell death at low doses of radiation therapy. These have a high α-component in the cell-survival model. Bone marrow progenitors including granulocytes, macrophages and sperm are examples of cells sensitive to radiation therapy as these enter exponential cell death at low doses of radiation therapy. Most epithelial normal tissue and tumors demonstrate the described two phases of cell death in response to radiation exposure (FritzGerald et al 2008).

2.2.5.3 External beam radiation therapy (EBRT)

External beam radiotherapy (EBRT) uses high energy, typically 6 - 15 MeV, X-ray beams generated in a linear accelerator accurately targets the tumor volume. In the case of prostate cancer this will include the entire prostate gland with a margin and often also the seminal vesicles. The high energy X-rays cause cell death through DNA damage.

EBRT is suitable for treatment of localised prostate cancer. It can be combined with androgen deprivation treatment or chemotherapy. For low risk disease the prostate alone will be treated, for intermediate and high risk nodal and seminal vesicle may be involved.

CT based planning is used to reconstruct the treatment volume in three dimensions together with the organs at risk (rectum, bladder and femoral heads) before defining the beam sizes, angles and contributions using complex dosimetry algorithms. Three or four beams converging on the target are required for typical treatment of prostate cancer. The standard dose is 74 Gy, delivered in 2 Gy per fraction, daily Monday to Friday. In prostate cancer, the α/β ratio is estimated to be between 1.5 and 3.5, which is lower than other carcinoma types and favours hypo-fractionated regimes (dose larger than 2 Gy per fraction) (Moule and Hoskin 2009).

2.2.5.4 Brachytherapy

Brachytherapy is the delivery of radiation directly into the prostate. The greek word ‘brachy’ means ‘close’. Brachytherapy delivers a destructive dose to the tumor by implanting small radioactive seeds in the prostate, while minimizing rectal and urinary morbidity. Pasteau first reported insertion of a radium capsule per-urethra to irradiate prostate cancer in 1913 (Pasteau and De l’emploi 1919). The development of the transrectal ultrasound (TRUS) probe in Denmark in 1983 revolutionized brachytherapy. Using TRUS, accurate placement of the seeds in the prostate is achieved (Jamal et al 2008).

Currently, brachytherapy uses iodine-125 or, less often, palladium-103, seeds (Grimm et al 1994). Iodine-125, having a half-life of 60 days and a mean energy of 26 KeV, has been available since the 1970s, and palladium-103, having a half-life of 17 days and a mean energy of 21 KeV, since the 1980s. The biochemical disease survival is not different between these two isotopes, but the toxity of palladium resolve more quickly (Wallner et al 2002). A novel isotope, Cesium-131, has a very short half-life of only 9.7 days and mean energy of 29 KeV, delivering 90% of its therapeutic dose within 1 month. There is much interest in this isotope since the higher energy photon emission and shortened half-life may improve coverage of the prostate with fewer side effects (Jamal et al 2008).

2.2.5.5. Hormone therapy

Since the 1940s, androgen deprivation therapy has been a common treatment of prostate cancer, especially for metastatic stage of disease (Huggins and Hodges 1941). Testicular androgens are eliminated by surgical removal of the testicles, inhibition of pituitary secretion of luteinizing hormone or follicle-stimulating hormone by downregulation of gonadotropin-releasing hormone (GnRH) receptor with agonist and antagonist, or administration of estrogens to reduce the secretion of GnRH by the hypothalamus. The availability of GnRH agonists and non-steroidal antiandrogens from 1980s made immediate hormonal intervention more attractive for patients and clinicians. Although endocrine therapy is palliative and not biologically curative, increased uptake of this treatment could contribute to decline mortality rates by delaying death from prostate cancer long enough for the patients to die of unrelated causes (Damber 2004). After a 2 to 5 years period after hormone deprivation hormone-dependent prostate cancer can change into a hormone-refractory type. Intermittent androgen suppression take into account that malignant prostate cancer cells remain in a hormone-dependent stage longer than under continuous treatment, thus leading to extended survival (Bruchovsky et al 1990, Trachtenberg 1987).

2.2.5.6 Chemotherapy

Multiple clinical trials have not yet established the benefit from the cytotoxic effect of chemotherapy in prostate cancer. Angiogenesis and cell-cycle kinetic therapies may both interact with radiation therapy, and may become important targets for improving cell death. Signaling-pathway inhibitors and cell-adhesion modulators may also become important supplements to radiation therapy as it is evidenced that radiation therapy has a relationship with these agents (FitzGerald 2004).

2.2.5.7 Alternative treatment

High-intensity focused ultrasound (HIFU)

HIFU was first established in 1944 (Lynn and Putnam 1944), although it was 30 years before its first use in clinical practice (Madersbacher et al 1995). It involves high-intensity ultrasound waves focused on an area to cause tissue destruction due to the thermal effect and cavitation (Kennedy et al 2003). The thermal effect is due to absorption of ultrasound energy subsequently converted to heat, with temperatures of 70-100°C achieved within a few seconds. Cavitation occurs due to an interaction of ultrasound and microbubbles in the tissue, resulting in an oscillation of these bubbles and, thereby, tissue ablation. These processes result in coagulative necrosis of the tissue (Chapelon et al 1992). HIFU is used in treatment of organ-confined prostate cancer in patients not suitable for other treatments, either due to informed patient choice, comorbidity, or age (Rebillard et al 2003). HIFU can be repeated without maximum dosage constraints. The most common side-effects of HIFU include urinary retention and erectile dysfunction (Murat et al 2007).

Cryosurgery

In cryosurgery, cell death is obtained by direct cellular injury using cooled ultra-thin trans-perineal probes in the prostate (Jamal et al 2008). When temperature decreases, enzymatic paralysis results in cellular metabolic failure. Below -20°C, water in the intracellular environment crystallizes to ice, drawing fluid in from the extracellular environment and causing electrolyte imbalance. During the thawing phase, ice crystals coalesce and disrupt the cell membrane. Endothelial damage is the stimulus for platelet aggregation and microthrombs formation, leading to microcirculatory failure. The most frequently observed complication associated with cryotherapy is erectile dysfunction, occurring in approximately 90% of preoperatively potent patients (Chin et al 2007). The main concern with cryotherapy is the lack of data from randomized controlled trials and long-term follow-up.

2.2.6. Treatment strategy

Localized prostate cancer

Localized prostate cancer is the most commonly diagnosed stage. The choice of treatment (active monitoring, radical prostatectomy, or any type of radiotherapy) is based on tumor characteristics and the patient's life expectancy. It is recommended that men with a life expectancy of less than 10 years who have early-stage prostate cancer should be actively monitored as their first choice of treatment (Aus et al 2005) and that this approach is an option for all men in the low-risk group. Men with more poorly differentiated tumors and those with a long life expectancy are usually offered curative treatment. There is no cut-off limit for age when active therapy might be of value, thus clinicians have to define the individual patient's life expectancy. Even older men can benefit from curative treatment if they live long enough (Wong et al 2006). Of the treatments available, only radical prostatectomy has a survival advantage over watchful waiting.

For patients receiving EBRT, the American Urological Association has issued guidelines on prostate cancer (Table 2.2). Whether EBRT needs to be combined with hormonal therapy when used in patients with clinically localized disease is not clear, but there seems to be some benefit for the combination (Dearnalay et al 2007). Brachytherapy using iridium-192 can also be used for localized disease, either as monotherapy or in combination with EBRT (Pickles and Pollack 2006).

Table 2.2: American Urological Association's guidelines for treatment (Damber 2008)

Risk grade of disease	Therapy
Low	A radiation dose higher than 70 Gy might decrease the risk of PSA recurrence, but no difference in survival has been shown (Pollack et al 2002, Zietman et al 2005)
Intermediate	Conventional-dose radiotherapy of 70 Gy or less with the use of neoadjuvant and concurrent hormonal therapy for 6 months might extend survival of patients. Higher radiation doses might reduce the risk of PSA recurrence, but no difference in survival has been shown (Pollack et al 2002, Zietman et al 2005)
High	A combination of long-term hormonal therapy (up to 3 years) might extend survival compared with EBRT alone (D'Amico et al 2004, Bolle et al 2002)

Locally advanced prostate cancer

Some patients with extracapsular extension of the tumor can still be offered treatment with curative intent. Radiotherapy has long been the standard option for these men. Effectiveness of radiotherapy can be improved by increasing dose escalation to more than 70 Gy or combination of radiation with neoadjuvant- or adjuvant hormonal therapy. The use of short-term neoadjuvant hormonal therapy might result in improved biochemical control or local control and also in disease-specific survival. Longer periods of adjuvant hormonal therapy (up to 3 years after radiotherapy or indefinitely) will also result in an overall benefit in survival although benefit seems to be limited to patients with high Gleason scores (Aus et al 2005, Gerber et al 1997, Hsu et al 2007). Radical prostatectomy is in many cases not an option, because of the difficulties in obtaining free resection margins in patients who have extracapsular disease. Some patients with small tumors that extend outside the gland might still be candidates for surgery (Aus et al 2005, Hsu et al 2007).

Second-line treatment after failed primary surgery or radiotherapy

A rising serum PSA is often the first sign of treatment-failure, occurring months to years before clinical symptoms or radiographic signs of recurrent disease. The recurring disease is classified as local or systemic. Local failure is characterized by a late PSA increase (more than 12 months after primary treatment), a long PSA doubling time (a slow rise in PSA over time) and a not too aggressive disease at diagnosis. Systemic failure is expected for patients with early PSA increase, rapid PSA doubling time or adverse pathological change (Simmons et al 2007, Aus et al 2007). Most patients with local failure have a protracted course before clinical signs of disease recurrence become obvious, meaning that men with a remaining long life expectancy (5-10 years) can be offered a second curative treatment. After surgery such treatment is EBRT. Experimental therapies, such as HIFU and cryotherapy, are hampered by high complication rates and low chance of permanent success (Simmons et al 2007, Aus et al 2007). For men with short life expectancy and men who received primary radiotherapy, the advice is watchful waiting with hormonal therapy if needed.

Metastatic prostate cancer

Androgen deprivation therapy is a primary treatment of metastatic prostate cancer (Huggins and Hodges 1941). Patients with extraprostatic growth, with or without lymph-node metastases, or distant metastases, are given endocrine therapy.

Treatment of androgen-independent prostate cancer

The renewed progression of metastatic androgen-independent prostate cancer is the final stage of the disease and constitutes a substantial threat of morbidity and mortality. Recently, two large clinical trials showed that docetaxel, alone or in combination with estramustine, improved the survival of men with hormone-refractory prostate cancer in comparison with mitoxantrone and corticosteroids (Petrylak et al 2005, Tannock et al 2004). Such biologically active drugs as angiogenesis and signal transduction inhibitors, vaccines and other immunomodulators have a potential to be a new treatment modality (Sowery et al 2007). Prostate cancer expresses unique targets that enable the development of specific vaccines to recognize the cancer cells without affecting the benign tissue (Sowery et al 2007).

2.3. Prostate cancer research models

2.3.1. In vivo models

In 1969, the first human tumor growing in an immunodeficient ‘‘nude’’ (athymic) mouse was reported (Rygaard et al 1969). Since then, human tumor xenografts grown in nude mice (Giovanella et al 1972) or in mice with severe combined immunodeficiency (SCID) (Boxma et al 1983) have covered all of the major tumor types. In 1976, the Developmental Therapeutics Program at the National Cancer Institute (NCI) adopted 3 subcutaneously (s.c.) grown xenografts (colon, CX-1; breast, MX-1; and lung, LX-1) into their *in vivo* cancer drug screening program (Plowman et al 1997).

L. R. Kelland has provided a standard operational procedure (SOP) for conducting a xenograft experiment (Kelland 2004). The SOP points out the importance of appreciating and understanding each of the many variables existing in the use of xenografts such as origin of the xenograft model, site of implantation, growth characteristics, treatment modality and experimental endpoint.

Human tumor xenografts can be established by direct implantation of patient biopsies or via inoculation of human tumor cell lines. Xenografts derived directly from patient biopsies largely retain the morphological and molecular properties of the source tumors. In contrast, xenografts derived from cell lines show a more homogeneous, undifferentiated histology (and sometimes loss of the target receptors and proteins), probably due to the higher selection pressure *in vitro* during extensive culturing.

While most xenograft experiments use s.c. implantation, there are many reports of differences in biological behavior when tumors are grown s.c. relative to orthotopically (Eccles 2002). It is recognized that not all xenograft models are usable for compound screening because of their growth properties. Sometimes growth is too slow, too inconsistent/erratic/non-linear with time, or they possess cystic or necrotic areas, even at relatively small tumor volumes. The occurrence of cystic or diffuse necrotic areas can often comprise 20-80% of the tumor mass, depending upon the model and number of passages in mice (Corbett et al 2002).

2.3.2. Xenograft models for prostate cancer

During the 1980s and 1990s, numerous chemotherapy trials in hormone refractory prostate cancer consistently showed poor response rates, without any trend towards improved survival (Yagoda and Petrylak, 1993). To increase the speed of selection between the large amounts of new chemotherapic drugs in prostate cancer treatment, the use of human prostate cancer xenograft models as a pre-screening system was proposed (Schröder et al, 2000). Such a xenograft-based pre-screening enabled a relatively fast selection of the best performing compound and new combinations. These preclinical studies allow validation of biomarkers, such as PSA, for their use in subsequent clinical studies (van Weerden et al 2009). In xenograft models, circulating levels of PSA can be directly correlated to tumor burden, allowing validation of the relationship between PSA and tumor response during therapy (Limpens et al, 2006).

Prostate cancer research has long been hampered by the limited availability of representative model systems. The classical models are the androgen-independent PC3 and DU145 cell lines and the androgen-responsive LNCaP cell line (Van Bokhoven et al, 2003). PC3 and DU145 lack expression of androgen receptor and PSA (Ruizeveld de Winter et al, 1994). Although more clinically relevant, the androgen-responsive and PSA-secreting LNCaP cell line has its limitation in poor *in vivo* tumorigenicity and aberrant response to anti-androgens. This is due to a point mutation in the ligand-binding domain of the androgen receptor, rendering the cells sensitive not only to androgens, but also to other hormones such as progesterone and oestrogen, as well as to anti-androgens such as hydroxyflutamide (Veldscholte et al, 1992).

The amount of human-derived xenografts was low, before a significant number of human prostate cancer xenografts were established in the 1990s (Van Weerden et al, 1996). Thereafter, other groups, primarily in the United States, established several human-derived xenografts, such as the CWR, MDA Pca, LuCaP and LAPC series of xenografts (Table 2.3). All these xenografts are available to other researchers (Bosland et al 1996, Navone et al 1999).The development of permanent cell lines from prostate cancer xenografts has been complicated, with the PC346 xenograft for a long time being the only xenograft resulting from a cell line (PC346C) (Marques et al, 2006). In recent years, a small number of xenograft-derived cell lines have been established. These include PC346C, 22Rv1, CWR-R1, DuCaP, LAPC-4, MDA Pca1, MDA Pca2a, MDA Pca2b and VCaP, all being karyotyped and compared in an extensive study by van Bokhoven et al (van Bokhoven et al 2003). The present set of xenograft models and cell lines represent the various disease stages of human prostate cancer, suitable for preclinical testing.

Xenografts are well suited for molecular studies as they consist of pure human tumor tissue without contamination of human normal prostate tissue, which is always present in patient samples. Xenografts have been used in evaluation of abnormal genetic changes and gene profiles in human prostate cancer (van Weerden et al 2009). Genomic characterization shows that specific genomic abnormalities being detected in prostate cancer patients, such as mutations in the PTEN suppressor gene and genetic alterations in specific genes, also are prevalent in the xenografts (Vlietstra et al 1998, Maki et al 2007). Knowledge of the genomic profile of xenografts is crucial for selecting the most appropriate preclinical model, especially in the new era of targeted therapies requiring model systems with a specific molecular expression profile mimicking a specific disease stage or patient group (van Weerden et al 2009).

Table 2.3 Human prostate cancer xenografts (van Weerden et al 2009)

Name	Derived from	Androgen responsive	PSA	AR	Year
PC-82	Prostate	Yes	Yes	Yes	1977
PC-133	Bone	No	No	No	1981
PC-135	Prostate	No	No	No	1982
PC-EW	Prostate	Yes	Yes	Yes	1981
PC-295	LN	Yes	Yes	Yes	1991
PC-310	Prostate	Yes	Yes	Yes	1991
PC-324	TURP	No	No	No	1991
PC-329	Prostate	Yes	Yes	Yes	1991
PC-339	TURP	No	No	No	1991
PC-346	TURP	Yes	Yes	Yes	1991
PC-346I	PC-346	No	Yes	Mutant	1992
PC-346B	TURP	Yes	Yes	Yes	1991
PC-346BI	PC-346B	No	Yes	Yes	1992
PC-374	Skin	Yes	Yes	Yes	1992
TEN/12	Prostate	Yes	Yes	Yes	1985
LuCaP 23.1	Lymph node	Yes	Yes		1996
LuCaP 23.8	Lymph node	Yes	Yes		1996
LuCaP 23.12	Liver	Yes	Yes		1996
LuCaP 35	Lymph node	Yes	Yes	Yes	2003
LuCaP 35V	LuCaP 35	No			2003
LuCaP 49	Metastasis?	No	No	No	2002
LAPC-3	AI TURP	No	Yes/no	Yes	1999
LAPC-4	AI LN	Yes	Yes	Yes	1997
LAPC-9	AI Bone Met	Yes	Yes	Yes	2001
CWR22	AD Met	Yes	Yes	Mutant	1993
CWR21	AD Met	Yes	Yes	Yes	1993
CWR31	AD Met	Yes	Yes	Yes	1993
CWR91	AD Met	Yes	Yes	Yes	1993
MDA Pca-31	Liver	NA			1998
MDA Pca-40	Liver	NA			1998
MDA Pca-43	Adrenal	NA			1998
MDA Pca-44	Skin	NA			1998

AR = androgen receptor; LN = lymph node metastasis; MET = metastasis; NA = not applicable; PC = prostate cancer; PSA = prostate-specific antigen; TURP = transurethral resection of the prostate.

2.3.3. The orthotopic PC xenograft model

The majority of preclinical studies are performed using subcutaneously (s.c.) implanted tumor cells or xenografts. With the establishment of new human prostate cancer cell lines from xenografts, orthotopic injections of PC346C, LAPC4 and LuCaP cell lines into the mouse prostate have become an alternative to the traditional s.c. xenograft model. The orthotopic model is especially important in evaluation of targeted therapies where expression of the tissue-specific target is essential and influenced by the implantation environment (van Weerden et al 2009).

A drawback of orthotopic transplantation in the mouse prostate is the difficulty of monitoring tumor growth with time. In the case of PSA-producing cells, plasma PSA may be used as an indicator of tumor burden, although this approach would lack validation of circulating PSA levels to actual tumor load (Thalmann et al 1996). To allow longitudinal studies of treatment efficacy in individual mice, a three-dimensional ultrasound micro-imaging technique has been developed, allowing monitoring of prostate tumor growth (Kraaij et al 2002).

2.3.4. Tumor characteristics of PC xenografts

Initially, xenograft data was thought to have a poor prediction of human responses in clinical trials. As the three classical cell line models, PC3, DU145 and LNCaP, were strongly overrepresented, this may relate to the inappropriate choice of the model system (van Weerden et al 2009). With the present generation of xenograft models and the detailed knowledge of their genomic profiling, human xenografts are thought to be powerful tools in investigation of compound efficacy, specificity or identification of the mechanisms of action (van Weerden et al 2009). To perform relevant preclinical studies, the choice of the most appropriate model is essential and largely depends on the patient group the model is representing, and the expression of the target of interest.

2.3.5 Androgen responsiveness in prostate cancer xenografts

Hormonal treatment has been the main treatment in advanced prostate cancer since the first studies of Huggins and Hodges in the early 1940s. Since then, androgen responsiveness and androgen receptor (AR) characteristics, as well as PSA expression, have been the most important determinants for prostate cancer models (see Table 1.4, van Weerden et al 2009). Most tumors from prostate cancer patients that no longer respond to endocrine therapy have retained a functional AR, often with higher levels than in primary tumors (Ruizeveld de Winter et al 1994). It is suggested that the AR still is involved in growth regulation at this stage and that presently available anti-androgens not are capable of blocking this activity. The PC346 xenograft system and some of the CWR22, LuCAP and LAPC xenografts, show progressive, androgen-independent growth after androgen deprivation of tumor-bearing mice (Marques et al 2006). These resistant, androgen-independent sublines are valuable assets in the study of androgen-resistant molecular pathways (Hendriksen et al 2006). Marques and colleagues established a set of anti-androgen (flutamide) resistant PC346C cell lines that mimic the clinical situation of androgen-indipendent prostate cancer. This unique cell line can also be grown as xenografts, reflecting the various mechanisms of androgen-resistance also being observed in patients, including mutation, overexpression and downregulation of the AR (Marques et al, 2005).

2.3.6. CWR22 xenograft model

CWR22 is an androgen-dependent, human prostatic carcinoma xenograft established from a transurethral resection and grown subcutaneously in male athymic nude mice, each containing a s.c. implanted 12.5 mg testosterone pellet (Innovative research, Sarasota, FL) (Pretlow et al 1993). The CWR22 xenograft was taken from a stage D, Gleason score 9, prostatic carcinoma with osseous metastases and was the first serially growing primary prostatic carcinoma (Pretlow et al 1993). Among the standard prostate tumor lines, CWR22 has the least deviated sets of chromosomal aberrations from human prostatic carcinomas (Wainstein et al 1994).

Upon androgen withdrawal, CWR22 PSA messenger ribonucleic acid (mRNA) and protein decrease rapidly, cells undergo apoptosis and tumors regress in size (Wainstein et al 1994, Gregory et al 1995). After several months they recur in the absence of testicular androgens in a manner characteristic of human androgen-independent prostate cancers (Wainstein et al 1994, Gregory et al 1995). Thus, the CWR22 model allows the study of tumor behavior in both androgen-dependent and -independent states.

In mice bearing CWR22 xenografts, Wainstein et al (Wainstein et al 1994) observed that serum PSA concentrations correlated with tumor size (Figure 2.7), and that blood levels of PSA decreased after androgen withdrawal. Gregory et al (Gregory et al 1995) demonstrated a decrease in CWR22 PSA mRNA levels within 48 h after androgen withdrawal.

The slope of the graph in Figure 1.7 suggests that one can detect 1-2 mg of tumor with 50 μl of serum from the tail vein (Wainstein et al 1994). There was observed a significant metabolic decrease after irradiation in contrast to a lack of change in tumor volume and PSA for the same time frame in control mice (Dyke et al 2003).

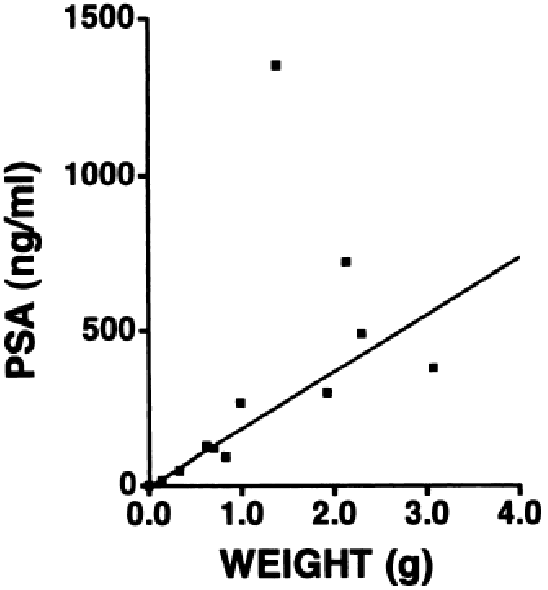

Figure 2.7. Correlation of PSA plasma concentration versus tumor volume. PSA plasma concentration was linearly related to tumor size up to 0,8 g, and continued to increase in larger tumors (Figure from Wainstein et al 1994)

2.4 Magnetic resonance imaging

2.4.1. Physics of magnetic resonance imaging

The phenomenon of Nuclear Magnetic Resonance (NMR) was independently discovered by two groups of physicists headed by F. Bloch and E. M. Parcell (Bloch et al 1946/69, Bloch et al 1946/70, Bloch 1946, Purcell et al 1946). The basic physical effect in NMR is the interaction between nuclei with a nonzero magnetic moment (^{1}H, ^{13}C, ^{17}O, ^{31}P) and an external magnetic field. Due to abundance of hydrogen in human body, proton resonance is used in clinical imaging, thus, the equations in this chapter is written for the case of the proton.

Under the influence of B_0 the sample becomes magnetized. In thermal equilibrium the nuclear magnetization in the sample can be expressed as

$$M = \chi B_0 \tag{2.2}$$

where χ is the nuclear susceptibility, the degree of magnetization of a material in response to an applied magnetic field.

Interaction between proton and external field can be described by the Hamiltonian

$$H = -\mu B_0 \tag{2.3}$$

where **μ** is the magnetic moment of a nucleus. The moment μ can be expressed as

$$\mu = \gamma \frac{h}{2\pi} I \tag{2.4}$$

where $\frac{h}{2\pi} I$ is the angular moment of the nucleus and γ is a constant called the gyromagnetic ratio, $\gamma_H = 42.6$ MHz/T.

The magnetic moment μ will precess around the axis of B_0 at a frequency given by the Larmor equation

$$\omega = \gamma B_0 \tag{2.5}$$

where ω is the angular precessional frequency.

Excitation

The NMR signal from a macroscopic sample is proportional to the equilibrium magnetization in the sample

$$M = n \langle \mu \rangle \tag{2.6}$$

where n is the number of nuclei and <μ> is the average magnetic moment of nuclei. Because the energy of magnetic interaction is minimum when μ is parallel to $B_{0,}$ the probability that a nuclear magnetic moment is parallel to B_0 is greater than being antiparallel to B_0. In thermal equilibrium more magnetic moments in a sample are aligned with the external field. Because the energy of interaction does not depend on the component of μ in the plane perpendicular to B_0 (transverse plane), the average transverse component of μ is zero. The equilibrium magnetization satisfies the following conditions: $M_Z = M_0 > 0$, $M_X = 0$, $M_Y = 0$ where the z-axis is in the direction of B_0. The signal which is detected in MR imaging is the varying magnetic flux in the xy-plane. The net magnetic moment in the z-direction has to be rotated or 'flipped' into the xy-plane to achieve a detectable signal. This flipping is called excitation.

The excitation of the protons is achieved by applying another magnetic field, B_1, in the xy-plane. B_1 is a linear polarized oscillating magnetic field with an oscillation frequency equal to the Larmor frequency ω and can be described as

$$B_{1,x} = B_1 \cos \omega t, B_{1,y} = 0, B_{1,z} = 0 \tag{2.7}$$

The B_1 field is applied a time τ and is called the radiofrequency (RF) pulse or the excitation pulse. During the time τ the magnetic field is flipped an angle $\Theta = \gamma \tau B_1$.

If the RF pulse flips magnetization M_Z into xy-plane it is called a 90°-pulse, and if magnetization M_Z rotates 180° then the RF pulse is called a 180°-pulse. In practice flip angles can have all values from 0 to 180°.

Rotating Frame of Reference

The stationary frame of reference, x, y, z, is called the laboratory system. A new frame x', y', z' is defined, which rotates around the z-axis with the Larmor frequency and is called the rotating frame of reference. In the rotating laboratory system, the magnetization vector will be static, provided the RF pulse is applied along the x axis.

Relaxation

After excitation, the magnetic dipole moment will try to re-establish equilibrium. This is called relaxation. In the Bloch model it is the thermal perturbations which cause relaxation of the longitudinal magnetization M_Z back to its equilibrium state, while interactions between nuclei in the sample cause decay of the transverse magnetization M_{xy} (Bloch 1946). This relaxation can be detected with external coils. The phenomenon is called free induction decay, FID.

T_1 relaxation

The relaxation of M_Z is described by

$$\frac{dM_Z}{dt} = \frac{(M_0 - M_Z)}{T_1} \tag{2.8}$$

where T_1 is a constant known as the spin-lattice relaxation time (Bloch 1946). A solution of this equation can be written as

$$M_z = M_0 + \left[M_z(0) - M_0\right]\exp(-t/T_1)\,, \tag{2.9}$$

where $M_z(0)$ is the initial value of M_z.

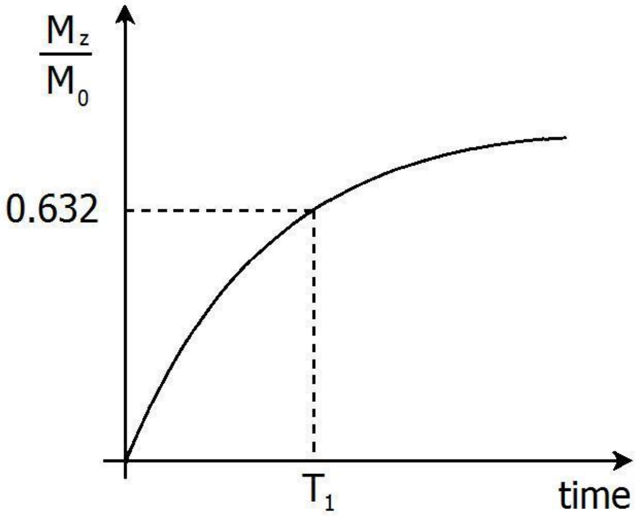

Figure 2.8 Relaxation of longitudinal magnetization M_Z to its equilibrium state and T_1 constant.

T_1 relaxation occurs when protons excited to a higher state of energy, spin-up, returns to the lower state, spin-down. The transition between the energy states is stimulated by fluctuating magnetic field in the medium. They originate from molecular movements and can stimulate transitions between the energy states if the fluctuation has frequency components equal to the Larmor frequency.

The T_1 constant is tissue-specific. A short T_1 indicates that the tissue containing the protons suitable for the energy exchange. Fat has short T_1, water has long T_1, and solid tissue has intermediate T_1 relaxation times.

T_2 relaxation

Different nuclear moments precess at slightly different Larmor frequencies as a result of magnetic interactions between neighbouring nuclei. The presence of microscopic magnetic fields created by the nuclei themselves or by electrons causes dephasing of nuclear spins in a sample. This results in an exponential decay of M_{xy} that occurs with a characteristic time constant T_2 known as the spin-spin relaxation time. The dynamics of M_{xy} in the laboratory coordinate system is described by:

$$\frac{dM_X}{dt} = -\frac{M_X}{T_2} + \gamma M_Y B_0, \frac{dM_Y}{dt} = -\frac{M_Y}{T_2} - \gamma M_X B_0 \qquad (2.10)$$

A solution of this equation can be written as

$$M_{xy}(t) = M_{xy}(0)\exp(t/T_2) \qquad (2.11)$$

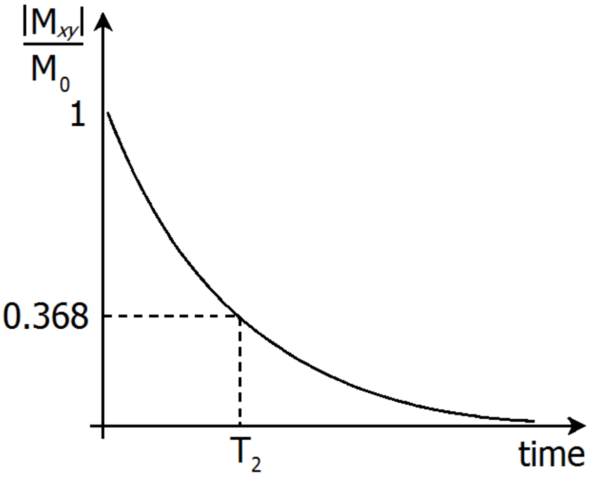

Figure 2.9 Relaxation of transverse magnetization and T_2 constant

In practice a more rapid decay of transverse magnetisation, known as the T_2*-decay, is observed. It happens due to local magnetic field heterogeneity because of the nonuniformity of the applied field, spatially varying magnetic susceptibility in the media and destructive interference of the signal produced by different nuclei in the volume. The T_2*-decay can be determined by:

$$\frac{1}{T_2*} = \frac{1}{T_2} + \gamma \frac{\Delta B_0}{2} \tag{2.12}$$

where ΔB_0 is the inhomogeneities in the magnetic field.

Water has long T_2 relaxation time and is bright at T_2-weighted images, while fat has short T_2 relaxation time and appears dark on T_2-weighted images.

Spin echo

Fast dephasing of nuclear spins due to magnetic field heterogeneity causes a significant loss of signal. The phenomenon of magnetic dipole moments refocusing in x'y' plane by a 180°pulse after a 90°excitation RF pulse was discovered by E. Hahn (Hahn 1950) and is known as *spin echo*.

The series of RF pulses shown on Figure 2.10 is called spin echo sequence.

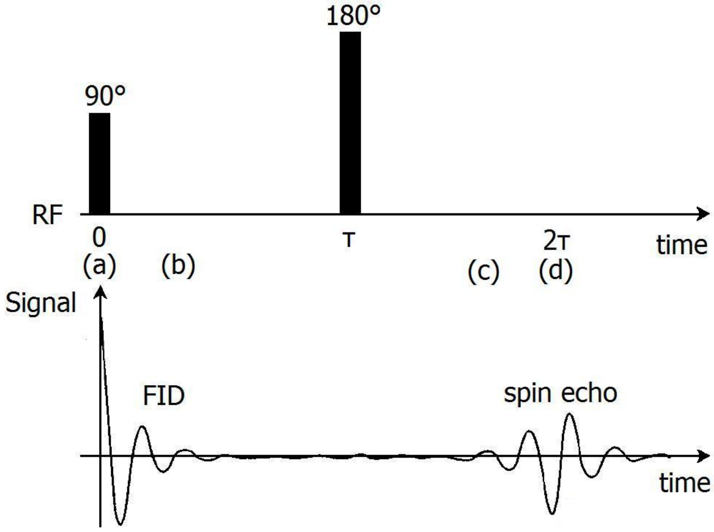

Figure 2.10 FID and spin echo signal produced by a spin echo sequence.

The sequence starts with an excitation 90° pulse that flips a net magnetic dipole moment into x'y' plane (Figure 2.11a). Due to different Larmor frequencies of dipole moments after a period of time they will be out of phase (Figure 2.11b). After time τ a 180°pulse is applied. This causes refocusing of dipole moments (Figure 2.11c). At the time 2τ, the echo time (TE), the dipole moments will be in phase again and a new signal can be registrated (Figure 2.11d).

If the 180°pulses are repeated a series of echoes can be detected. The amplitude of the signal is declining with the T_2 relaxation constant.

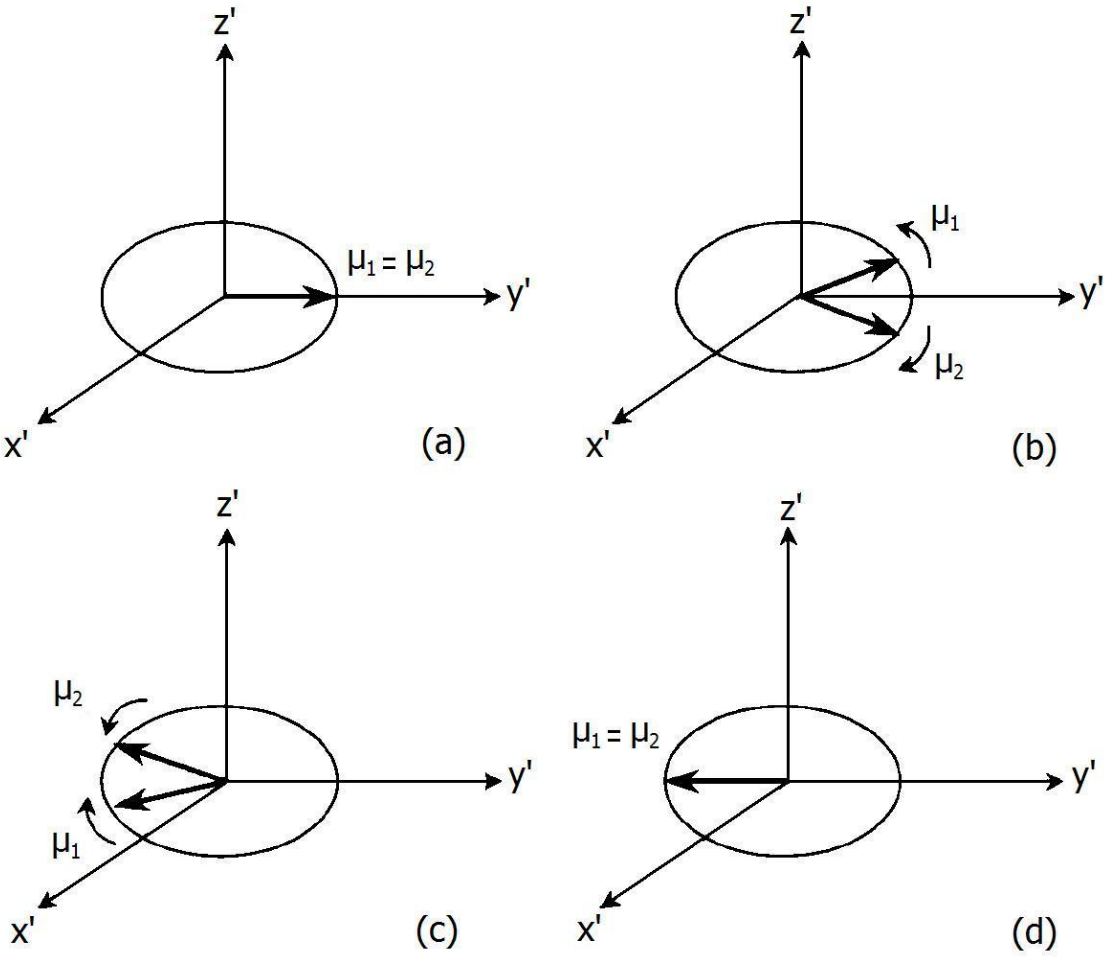

Figure 2.11. Refocusing of dipole moments in the rotating coordinate system.

Image reconstruction.

The detected signal is a sum of contributions from all the excited magnetic dipole moments in the sample volume. To achieve an image with spatial resolution, signals from smaller volumes need to be separated. It can be achieved by introducing magnetic field gradients which causes the Larmor frequency to be a function of position. Gradients in the x, y and z directions are required to obtain spatial information:

- The slice select gradient, Gz

- The frequency-encoding gradient, Gx

- The phase-encoding gradient, Gy

The Slice Select Gradient

In addition to the external magnetic field, B_0, a linear magnetic gradient in the z-direction,G_z, is applied

$$B = B_0 + G_Z z - \frac{\omega}{\gamma} \tag{2.13}$$

Since the Larmor frequency is proportional to the strength of the magnetic field, the Larmor frequency will have a z-dependence given by

$$\omega = -\gamma(B_0 + zG_Z) \tag{2.14}$$

The magnetic dipole moments outside the slice will not be excited as their Larmor frequencies differs from the frequency of the B_1.

Frequency and Phase Encoding

Phase and frequency distribution within the selected slice can be modified by applying gradients in the x- and y-directions.

After applying the gradient in the y-direction, G_y the magnetic dipoles will rotate with a frequency determined by their y position. The phase angle α=ωt is defined by

$$\alpha(r,t) = -\gamma \int_0^{\tau} G_y(t) r dt = kr \tag{2.15}$$

where r=*i*x+*j*y defines the position of the dipole, k represents coordinates in spatial frequency space (k-space) and has the unit radians per meter. The k-space is the Fourier transform of the MR image and represents the spatial frequency distribution. The central part of k-space contains low spatial frequency information (contrast), whereas the outer parts of k-space contain high spatial frequency information (detail, edges).

After a time t_y, G_y is turned off, resulting in the magnetic dipoles to precess with the same frequency. Due to varying precession speed while G_y is on, the magnetic dipole moments will have different phase dependent on the y position. This technique is called phase encoding, and the phase of the individual y positions is given by

$$\alpha_y = \omega_y t_y = \gamma G_y t_y y = k_y y \tag{2.16}$$

The gradient G_x turns on while the G_y gradient is active and during detection of the signal. This is called the read-out gradient. The magnetic dipole moments will during detection of the signal precess with a frequency dependent on the x position. To be able to image the entire slice, this sequence is repeated with a new G_y in every repetition, resulting in a set of FIDs with different G_y. To make an image with $N_x \times N_y$ points, N_x points are needed in every FID and the sequence must be repeated N_y times. In terms of k-space, a single line along k_x is sampled following each RF pulse. In MRI the pulse sequence using this sampling principle is called *gradient echo* (GRE) sequence. This sequence is faster than spin echo sequence due to absence of refocusing pulse and therefore shorter repetition and echo times.

The magnetization M(*r*,*t*) gives rise to the detected signal. The total transverse magnetization is given by

$$M(x,y) = M(r,t) = M(r,o)\exp(-j\gamma\int_0^t G(t)rdt) = M(x,y)\exp(-j(k_x x + k_y y)) \quad (2.17)$$

The total signal is a sum of contributions from all sample volumes. By applying an inverse Fourier transformation, signal for a given slice signal can be defined as

$$S(k_x,k_y) = C\iint_{slice} M(x,y)\exp(j(k_x x + k_y y))dxdy \qquad (2.18)$$

where C is a constant.

Imaging Coils

A coil is an electrical device composed of a single or multiple loops of wire. The coil can either generate a magnetic field, a gradient coil, or detect an oscillating magnetic field as an electrical current induced in the wire, a RF coil (Hashemi and Bradley 1997).

Gradient coils include the imaging gradient coils and the shim coil. The imaging gradient coil causes a perturbation in the magnetic field homogeneity which results in spatial encoding. Shim coils are used to produce a magnetic field which cancels spatial variations in the external magnetic field, B_0. Transmit and/or receive RF coils include the single phase or quadrature coils, the surface or volume coils, called solenoid, and the phased array coils. The quadrature coils have two receivers which are 90° to one another in order to distinguish between the real- and imaginary components of the received signal. The solenoid coils can be wrapped around the patient to increase the SNR. Phased array coils contain multiple small surface coils. These coils allow faster scanning with finer details and increased signal to noise ratio (SNR).

Coil for Imaging of Small Animals

For small animal imaging in clinical whole-body MRI scanners, high spatial resolution images of thin tissue sections, high SNR and high B_1 field homogeneity are needed. While gradient strength in modern scanners is sufficient, the sensitivity of conventional coils does not satisfy the demands. To be able to image small animals, an open gap transmit-receive MR coil for imaging small animals in a clinical whole-body 1.5 T MR scanner can be used (Seierstad e al 2007). The coil is shown in Figure 2.12.

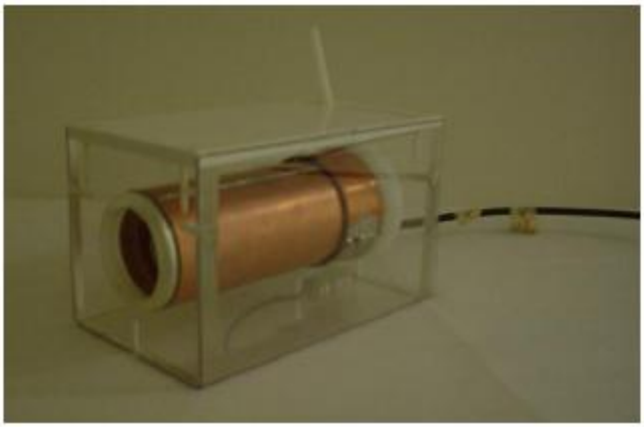

Figure 2.12. The transmit-receive MR coil for imaging of small animals in a clinical 1.5 T MR scanner.

The coil is tuned to a frequency close to the expected Larmor frequency of the protons at 1.5 T (63.89 MHz). The tuning creates a higher output signal for a given input signal and minimizes losses due to external sources with other frequencies. The coil provides examinations with nearly homogeneous sensitivity in the entire body at a spatial resolution of 1-2 mm. For all MR experiments with the coil, a 30 dB attenuator has to be connected to the transmit line of the MR scanner in order to reduce the excitation signal. There is no need for hardware modifications of the MR scanner.

Contrast in MR Imaging

MRI is an important diagnostic tool because it provides exquisite contrast between various soft tissues, enabling identification of pathologic processes. Variations in relaxation times, T_1 and T_2, and the amount of protons per unit volume (known as proton density, $N(H)$) are the predominant sources of contrast in ^{1}H MRI. The use of T_1 and T_2 in identification of pathology is based on differences in relaxation times between malignant and benign tissues (Damadian 1971).

T_1 *Contrast*

When tissues with different T_1 relaxation times experience excitation pulses, tissues with short T_1 will restore their longitudinal magnetization more rapidly and have a greater transversal magnetization than tissues with long T_1. As a result, imaged tissues with short T_1 are brighter than tissues with long T_1. These images are known as T_1-weighted images. Improved T_1 contrast is obtained by using short repetition times (TR) such that differences in T_1 relaxation times between the tissues are large, while keeping the echo time (TE) short to avoid influence of differences in T_2 relaxation among the tissues.

T_2 Contrast

In T_2 weighted images tissues with long T_2 appears bright, whereas tissues with short T_2 appears dark. These images are obtained by using long TR to avoid the differences in T_1 relaxation times, and a long TE to maximize the differences in T_2 relaxation times between the tissues.

Proton Density Images

Proton density is the number of protons per unit volume. Proton density-weighted images are produced using a long TR to avoid differences in T_1 relaxation times and a short TE to avoid differences in T_2 relaxation times.

Contrast Agents

Contrast agents can enhance MR image contrast by altering the $T_{1,}$ T_2 and T_2^* relaxation times and are used in diagnostic MRI to achieve better assessment of physiological and anatomical conditions or to improve detection of malignancy. These substances are administered internally, and must therefore possess low toxicity and easily be excreted from the body.

Paramagnetic ions with a number of unpaired electrons such as Gd^{3+} and Mn^{2+} are used as contrast agents because of their high relaxivities. To reduce the toxicity of these ions for *in vivo* applications, they are chelated to special molecules. Gadolinium pentetate (Gd-DTPA), the currently most used MRI contrast agent, is a chelate composed of gadolinium ions and diethylenetriaminepentaacetic acid (DTPA). Chelation of gadolinium ions decreases the effective amount of water molecules that interact with the paramagnetic ions, thus the relaxivities of Gd-DTPA are less than the corresponding relaxivities of the free gadolinium ion. Gd-DTPA is typically administered at a dose of 0.1 - 0.2 mmol/kg.

Rapid MR Imaging

Rapid MRI techniques were developed to reduce motion artifacts and scan times in diagnostic MRI. Reduction in scan time is achieved by using gradient-echo imaging with short TRs, echo-planar imaging (EPI) and fast spin-echo imaging (FSE).

Rapid Gradient-Echo Imaging

There are two different techniques for rapid gradient-echo imaging. The first one is *Spoiled Gradient-Echo Imaging* that employ RF and gradient spoiling to destroy the transverse magnetization after each signal acquisition while maintaining the steady-state longitudinal magnetization. The second approach is *Refocused Gradient-Echo Imaging* with gradient refocusing used to maintain both transverse and longitudinal components of the magnetization in equilibrium. This means that a single refocused magnetization vector is present in the transverse plane at each RF-excitation and no ‘splitting’ of the transverse magnetization occurs. The effects of field inhomogeneities are refocused (no T_2* effect) and "true" T_2 decay is observed.

Accelerated k-space trajectories

In spin echo and GRE sequences a single line in k-space is read out per one RF pulse (one TR interval). Scan time is therefore long, especially when strong T_2 weighting required. The acquisition time can be reduced by acquiring multiple k-lines per TR-interval. Two main techniques that use this approach are EPI and FSE.

FSE is a spin echo pulse sequence including a series of rapid 180° rephasing pulses and multiple echoes, changing the phase encoding gradient for each echo. Compared with conventional spin echo sequence where a single k_y-line is read out per TR, multiple k_y-lines are read in FSE. If all k_y-lines are read out after a single 90° pulse followed by N_y 180° pulses then the sequence is called *Single Shot FSE* (SSFSE). The number of echoes acquired in each TR interval is called echo train length (ETL). For example, if an ETL=10 then this will result in 10 fold reduction of scan time relative to scan time used to cover the same volume with single spin echo.

In the EPI sequence, multiple k-lines are acquired following a single excitation pulse and a complete EPI can be acquired in approximately 100 ms. But in addition to speed, EPI is very sensitive for field inhomogeneities which results in many artefacts.

2.4.2. Dynamic contrast enhanced magnetic resonance imaging

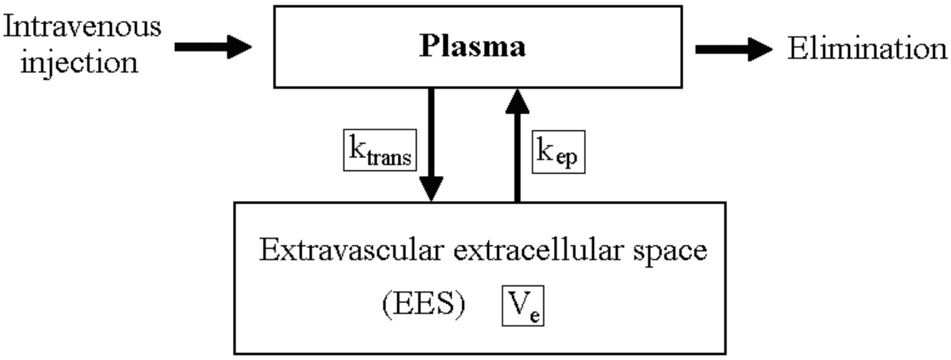

Figure 2.13 Two compartment pharmacokinetic model. After an intravenous bolus injection of low molecular weight contrast agent, it mixes with plasma and can penetrate through damaged capillary membrane (e.g. in tumors). The transfer is described by a constant of the transport of contrast agent from plasma into the EES,K^{trans}, and a transport constant of backflux from EES to plasma,K_{ep}. V_e is a fraction of EES in total tissue volume

Dynamic contrast enhanced (DCE) MRI is a method of tracing dynamic effects in MR contrast after a bolus injection. When a paramagnetic, low-molecular weight contrast agent is injected intravenously, it enters the blood vessels and subsequently passes into the extravascular extracellular space (EES) (Figure 2.13). A high first pass extraction occurs in most normal tissues, while in tumors, typically 12-45% of the contrast media leaks into the EES during the first pass (Daldrup et al 1998). Then the contrast agent freely diffuses within the interstitial space until whole body distribution and renal excretion lowers the vascular concentration below that in the interstitial space and the contrast medium passes back into the vascular space. Three major factors determine the behavior of low molecular weight contrast agents during the first few minutes after injection: 1) blood perfusion (contrast agent delivery), 2) transport of contrast agent across vessel walls and 3) diffusion of contrast medium in the interstitial space. If the delivery of the contrast medium to a tissue is insufficient to maintain a high vascular concentration compared to that in the EES (flow-limited situations or the vascular permeability is greater than inflow), then blood perfusion will be the dominant factor determining contrast agent kinetics, which is the situation in tumors. As low molecular weight contrast agents do not cross cell membranes, its volume of distribution is the volume of the EES, V_e.

The most commonly used mathematical model for describing contrast agent distribution is the two-compartment model, also called the Tofts model (Figure 2.13).

The dynamics of contrast agent concentration in tissue can be described by the following equation:

$$\frac{dC_t(t)}{dt} = K^{trans} C_p(t) - k_{ep} C_t(t) \tag{2.19}$$

where K^{trans} is a constant describing the transport of contrast agent from plasma into the EES, k_{ep} is a transport constant describing backflux from EES to plasma, C_p and C_t are contrast agent concentration in plasma and EES, respectively. K^{trans} is a measure of the permeability surface area product of the capillary walls in tissue. The constant k_{ep} is related to K^{trans} and V_e as

$$k_{ep} = \frac{K^{trans}}{V_e} \tag{2.20}$$

The contrast agent concentration in plasma $C_p(t)$ is determined by the arterial input function (AIF). For Gd-DTPA, the AIF can be approximated as:

$$C_p(t) = A\exp(-Bt) + C\exp(-Dt) \tag{2.21}$$

where A [mM], B [s^{-1}], C [mM] and D [s^{-1}] are constants determined by experiments. The first term of the equation describes the fast diffusion from blood vessels into EES, the second one describes slow elimination of Gd-DTPA by kidneys (Tofts 1997).

Using the equations for plasma concentration and the dynamics of contrast agent concentration, the equation of contrast agent concentration in tumor tissue will be as following:

$$C_t(t) = Dk_{trans}\left[(\frac{A(\exp(-Bt) - \exp(-k_{ep}t))}{k_{ep} - B}) + (\frac{C(\exp(-k_{ep}t) - \exp(-Dt))}{D - k_{ep}}) \right] \quad (2.22)$$

where D is the dose of Gd-DTPA injected.

The ability of the contrast agent to enhance the proton relaxation rate is defined in terms of relaxitivity:

$$R_{1,2} = \frac{1}{T_{1,2}} = R^0{}_{1,2} + r_{1,2}C_{Gd} \quad (2.23)$$

where $R^0{}_{1,2}$ are relaxation rates without presence of contrast agent, C_{Gd} is concentration of contrast agent, $r_{1,2}$ are relaxivities of contrast agent and have units of $mM^{-1}s^{-1}$. (Bjørnerud 2006).

The contrast agent concentration can be estimated using a method introduced by Hittmair et al. (Hittmair et al 1994). It is based on a T_1-weighted RF-spoiled GRE sequence with TE less than T_2*. Signal intensity in acquired images can be approximated as following

$$S \approx S_{\max}(1 - \exp(-K\frac{TR}{T_1})) \quad (2.24)$$

where K is a correction factor dependent on the flip angle. S_{max} is the maximum signal intensity and can be estimated from proton density images as following

$$S_{\max} = N(H)\sin\alpha = S_{\alpha=10^\circ}\frac{\sin\alpha}{\sin 10^\circ} \quad (2.25)$$

where N(H) is the proton density and $S_{\alpha=10^\circ}$ is the signal intensity in proton density images with a flip angle of 10°, α is the flip angle used in T_1 weighted images.

Relaxivity changes can be calculated using images taken before (precontrast) and after (postcontrast) administration of contrast agent using the following equation

$$\Delta R_1 = r_1 \approx \frac{1}{K \cdot TR}\ln(\frac{S_{\max} - S_{pre}}{S_{\max} - S_{post}}) = C \cdot C_{Gd} \quad (2.26)$$

where C_{Gd} is the measured concentration of Gd-DTPA in tissue, C is a constant, S_{pre} and S_{post} are signal intensities for pre- and postcontrast images, respectively.

C can be calculated if we introduce two phantoms, one (*fant0*) without contrast agent, another (*fant1*) with known Gd-DTPA concentration C_1 in the same image. Constant C can be determined as following

$$C = \frac{1}{C_1 K \cdot TR} \ln\left(\frac{S_{\max, fant0} - S_{fant0}}{S_{\max, fant1} - S_{fant1}}\right) \tag{2.27}$$

Measured concentration of contrast agent in tissue C_{Gd} can then be calculated using equation (2.26). The $C_{Gd}(t)$ curve is approximated using the Tofts model curve $C_t(t)$ (2.22). K^{trans}, V_e and k_{ep} can then be found.

2.4.3. Diffusion-weighted magnetic resonance imaging

Biological diffusion

(Based on Alexander et al 2007 if else is not stated)

Diffusion is a random transport phenomenon, describing the transfer of material (e.g., water molecules) from one spatial location to other locations over time. The Einstein diffusion equation (Einstein 1956) states that the diffusion coefficient, D (in mm^2/s), is proportional to the mean squared-displacement, $\langle \Delta \mathbf{r}^2 \rangle$, divided by the number of dimensions, n, and the diffusion time, Δt:

$$D = \frac{\langle \Delta r^2 \rangle}{2n\Delta t} \tag{2.28}$$

The diffusion coefficient of pure water at 20°C is roughly 2.0×10^{-3} mm^2/s and increases at higher temperatures. In the absence of boundaries, the molecular water displacement is described by a Gaussian probability density

$$P(\Delta r, \Delta t) = \frac{1}{\sqrt{(2\pi D \Delta t)^3} \exp\left(-\frac{\Delta r^2}{4D\Delta t}\right)} \tag{2.29}$$

The diffusion of water in biological tissues occurs inside, outside, around, and through cellular structures. Water diffusion is primarily caused by random thermal fluctuations, and is modulated by the interactions with cellular membranes and organelles. Cellular membranes hinder the diffusion of water, causing water to take more tortuous paths, thereby decreasing the mean squared displacement. The diffusion tortuosity and corresponding apparent diffusivity may be increased by either cellular swelling or increased cellular density. Thus, necrosis, which results in a breakdown of cellular membranes, decreases tortuosity and increases the apparent diffusivity. In fibrous tissues like white matter in brain, water diffusion is unimpeded in the direction parallel to the fiber orientation. This makes the diffusion in fibrous tissues anisotropic.

The diffusion tensor describes anisotropic diffusion behavior (Basser et al 1994, Basser et al 1994/2.) The model of Basser describes anisotropic diffusion by a multivariate normal distribution

$$P(\Delta i, \Delta t) = \frac{1}{\sqrt{(4\pi\Delta t)^3 |D|}} \exp(\frac{-\Delta i^T D^{-1} \Delta i}{4\Delta t}) \qquad (2.30)$$

where the diffusion tensor is a 3×3 covariance matrix:

$$D = \begin{bmatrix} D_{XX} & D_{XY} & D_{XZ} \\ D_{YX} & D_{YY} & D_{YZ} \\ D_{ZX} & D_{ZY} & D_{ZZ} \end{bmatrix} \qquad (2.31)$$

describing the covariance of diffusion displacements in three dimensions normalized by the diffusion time.

The diagonal elements, $D_{ii} > 0$, are the diffusion variances along the x, y and z axes, and the off-diagonal elements are the covariance terms being symmetric about the diagonal, $D_{ij} = D_{ji}$. Diagonalization of the diffusion tensor yields the eigenvalues l_1, l_2 and l_3 and corresponding eigenvectors $\hat{\boldsymbol{e}}_1$, $\hat{\boldsymbol{e}}_2$ and $\hat{\boldsymbol{e}}_3$, describing the directions and apparent diffusivities along the axes of principle diffusion. Diffusion is considered isotropic when the eigenvalues are nearly equal (e.g., $l_1 \sim l_2 \sim l_3$) and anisotropic when the eigenvalues are significantly different in magnitude (e.g., $l_1 > l_2 > l_3$). The eigenvalue magnitudes are affected by changes in local tissue microstructure, both diseased and normal physiological changes. Diffusion coefficient in case of isotropic diffusion is determined as $D = (l_1+l_2+l_3)/3$.

MRI and diffusion

Changes in T_1 and T_2 relaxation are often insufficient to detect or characterize lesions (Charles-Edwards and deSouza 2006), thus MR sequences have been sensitized to measure the “apparent diffusivity”. The diffusional motion measured by MRI relates to the mean path length, L, travelled by protons within a specific observation time period, the diffusion time, as a result of the thermally driven, random motion (Fig. 2.14 Charles-Edwards and deSouza 2006).

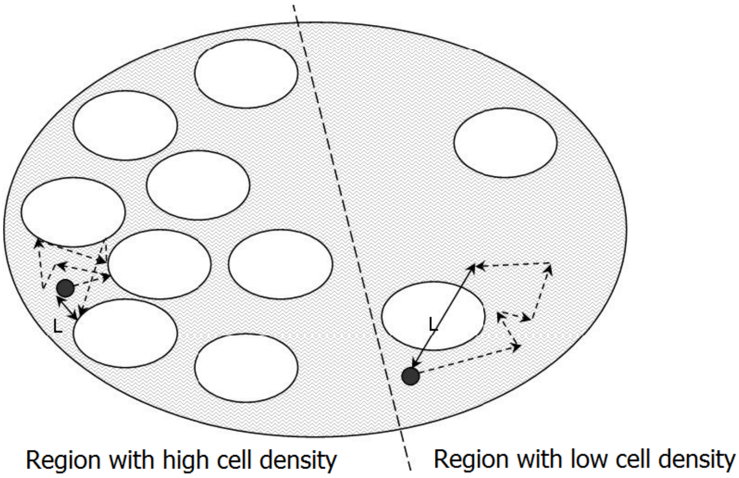

Figure (2.14). The mean path length *L* for regions with different cell density. Due to high density of the cells the mean path length is L is shorter than in low cell density areas (e.g. necrosis cores) (Charles-Edwards and deSouza 2006)

Diffusion-Weighted Image Acquisition

Diffusion sensitivity of MR sequences is achieved using a bipolar gradient pair. This sequence was originally called the Stejskal-Tanner sequence.

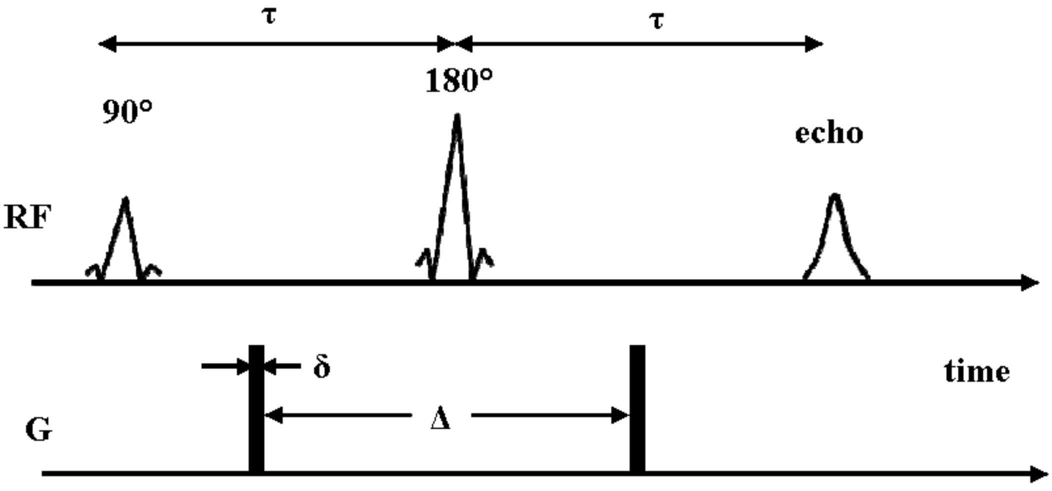

Figure (2.15) The Stejskal-Tanner diffusion weighted sequence (Bjørnerud 2006).

The gradient pulses attenuate the signal coming from spins that are diffusing in the presence of the gradient pulses. The first gradient pulse dephases the magnetization and the second rephases the magnetization. For stationary, non-diffusing, protons, the phases induced by both gradient pulses will cancel producing no signal attenuation from diffusion. The net phase effect for moving protons due to gradient pair is described as following

$$\Phi = \gamma\delta G(r - r') = \gamma\delta GR \qquad (2.32)$$

where γ is the gyromagnetic ratio, G is the magnitude of the diffusion-encoding gradients, δ is the duration of each diffusion encoding gradient, and Δ is the time interval between the leading edges of the diffusion-encoding gradients

The signal intensity for the resulting image can be written as following

$$S(b) = S(0)\exp(-(\gamma\delta G)^2(\Delta - \frac{\delta}{3})D) = S(0)\exp(-bD) \qquad (2.33)$$

where b is a parameter determining the amount of diffusion weighting in the sequence and has the units of s/m^2:

$$b = (\gamma\delta G)^2(\Delta - \frac{\delta}{3}) \qquad (2.34)$$

In our experiment, diffusion tensor imaging was achieved using a SSFSE-based diffusion MR acquisition. It provides images without the significant degree of spatial distortions that single shot EPI sequences suffers from. For diffusion tensor imaging, encoding a minimum of six non-collinear diffusion encoding directions are required to measure the full diffusion tensor. A wide variety of diffusion tensor encoding strategies with six or more encoding directions has been proposed (Charles Edwards and de Souza 2006).

Image analysis

A DW-MRI sequences’ sensitivity to diffusion can be adjusted by altering the combination of gradient pulse amplitude, the time for which the gradients are applied and the time that elapses between their application. The higher the *b*-value, the more sensitive an image is to the effects of diffusion. In biological objects diffusion is usually anisotropic or a mixture of diffusion in different compartments each having different diffusion coefficients, D. Therefore, the “apparent diffusion coefficient” (ADC) was introduced to measure a diffusion coefficient obtained in *in vivo* studies. ADC describes the displacement of protons during the application of the diffusion gradients (Mori and Barker 1999):

$$ADC = \frac{1}{b}\ln(\frac{S_0}{S_b}) \qquad (2.35)$$

where S_0 is the signal intensity without diffusion weighting, and S_b is the signal intensity with diffusion gradient. An ADC map created by combining two images with different *b*-values, the lower which is not large enough to remove the effects of perfusion (*b* values less than 300 s/m^2), contains information about perfusion as well as diffusion components. To differentiate between perfusion and diffusion multiple *b*-values are needed.

Most clinical machines create ADC maps by averaging three diffusion-weighted images which have encoded diffusion in the slice, frequency (read) and phase-encode directions, respectively. Such techniques are termed ‘isotropic’ and the associated averaged ADC maps sometimes termed ‘trace’ or ‘isotropic’.

Pathological correlates

The majority of diffusion MRI performed clinically to date has focused on the extracellular water diffusion. In highly cellular tissues, such as tumors, extracellular water diffusion is restricted, leading to a short diffusional path and a reduced ADC. Cystic or necrotic portions of tumors have few structural barriers present and have a high ADC. ADC maps, derived from diffusion-weighted imaging, can therefore provide a non-invasive measure of cellularity (Herneth et al 2003), being a promising tool in diagnosis, treatment planning and monitoring.

Chapter 3

Materials and Methods

3.1. Description of the experiment

The experiment consisted of 32 male mice with subcutaneously implanted CWR22 xenografts randomized into 4 groups of 8 mice:

1. CWR22 control
2. CWR22 irradiated
3. CWR22CA control
4. CWR22CA irradiated

Mice in group 1 and 2 were included in the experiment when the tumors' shortest diameter reached 8 mm. Mice in group 3 and 4 were castrated when the shortest tumor diameter was 13 mm. Due to castration the tumors regressed and at a shortest tumor diameter of 8 mm these animals were included in the experiment. The day of inclusion is called day 0.

MRI was performed at day 0, day 1 (24 h) and day 9. The tumors in the irradiation groups were irradiated with a single fraction of 15 Gy after the baseline MRI at day 0. When the tumors' longest diameter reached 16mm in two of the mice in one group or 30 days after inclusion into experiment (depending of what condition was satisfied first), the mice were sacrificed, and blood and tumor tissue were collected. An additional 8 mice with identical weight as the other mice were used to obtain vascular input functions (VIFs) by imaging the left ventricle. A schematic illustration of the experiment is shown in Figure 3.1. The individual parts of the diagram will be explained in detail in this chapter.

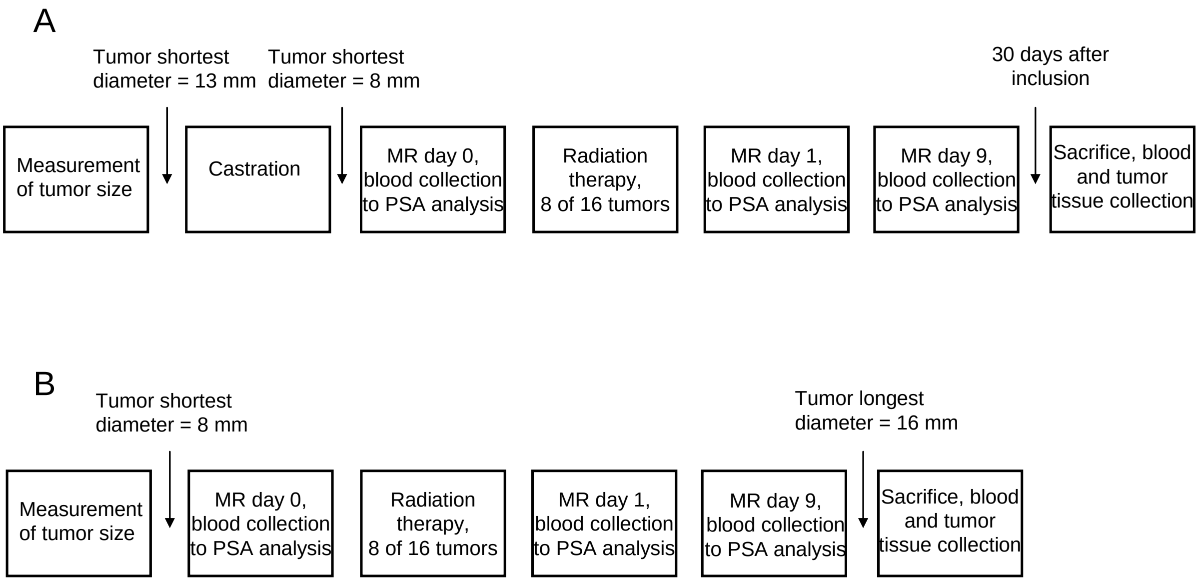

Figure 3.1. Schematic view of the experiments. The bottom row (B) shows the experimental procedure in group 1 and group 2 (CWR22), and the upper row (A) shows the experimental procedure in group 3 and group 4 (CWR22CA). Tumor sizes were measured two times a week from implantation until the mice were sacrificed.

3.2. Substances used in experiment

3.2.1. Anesthesia

An ampoule containing powder of 125 mg tiletamine and 125 mg zolazepam (Zoletil vet., Virbac, Carros, France) was mixed with 10 ml of 20 mg/kg xylazine solution (Narcoxyl vet, Roche, Basel, Switzerland) and 0.5 ml 10 mg/ml butorphanol solution (Torbugesic, Fort Dodge Laboratories, Fort Dodge, IA). The resulting stock solution was further diluted 1:5 with sterile water to prepare a mice Zoletil solution. Both stock and mice Zoletil solutions were stored at 4 °C, with new stock solution prepared every month. To obtain a full anesthesia, mice were s.c. injected with 75 µl per 10 g of weight, giving a total dose of 18 mg/kg zolazepam, 18 mg/kg tiletamin, 0.7 mg/kg butorphanol and 29 mg/kg xylazin. Full anesthesia lasted for approximately 2 hours.

Eye ointment containing 20% liquid paraffin and 80% vaseline (Simplex, Ophtha, Gentofte, Denmark) was used during every anesthesia to prevent the eyes from dryness.

3.2.2. Analgesia

An ampoule containing 0.3 mg buprenorphinum (Temgesic, Schering-Plough, Brussels, Belgium) was diluted in sterile water to a total concentration of 0.03 mg/ml. The solution was administrated subcutaneously at a dose of 0.1 ml per 20 g mouse, resulting in a total dose of 0.15 mg/kg. The effect lasted for approximately 6 hours.

3.2.3. Contrast agent

Gadopentetate dimeglutamine (Gd-DTPA) (Magnevist, Schering, Berlin, Germany) diluted in heparinized saline (produktnavn, sted, land) to 0.06 M was used as the contrast agent. Heparinized saline contained 500 IE of heparin per 100ml.

3.3. Animal model

3.3.1. Mice

Locally bred sexually mature male NCR nude mice (similar to commercially available BALB/c nude mice) weighing 25 – 35 g and aged 6 to 8 weeks old were used in this study. The National Committee on Research on Animal Care approved the animal protocol, and the experiment was performed according to Interdisciplinary Principles and Guidelines for the Use of Animals in Research, Marketing and Education (New York Academy of Science, New York, NY). The mice were kept under specific pathogen-free conditions at constant temperature (21.5 – 22.5 °C) and humidity (50 – 60 %). The mice were given sterilized food and water *ad libitum*. Mice were sacrificed by neck dislocation at the end of experiment.

3.3.2. Xenografts

The human androgen-dependent xenograft CWR22 was used. Tumor tissue measuring approximately $2 \times 2 \times 2\ (\text{mm})^3$ was subcutaneously implanted into the left flanks of the mice to generate CWR22 xenografts. Mice were anesthetized with zoletil solution before implantation.

The CWR22CA xenografts were achieved by androgen deprivation therapy using surgical castration of animals with CWR22 xenografts. At a shortest tumor diameter of 13 mm the animals were surgically castrated and allowed to partially regress until the shortest tumor diameter was 8 mm, before they were included into the experiment. Mice were anaesthetized with Zoletil solution and analgesized with Temgesic solution during the castration procedure.

Tumor volumes were estimated from caliper measurements two times a week from implantation until the end of the experiment using the formula $V = (length \times length \times width)/2$, with *length* being the longest diameter across the tumor and *width* the corresponding perpendicular.

3.4. PSA analysis

Blood to PSA analysis were collected from each mouse at day 0, day 1, day 9 and when the mice were sacrificed. A blood volume of 50 to 150 µl was collected from the tail vein using a non-heparinized capillary tube, before it was allowed to clot and centrifuged to collect serum. The serum was frozen at -80°C until PSA measurements were conducted. The ProStatus(tm) PSA Free/Total assay was used. It is a solid phase fluoroimmunometric assay based on the direct sandwich technique containing three monoclonal antibodies derived from mice. The principal scheme of the assay is showed in Figure 3.2. Europium-labeled antibodies directed against an antigenic site which is accessible only in free PSA are reacted with solid phase bound free PSA. Simultaneously, samarium-labeled antibodies directed against antigenic site common to both free and complexed PSA are reacted equimolarily with bound free and complexed PSA. Enhancement solution dissociates europium and samarium ions from the labeled antibody into solution where they form highly fluorescent chelates with components of the enhancement solution. The fluorescences in each well are then measured. The europium fluorescence of each sample is proportional to concentration of free PSA in the sample and the samarium fluorescence is proportional to the concentration of free and complexed PSA (total PSA) (Soini and Kojola 1983, Hemmila et al 1984, Lovgren et al 1985). Reference standards were used to calibrate the results.

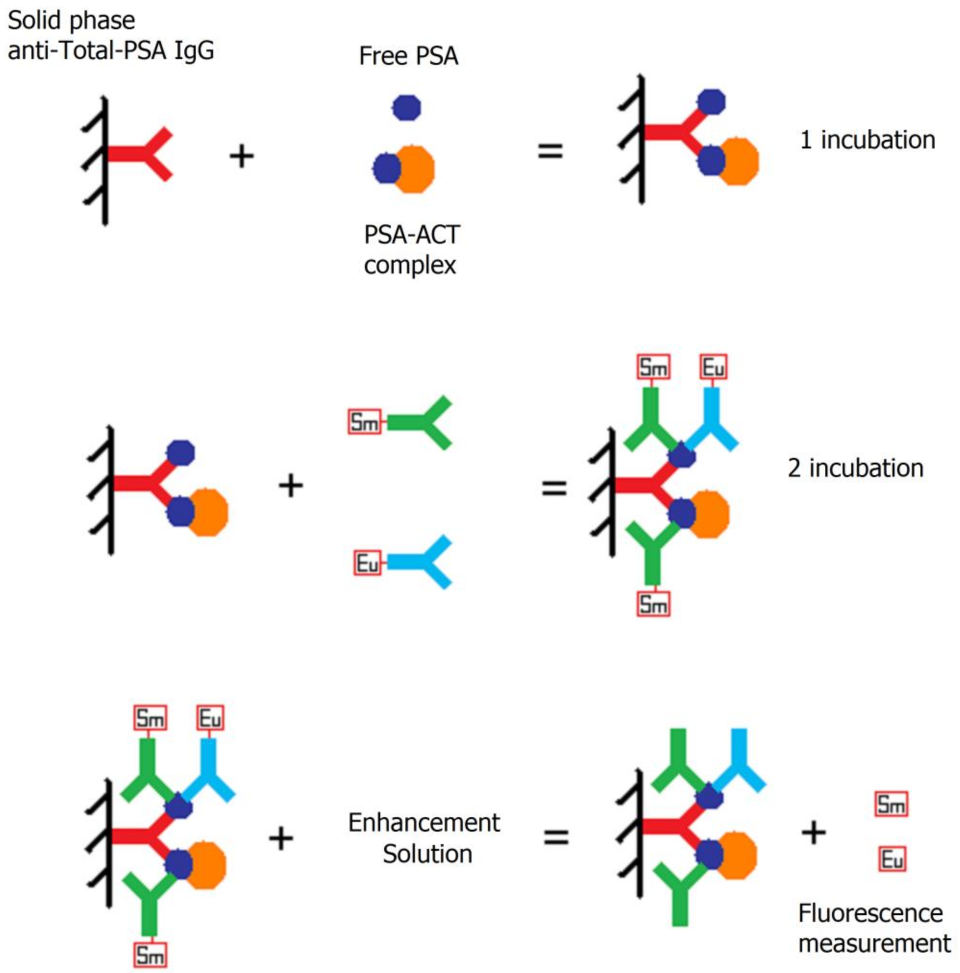

Figure 3.2.A scheme of The ProStatus (tm) PSA Free/Total assay used to measure PSA concentration in plasma.

3.5. Radiation therapy

The tumors in the two irradiation groups (groups 2 and 4) received a single fraction of 15 Gy on day 0 (after the MRI) using a ^{60}Co source (Mobaltron 80, TEM Instruments, Crawley, UK) having a dose rate of 0.6 Gy/min. The ^{60}Co source is contained inside a stainless-steel capsule sealed by a welding, which is placed in another steel capsule to prevent any leakage of the radioactive material, see Figure 3.3. The ^{60}Co source emits radiation when the ^{60}Co nucleus decays to ^{60}Ni by emission of β-particles and two photons per disintegration with energies of 1.173 MeV and 1.332 MeV. These γ-rays constitute the useful treatment beam. The β-particles are absorbed in the cobalt metal (Khan 1994)

Figure 3.3. The ^{60}Co-unit used in irradiation of the CWR22 and CWR22CA xenografts.

The megavolt beam produced by this cobalt source gives an initial dose buildup with depth, resulting in maximum dose at a depth of 4 mm. To achieve a homogeneous dose deposition within the tumor volume, a 5 mm thick polystyrene bolus was placed on top of the tumor. A bolus is a tissue-like material that compensates irregular contours and surface and creates a build-up region for reaching a maximum even dose in whole tumor. For the ^{60}Co unit at 80cm distance, the buildup dose distribution in polystyrene for a 10 x 10 cm field is givenin Table 3.1.

Depth, mm	Dose, % of max
0	18.0
1	70.5
2	90.0
3	98.0
4	100.0
5	100.0

Table 3.1: Buildup dose distribution in polystyrene for a 10 × 10 cm field by use of a ^{60}Co Unit (Khan 1994)

The ^{60}Co unit was initially measured the 15.09.1996, with the dose rate of $A^{-1}(0)=31.35$ s/Gy. Since ^{60}Co sorce is decaying, the dose rate is adjusted monthly according to the decay constant of the ^{60}Co source. Correct dose rate at the date of radiation, $A^{-1}(t)$, is calculated by the following formula (3.1)

$$A^{-1}(t) = A^{-1}(t_{15}) \cdot \frac{\ln 2}{T_h} \cdot n + A^{-1}(t_{15}) \quad (3.1)$$

where $A^{-1}(t_{15})$ is the dose rate at the 15th days of the last month, T_h is the half-life time of ^{60}Co (1925.1 days), and n the number of days since the 15th. The unit of dose rate is s/Gy. The radiation time in seconds was found by multiplying the dose rate $A^{-1}(t)$ with the dose in Gy.

During radiotherapy, only the tumor area of anesthetized mice was irradiated, whereas the rest of the body was kept outside the radiation field. Figure 3.4 shows mouse position in a radiation field represented on the picture by a square of white paper. In previous experiments (Røe 2006) measurement of dose in the center and the corner of the 10x10 square was made. The correct dose was found using a phantom, a plastic glove filled with water. The radiation field was adjusted to 10x10cm and the distance between source and phantom was 80 cm. In the center and in the phantom in the corner several TLD chips were placed. Measuremet showed that a central dose of 18.45Gy corresponded to 15Gy dose 1.5 cm into radiation field from the outer corner. When calculating radiation time a central dose was used. It was also showed that dose that dose outside the radiation field was 50 times lower than in the center. According to this, a mouse was placed in a radiation field as shown in figure 3.4. A tumor is positioned 1,5cm from outer corner, while the rest of the body placed outside the field.

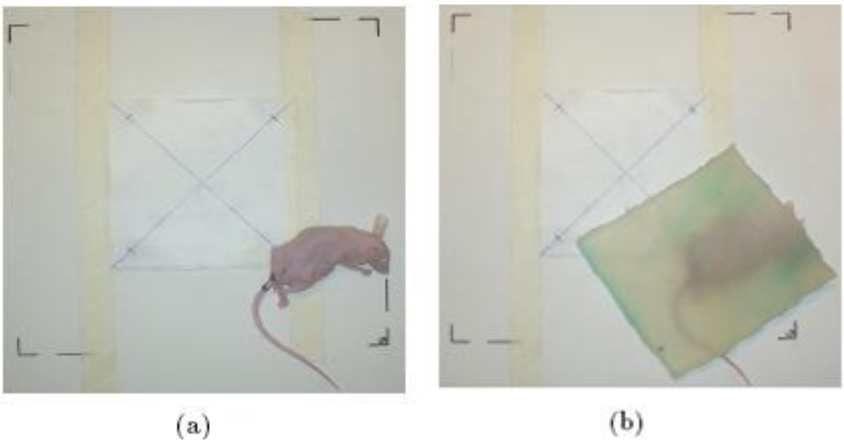

Figure 3.4. An illustration of a mouse in the radiation field (a), and a mouse with bolus (b). The white paper square was a guide for positioning of radiation field. Center of the field is marked with a cross. A tumor was positioned 1.5 cm from the outer corner, while the rest of the body was positioned outside the radiation field.

3.6. Magnetic resonance

3.6.1. Preparation for MR acquisition.

First, the mice were weighed to calculate the amount of contrast agent (0.1 ml/10 g of body weight).Then, the mice were anesthetized and eye ointment was applied. A heparinized 24-gauge catheter was inserted into the tail vein and attached to a cannula containing the saline-diluted Gd-DTPA. The mouse was placed in a stretcher made of extruded polystyrene thermal insulation material (Styrofoam) as shown in Figure 3.5. The loaded mouse coil was tuned with a vector impedance meter (Hewlett Packard 4193A) to 63.89 MHz. This frequency is the Larmor frequency of the protons at 1.5 T, whose resonance signal is being detected. The tuning matches the MR system before acquisition of data and results in a higher output signal and minimizes losses due to external sources with other frequencies.

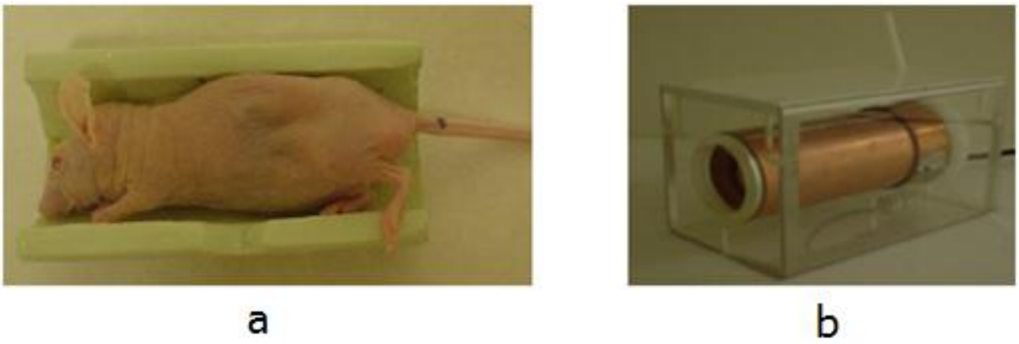

Figure 3.5. (a) An illustration of a mouse in the stretcher before placement in the MR coil, and (b) the mouse coil used in the MR experiments.

3.6.2. MRI acquisition

MR imaging was performed using a 1.5 T whole-body clinical MR system (Signa, General Electrics, Milwaukee, USA) at the MR facility at Rikshospitalet-Radiumhospital HF (Oslo university hospital at the present moment) (Figure 3.6). The volume to be excited in imaging of mice is substantially less than the volume to be excited in clinical imaging of patients. Thus, the transmitted signal was attenuated with 30 dB during all experiments. The mouse coil was attached to the clinical MR scanner in the connector for standard transmit/receive extremity coils used for MR. The coil was placed in the iso-center of the MR scanner. The temperature of the mouse was maintained at 38°C during acquisition using a water-heating pump with warming pad around the coil.

Figure 3.6. The 1.5 T clinical MR scanner used in the experiments. A mouse coil from figure 3.5(b) is placed outside the magnet.

The excitation field B_1 must be perpendicular to the main magnetic field B_0, hence themouse coil was placed as illustrated in Figure 3.7.

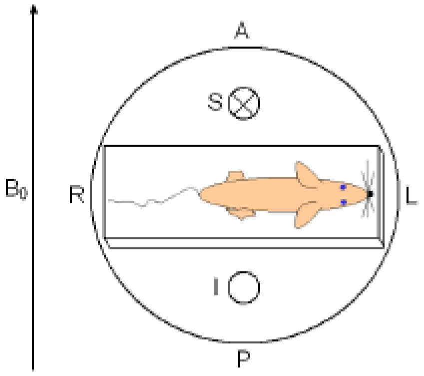

Figure 3.7. Placement of the mouse and mouse coil in the MR scanner. The excitation field of the coil, B_1, is perpendicular to the main magnetic field, B_0. A = anterior, P = posterior, R = right, L = left, S = supine, and I = inferior.

The MR-protocol given in Table 3.2 was used for all investigations. All imaging parameters were kept the same throughout the experiment.

Table 3.2 The MR-protocol

Sequence No	Type of sequence	Scan time
1	Localization	0:41
2	T2-weighted image	2:40
3	Tensor diffusion images with b = 0 and 50 s/mm^2	1:05
4	Tensor diffusion images with b = 0 and 100 s/mm^2	1:05
5	Tensor diffusion images with b = 0 and 300 s/mm^2	1:05
6	Tensor diffusion images with b = 0 and 600 s/mm^2	1:05
7	T2-weighted image	1:10
8	Proton density images	0:25
9	Dynamic T1-weighted images (DCEMRI)	21:00
10	Proton density images	0:25

Localization

An axial fast gradient-echo sequence gave 3 dimensional images of the mice in the axial, coronal and sagittal directions. The acquisition was performed with an acquisition matrix of 256 x 128, 5 mm slice thickness and 2 mm slice gap. Illustration images in three dimensions are shown in Figure 3.8.

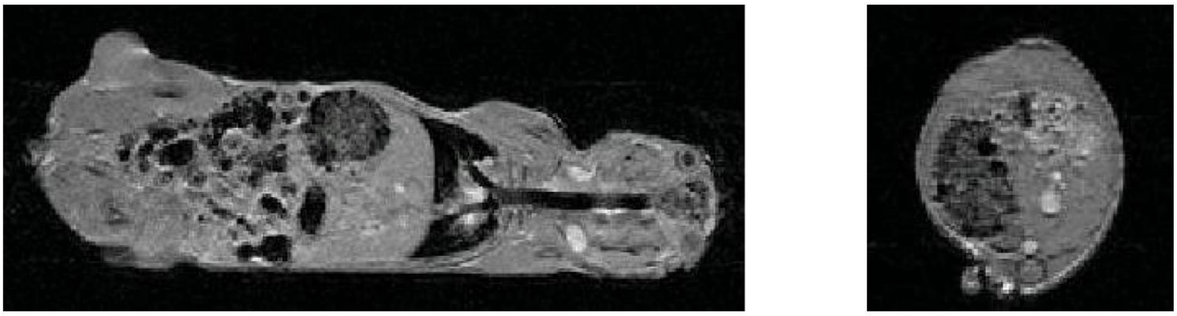

(a) Sagittal (b) Axial

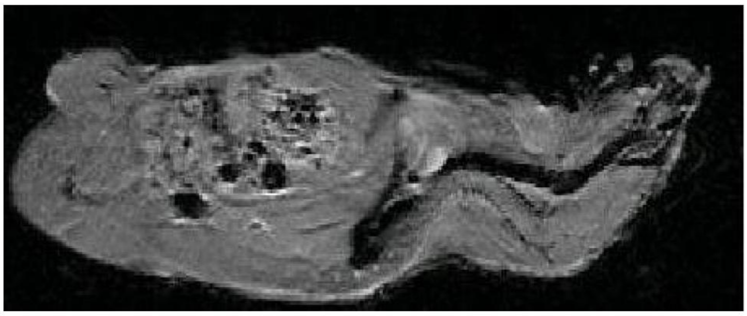

(c) Coronal

Figure 3.8. (a) Images of a mouse in the sagittal direction, (b) the axial direction and (c) a in the coronal direction.

T2-weighted image

Axial 2D T2-weighted images were obtained using a fast spin-echo sequence. These imageswere used to locate the slice with the largest tumor area, which are imaged in all subsequent acquisitions. The acquisition was performed with an acquisition matrix of 256 x 256, TE/TR = 85 ms/4000 ms, 2 mm slice thickness, 2 mm interslice gap, bandwith (BW) of 15.63 Hz, echo train length (ETL) of 16 and field of view (FOV) = 4 cm.

Diffusion tensor images

A single shot fast spin echo (SSFSE) sequence providing diffusion weighting in the direction of slice selection was used. This acquisition provided images without the significant degreeof spatial distortions that affect EPI-based diffusion imaging. The DTI-SSFSE sequence used in the experiments contained six gradient directions ([1 0 1], [-1 0 1], [0 1 1], [0 1 -1], [1 1 0] and [-1 1 0]) in addition to the zero gradient ([0 0 0]). This enabled calculation of the diffusion tensor and its eigenvalues, λ_1, λ_2 and λ_3. The acquisition was performed with an acquistion matrix of 256x256, TE/TR = 78.7 ms/5000 ms, BW = 15.63 Hz, ETL = 16, 2 mm slice thickness, 1 mm interslice gap and FOV = 14 cm. DTI acquisitions were performed 4 times by using 4 combinations of b-values: 1) $b_1 = 0$ s/mm^2 and $b_2 = 50$ s/mm^2; 2) $b_1 = 0$ s/mm^2 and $b_2 = 100$ s/mm^2; c) $b_1 = 0$ s/mm^2 and $b_2 = 300$ s/mm^2; and d) $b_1 = 0$ s/mm^2 and $b_2 = 600$ s/mm^2.

T2-Weighted Image

After the diffusion tensor imaging an addition axial 2D T2-weighted image serie was obtained using a fast spin-echo sequence with the same dimensions as the diffusion series (FOV = 14 cm), to be able to calculate ADC maps. The rest of theing parameters were identical to the first T2-serie in the exam.

Proton density image

Proton density images (TE = 4.4 ms, TR = 360 ms, image matrix = 256 x 128, FOV = 6 cm, slice thickness = 1 mm, FA = 10°) were acquired of the tumors central slice prior to and after the dynamic contrast-enhanced imaging to determine the maximal signal intensity S_{max}

DCEMRI acquisition

DCEMRI was performed on the tumors central slice using a dynamic fast spoiled gradient-recalled (FSPGR) T1-weighted images (TE = 6.3 ms, TR = 120 ms, image matrix = 256 × 128, FOV = 6 cm, slice thickness = 1 mm, flip angle (FA) = 80°). Following acquisition of 5 pre-contrast image data sets, the Gd-DTPA was manually injected during 3 seconds. The dynamic imaging continued with 100 post-contrast images with a time resolution of 12 seconds, totally 20 min post-contrast imaging. The reconstructed voxel size of the T1-weighted images was $0.23 \times 0.47 \times 1$ mm^3.

Sequence used for vascular input function determination

The imaging slice was positioned in the center of left ventricle. The protocol was identical as for DCEMRI except for TR = 200 ms for the proton density images, and TR = 80 ms, image matrix = 512 × 256 and slice thickness = 2 mm for the T1-weighted images, giving a voxel size of $0.11 \times 0.23 \times 2$ mm^3. The T1-weighted imaging consisted of 120 post-contrast images acquired every 10 seconds.

3.6.3 DCEMRI analysis

Acquired images were stored on the DICOM format and transferred to IDL (Interactive Data Language v6.2, Research Systems Inc., Boulder, CO) where all further analyses were performed using programs written in-house. Gd-DTPA concentrations were calculated from signal intensities and proton density images using the method of Hittmair *et al* (Hittmair et al 1994). They suggested using of a parameter called “enhancement factor”, EF, which can be determined as shown in equation 3.2.

$$EF = \frac{1}{K \cdot TR} \ln\left(\frac{S_{\max} - S_{nat}}{S_{\max} - S_{pc}}\right) \approx \Delta R_1 = const \cdot C \tag{3.2}$$

where K is a flip angle correction factor listed in work of Hittmair et al (Hittmair et al 1994), TR repetition time, S_{max} is maximal signal intensity, S_{nat} is signal intensity prior the contrast administration, S_{pc} is signal intensity after contrast administration, ΔR_1 is changes in relaxation rate due to contrast agent administration, C is concentration of constart afent, *const* is proportionality constant.

Maxiamal signal intensity S_{max} was determined from proton density images with low flip angle (FA=10°). Signal intensity on proton density images is dependent on proton density and flip angle as showed in equation 3.3

$$S = N(H) \cdot \sin\alpha \qquad (3.3)$$

where S is signal intensity, N(H) is proton density and α is a flip angle.

Maxiaml signal intensity S_{max} for DCE-MRI sequence is determined by equation 3.4

$$S_{\max} = N(H) \cdot \sin 80° = S_{\alpha=10°} \cdot \frac{1}{\sin 10°} \cdot \sin 80° \qquad (3.4)$$

To determine the proportionality constant *const* 2 reference phantoms one with water to simulate native tissue and another with water containeng 0.06M of Gd-DTPA to simulate contrast enhanced tissue. After calculation of EF according to equation 3.2, *const* can be as shown in equation 3.5

$$const \approx \frac{EF}{C} \qquad (3.5)$$

where *C* is concentration of Gd-DTPA in the phantom. Concentration of contrast agent in mouse tissue C_t can be approximated as EF/*const*.

From the mice subjected to left ventricle imaging, individual AIFs were determined fitting a biexponential function to the calculated Gd-DTPA plasma concentration curves as showen in equation 3.6:

$$Cp(t) = A\,exp(-Bt) + C\,exp(-Dt) \qquad (3.6)$$

where *A* and *B* reflect the equilibration of Gd-DTPA between plasma and extracellular space, *C* and *D* represent the kidney clearance of Gd-DTPA and $(A + C)^{-1}$ (l/kg) represents the plasma volume of the mouse per unit of body weight. The mean of the eight separate AIFs gave a single AIF with the following numerical constants: A = 3.57 ± 0.34 mM, B = 0.025 ± 0.005 sec^{-1}, C = 1.45 ± 0.15 mM, D = 0.0074 ± 0.0036 sec^{-1}, which was assumed to be valid for all mice in the experiment. Using the AIF parameters and Gd-DTPA concentration versus time curves for each voxel within the tumor region-of-interest (ROI), each individual voxel was fitted to the Tofts and Kermode model (Tofts 1997) using equation 3.7:

$$C_t(t) = Dk_{trans}\left[\left(\frac{A(\exp(-Bt) - \exp(-k_{ep}t))}{k_{ep} - B}\right) + \left(\frac{C(\exp(-k_{ep}t) - \exp(-Dt))}{D - k_{ep}}\right) \right] \quad (3.7)$$

where D is dose of GD-DTPA injected. It should be noted that Equation 3.7 assumes that plasma volume in tissue is 0 and do not contribute to overall enhancement.

Applying equation 3.7 a voxel-wise estimations of the forward volume transfer constant for Gd-DTPA between blood plasma and the EES (K^{trans}) (Tofts et al 1999), across the tumor was made. Unfitted voxels comprised those were the fit failed to converge due to low Gd-DTPA uptake or voxels giving values classified as nonphysiological ($K^{trans} < 0$, $K^{trans} > 0.01$ sec^{-1}). Unfitted voxels were normally in the center of the tumor, probably as a result of poor vascular supply in hypoxic or necrotic areas. On the basis of their low perfusion, the unfitted voxels were included in the K^{trans} maps as zeros, and therefore contributed in calculation of tumor mean K^{trans}. The percentage of unfitted voxels, scored as the ratio of unfitted voxels versus the total number of voxels within the tumor ROI, was monitored for all tumors in the experiment.

3.6.4 Diffusion analysis

The obtained image data were transferred to a remote computer where quantitative diffusion measurements were obtained by calculation of ADC by using the software nICE (Nordic Ice Medical AS, Bergen, Norway). For the central slice of the tumor, ROIs were drawn on the T2-weighted images corresponding to trace-value maps. The ADC for each ROI was calculated automatically as (Mean ± SD). ADC for b value of 50, 100, 300 and 600 s/mm^2 were calculated relative to b=0 s/mm^2 using equation 3.8:

$$ADC = \frac{1}{b}\ln\left(\frac{S_0}{S_b}\right) \quad (3.8)$$

where S_0 is the signal intensity without diffusion weighting, and S_b is the signal intensity with diffusion gradient.

3.7. Statistical analysis

Statistical analysis was performed using SPSS 17.0 (SPSS, Cary, NC). One-Sample Kolmogorov-Smirnov Z test was used to test the assumption of normal distribution. For normal distributed data results were presented as the mean value and standard error of the mean (SEM) of each group. Pearson’s correlation test was used to analyze whether correlations between variables were significant. All data were analyzed both by grouping all values within treatment groups (*t*-test) and by comparing mean individual animal data obtained pre- (day 0) and post-treatment (day 1 and day 9) (paired *t*-test), under conditions of normality. Data was presented in the form of mean and standard errors of the mean (SEM).

Chapter 4

Results

4.1 Animals used in experiment

The total number of mice used in the experiment was 80. Only 73 of them developed a tumor suitable for the experiment. In table 4.1, the total number of mice included into the experiment, mice dead after castration, radiation treatment or under MRI procedure are presented.

Table 4.1 Overview of the mice used in experiment.

Group name	Total number of mice	Died after castration	Sacrificed because of failed regression after castration	Died after radiation treatment	Died during MRI acquisition	Sacrificed because of other health-related reasons	The number of mice used for data collection
CWR22 control	9	-	-	-	1	0	8
CWR22 irradiated	9	-	-	1	0	0	8
CWR22CA control	55	9	10	-	2	7	9
CWR22CA irradiated				2	2	5	9
Total	73	9	10	3	5	12	34

4.2. Tumor growth

Pretreatment tumor volumes of all tumors used in experiment were normally distributed ($p = 0.71$) with a mean tumor volume of 400 ± 37 mm^3.

Pretreatment tumor volumes for CWR22 group were normally distributed ($p=0.39$) with a mean tumor volume of 276 ± 40 mm^3. Figure 4.1 shows the growth curves for untreated and irradiated CWR22 tumors. Exponentially growing CWR22 control tumors reached endpoint of experiment in 28 days. The tumors in the CWR22 irradiated group showed a 31% volume decrease ($p<0.01$) as compared to pre-treatment volumes 24 hours after treatment, before a renewed growth was seen from day 1 to day 9. Then, the tumors started to regress, and a lowest volume of 128±24 mm^3 at day 41 was reached before a renewed growth appeared. At day 69, two tumors reached 16 mm in largest diameter and all animals in the group were sacrificed. The mean tumor volume of this group was 528±145 mm^3 at the time of sacrifice. At day 23, the mean tumor volume of irradiated tumors was 5.3-fold less ($p<0.01$) than the mean tumor volume of CWR22 control tumors.

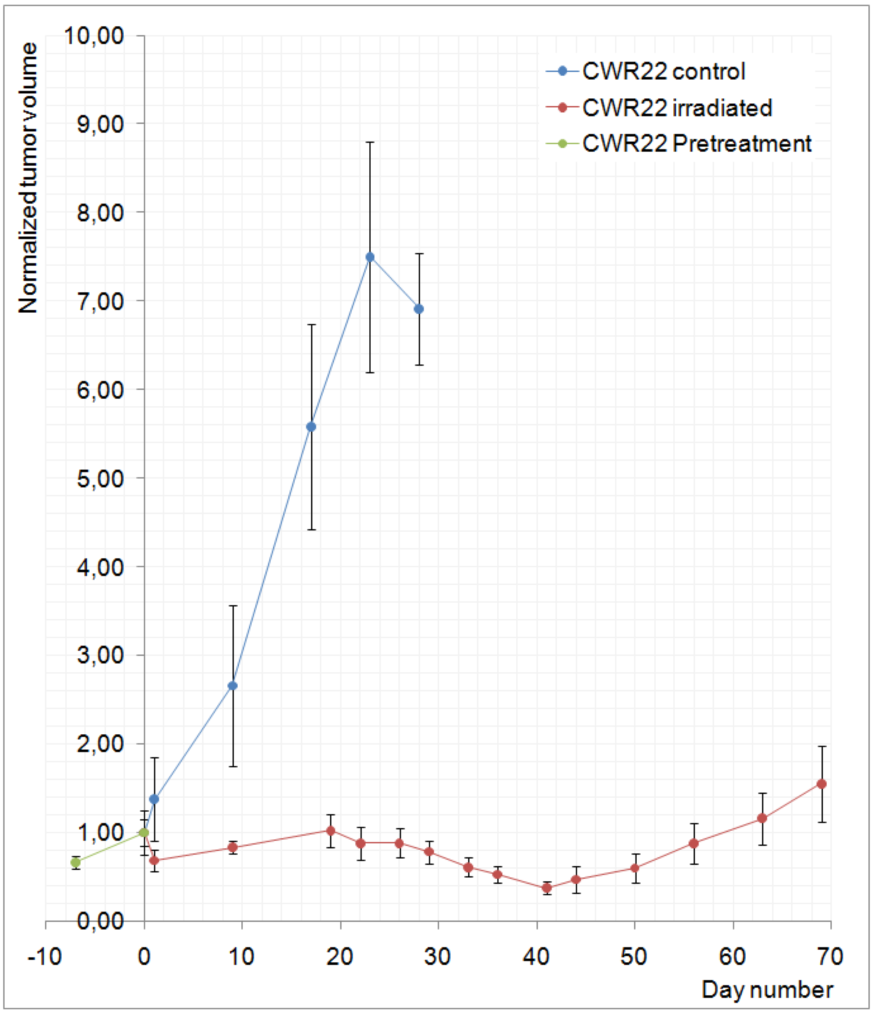

Figure 4.1 Tumor volume (mean±SEM) for CWR22 control and CWR22 irradiated groups normalized to tumor volume at day 0. Radiation treatment was performed at day 0 after an initial pre-treatment MRI.

Pretreatment tumor volumes for CWR22CA group were normally distributed ($p=0.643$) with a mean tumor volume of 500±47 mm^3. Figure 4.2 shows growth curves for CWR22CA tumors. Animals were castrated 32±3 days before the pre-treatment MRI. At the day of pretreatment MRI mice were randomized and separated into 2 groups, control and radiation treated. Mice in both groups reached experiment endpoint after 31±1 days after pre-treatment MRI. Volumes of tumors in the CWR22CA groups decreased continuously as long as the experiment lasted. Tumors in CWR22CA control group showed insignificant decrease in tumor volume at days 4, 7 and 10 compared to pre-treatment values, while a 47% ($p<0.01$) and 41% ($p<0.01$) decrease in tumor volume was observed for days 26 and 30, respectively. No significant difference was observed comparing tumor volumes at day 26 and 30.

CWR22CA irradiated tumor showed a 34% decrease in tumor volume already at day 10 (p=0.03), followed with a 61% decrease at day 20 (p<0.01), 70% at day 26 (p<0.01) and 67% at day 30 (p=0.01) compared to pre-treatment values. No significant difference between tumor volumes at day 20, 26 and 30 for CWR22CA irradiated group was observed.

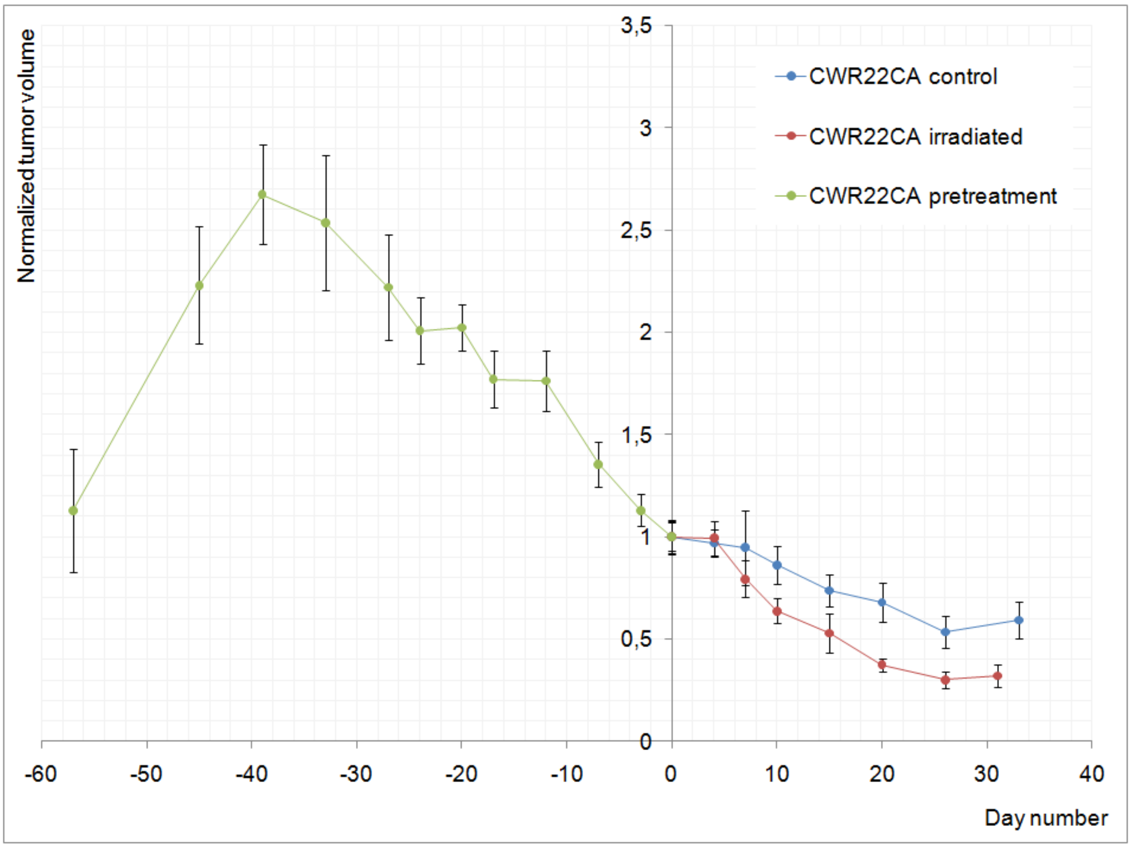

Figure 4.2 Tumor volume for CWR22CA control and CWR22CA irradiated groups normalized to the tumor volume at day 0. Radiation treatment was performed at day 0 after an initial pre-treatment MRI.

4.3 Histology

Figure 4.3 and 4.4 shows histological section of tumor tissue obtained after the mice were sacrificed at the end of the experiment. Macroscopic examination shows that CWR22 control tumors are necrotic and heterogeneous, with necrotic areas localized over the whole tumor cross section. The tumors had clear zones of viable tumor cells (arrow 1, figure 4.3.a and b). It has an organization of a glandular tissue, forming layer structure around blood vessel, with a layer of elongated cells (arrow 2, figure 4.3.a and b). It has a shape of typical columnar epithelium with nucleus located in distal part of the cell, but no basal membrane is present. These structures are surrounded with human tumor cells (arrow 3, figure 4.3.b) with large nucleus. Parts of glandular tissue surrounded with connective tissue that consists of mouse cells (arrow 4, figure 4.3.a).

In figure 4.3.c and d, histological sections of tumor from CWR22 irradiated group are presented. Unlike CWR22 control tumors, no structural epithelial patterns were observed. Tissue consisted primary of human tumor cells with blood vessels and small fraction of connective tissue, primary muscle cells. Tumor cells seem to be smaller, mainly because a less cytoplasm volume having the same nucleus size. A large number of cavities can be noticed (figure 4.3.c, arrow 5).

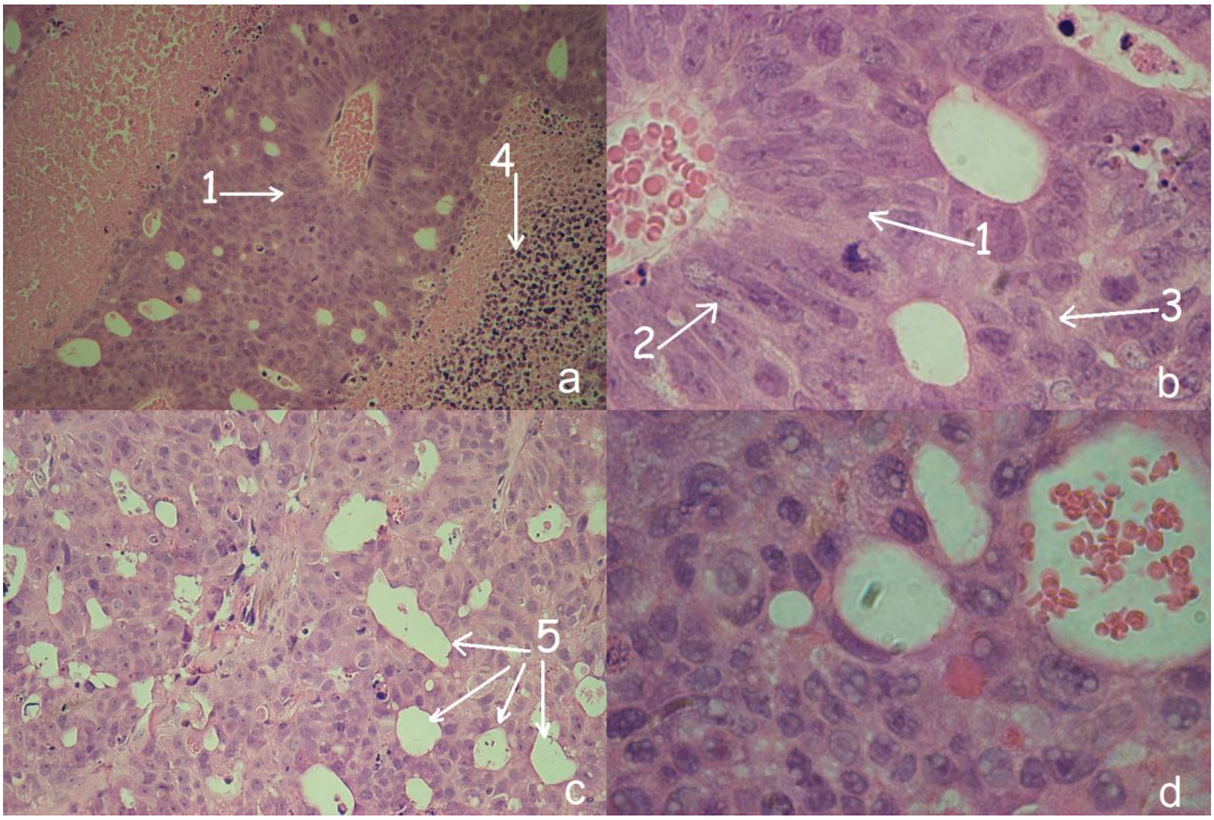

Figure 4.3 CWR22 control and irradiated group tumor sections died with hemaetoxilin and eosin. Panel a) and b) is CWR22 control group, magnification 10X and 40X respectively. Panel c) and d) is the CWR22 irradiated group.

In figure 4.4 histological sections for the CWR22CA groups are presented. Macroscopically, tumors from both groups were flat, and more compact and solid. Histological sections of CWR22CA control showed that the tumors consisted mainly from human tumor cells (figure 4.4.a, arrow 1), but in comparison to CWR22 control group the cells were smaller. In addition to tumor cells a large fraction of mouse fibrosis cells were present (figure 4.4.a, arrow 2). On sections from CWR22CA irradiated tumors the cells were even more compact. A large fraction of mouse fibrosis cells were present (figure 4.4.c, arrow 3). In figure 4.4.c multiple cavities can be seen (arrow 4), the same as in sections for tumors from CWR22 irradiated group.

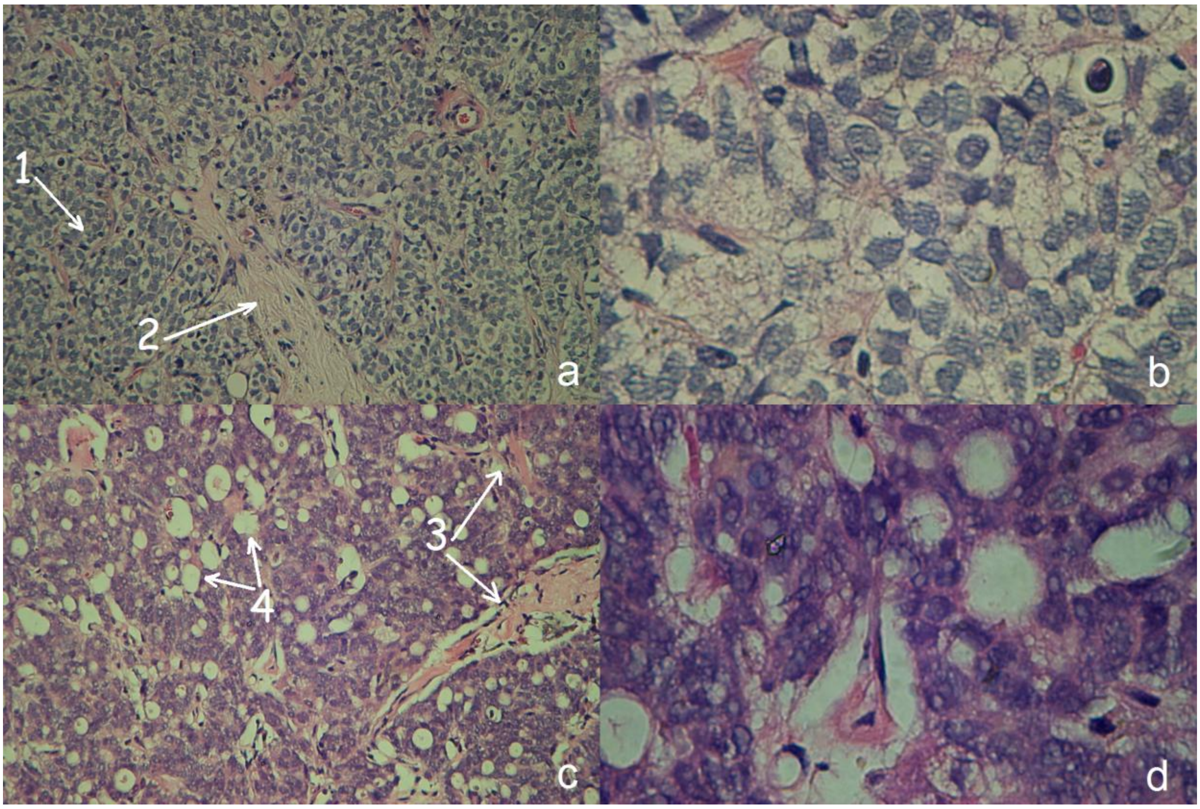

Figure 4.4 CWR22CA control and irradiated group tumor sections died with hemaetoxilin and eosin. Panel a) and b) is tumor section for CWR22CA control group, magnification 10X and 40X respectively. Panel c) and d) for CWR22CA irradiated group.

3.4. PSA analysis

Mean pre-treatment concentration of total PSA in blood was 28.0 ± 2.1 ng/ml and 16.2 ± 3.1 ng/ml for the animals bearing CWR22 and CWR22CA tumors respectively. For CWR22 control group total PSA concentration continued to increase along with tumor growth (day 1: 41,6 ± 6,9 ng/ml ($p=0.12$) day9: 88,2±12,2 ng/ml ($p<0.01$) end-point: 2124±13,8 ng/ml ($p<0.01$)) (Figure 4.5), but total PSA blood concentration normalized for tumor volume showed no significant changes over time (Figure 4.7). For CWR22 irradiated group PSA concentration increased more slowly than for CWR22 control group (day 1: 44,1±8,3 ng/ml ($p=0.06$) day 9 48,4±9,7 ng/ml ($p<0.01$) end-point: 75,8±17,4 ng/ml ($p<0.01$)). Normalized PSA blood concentration showed an increase for two consecutive measurement days (145% ($p<0.01$) at day 1 and 112% ($p<0.01$) at day 9) compared to pretreatment values. At the last day of experiment for this group normalized PSA blood concentration was 87% higher ($p=0.07$) than pretreatment concentration. There was no significant difference in normalized total PSA concentration for CWR22 control and irradiated groups at the same experiment days.

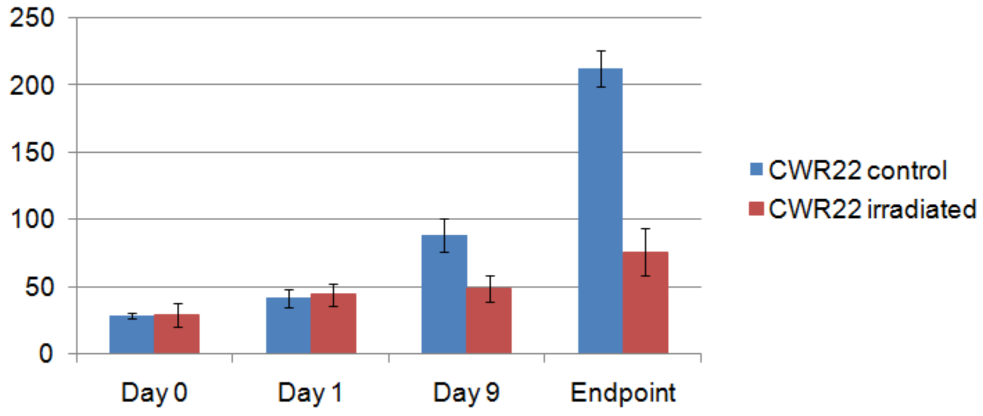

Figure 4.5 PSA blood concentration (mean ± SEM) for CWR22 control and irradiated groups, ng/ml.

In the animals bearing CWR22CA tumors the total PSA concentration was reduced in all subsequent measurement days compared to CWR22 groups. No significant difference was observed for both groups at day 0, 1 and 9 comparing within each group for consecutive days or between groups. The decrease in total PSA concentration from day 9 to the end-point of experiment was significant for both the control and the irradiation group (63% decrease, $p < 0.01$ and 94 % decrease, $p = 0.01$, respectively) (Figure 4.6).

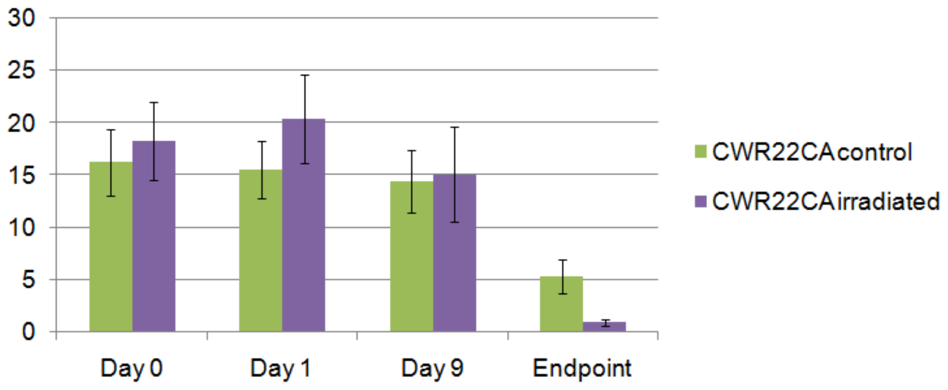

Figure 4.6 PSA blood concentration(mean ± SEM) for CWR22CA control and irradiated groups, ng/ml.

There was no significant difference in total PSA concentration normalized to tumor volume for CWR22CA control and irradiated groups at day 1 and 9 compared to pretreatment values. At the last day of experiment a decrease of 55% (p=0.01) for CWR22CA control and 89% (p<0.01) for CWR22CA irradiated groups were observed compared to pretreatment values. Normalized PSA concentration for CWR22CA control group was 3.7-fold higher (p=0.04) than for the CWR22CA irradiated group.

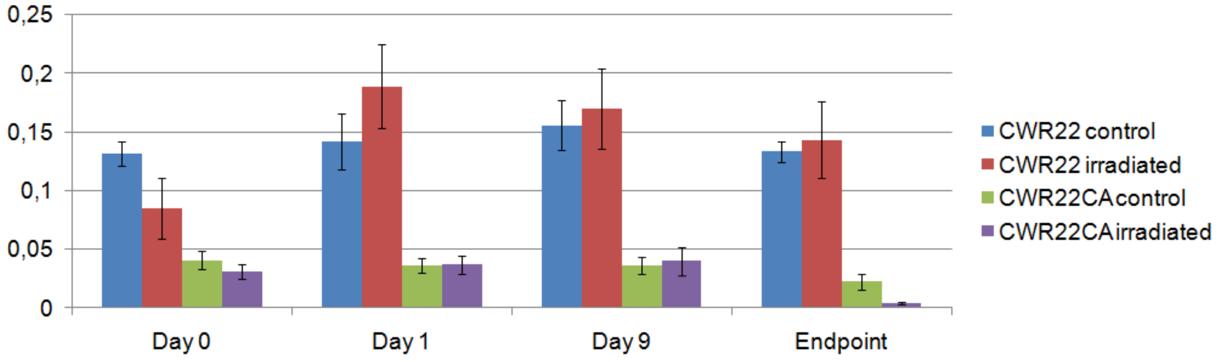

Figure 4.7 PSA blood concentration (mean ± SEM) for all groups normalized to tumor volume, ng x ml^{-1} x mm^{-3}

Free PSA blood concentration was increasing for CWR22 control group from day 0 to the end of experiment, reaching a value 4.5 times higher (p=0.01) than pretreatment value. There were no significant changes for CWR22 irradiated group. For CWR22 control group compared to CWR22 irradiated group concentration was 1.73-fold higher at day 9 after irradiation (p=0.04) and 4.89-fold higher at the end of experiment (p=0.03).

A 10% reduction at day 9 (p<0.01) and 64% reduction at the end of experiment (p<0.01) compared to pretreatment values was observed for CWR22CA control group. For CWR22CA irradiated group the reduction was 60% at day 9 (p<0.01) and 92% at the end of experiment (p<0.01) compared to pre-treatment values. Free PSA concentration was 4.3-fold higher (p=0.04) for CWR22CA control than irradiated groups at the end of experiment. Being the same for to pretreatment day and 24 hour after irradiation (p<0.01), free PSA concentration was higher for both CWR22 groups compared to CWR22CA groups (p<0.01) at day 9 and at the end of experiment.

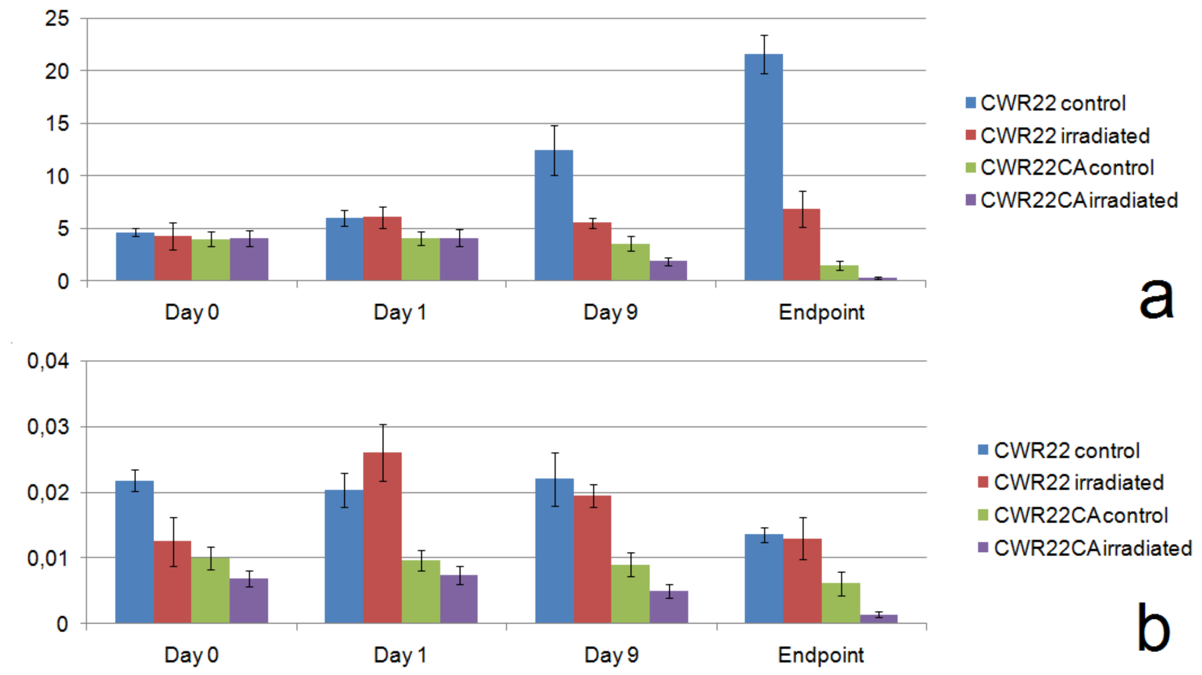

Figure 4.8 a) Free PSA blood concentration (mean ± SEM) for CWR22 and CWR22CA control and irradiated groups, ng/ml. b) Free PSA blood concentration (mean ± SEM) for CWR22 and CWR22CA control and irradiated groups normalized to tumor volume, ng x ml^{-1} x mm^{-3}.

The was no significant changes in the fraction of free PSA to total PSA for any group compared to pretreatment values or irradiated groups to control. Proportion of free PSA for CWR22CA groups was 1.5-3 times higher than for CWR22 groups, but the difference was not significant.

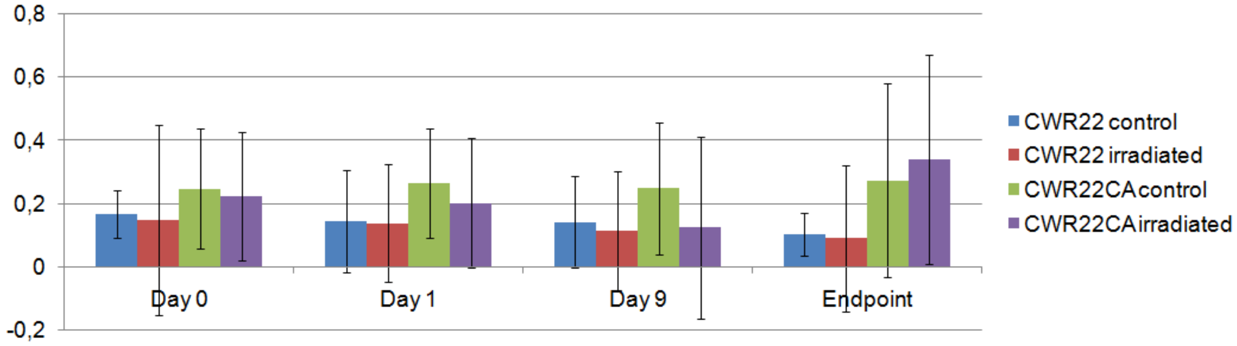

Figure 4.9 Proportion of free PSA versus total PSA (mean ± SEM) for CWR22 and CWR22CA control and irradiated groups, ng/ml.

There was a significant positive correlation (r=0.62, p<0.01 figure 3.10) between tumor volume and total PSA blood concentration. The correlation was stronger for animals with CWR22 tumors (r = 0.74, p < 0.01) than for animals with CWR22CA tumors (r = 0.27, p

= 0.03). It was a linear dependence between total PSA blood concentration and tumor volume (r=0.39, p<0.01) (Figure 4.10).

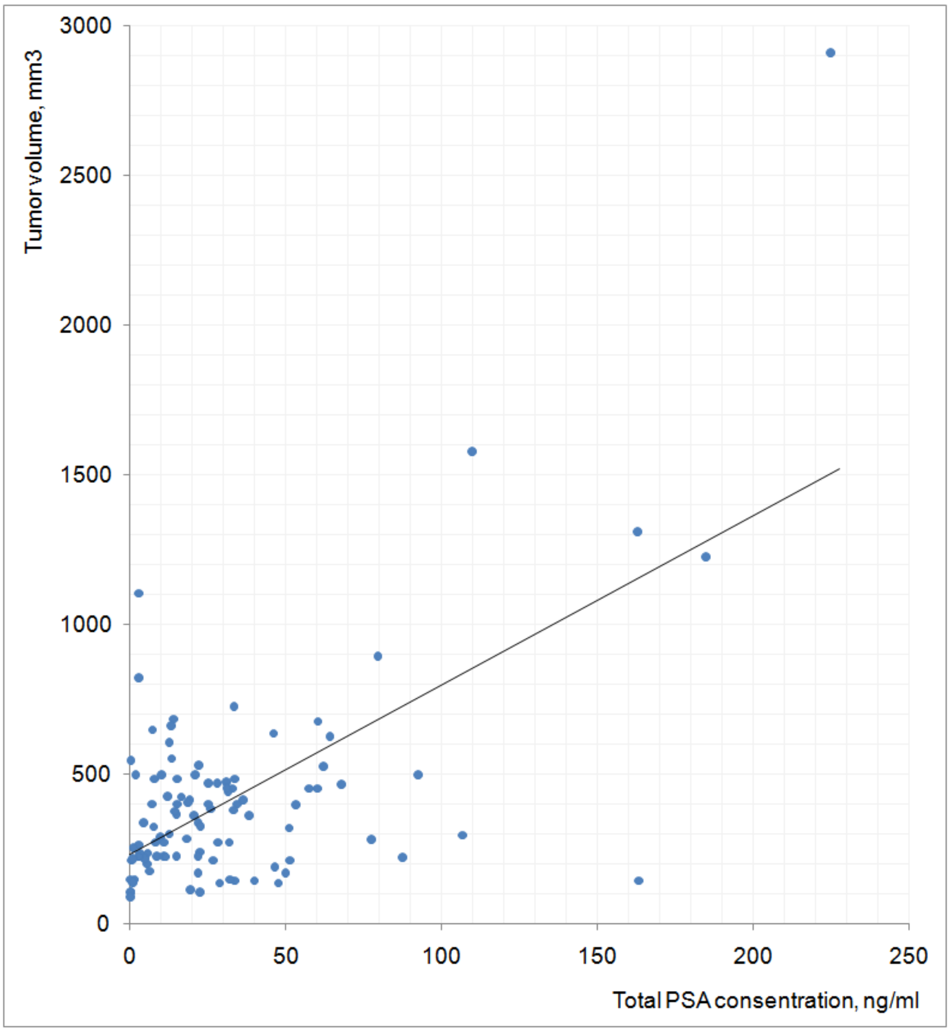

Figure 4.10. Correlation between total PSA concentration in blood (mean ± SEM) and tumor volume (mm^3), all data used (r=0.62, p<0.01).

When data from mice with untreated tumors only (non-castrated non-radiated mice) was used for analysis a significant strong positive correlation (r=0.73, p<0.01) between total PSA concentration and tumor volume were achieved (Figure 4.11).

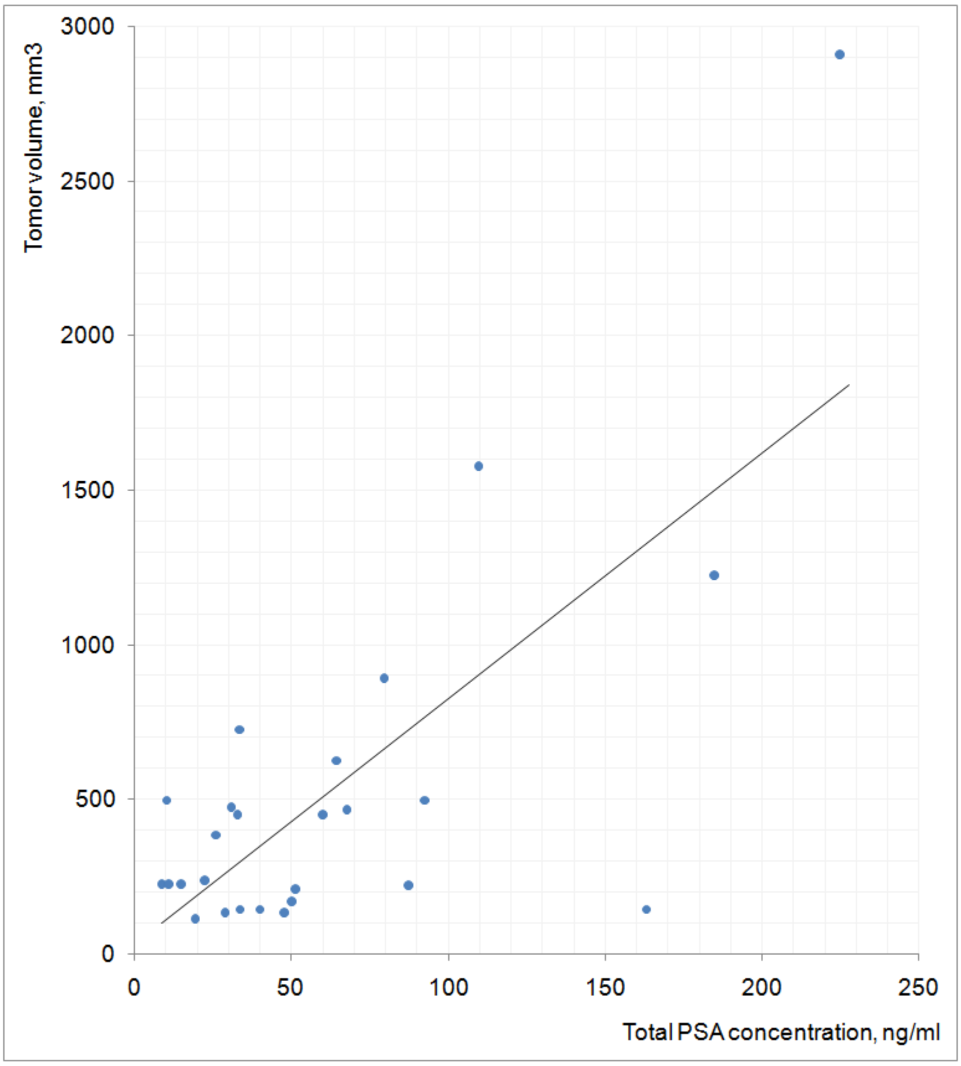

Figure 4.11 Correlation between total PSA concentration in blood (mean ± SEM) and tumor volume (mm^3), data from non-castrated control mice used ($r=0.73$, $p<0.01$).

4.5. DCEMRI results

4.5.1. Qualitative assessment of DCEMRI

Using concentration uptake curves (Figure 4.15 and 4.17) obtained from each tumor voxel together with the VIF parameters, parametrical maps of K^{trans} (s^{-1}) were generated using Tofts and Kermode modeling. A parametrical map is presented to the right along with respective post-contrast anatomical T1-weighted MR image (Figure 4.12). Manually selected ROIs (white line) showed on both MR image and on corresponding K^{trans} map. The dark blue areas within the tumor ROI on parametrical map are 0-value voxels. It is voxels which failed to fit with the model. The reason for it will be discussed in the discussion chapter. A color scale is presented to the left, with blue color equal to K^{trans} value of 0, dark red is the highest K^{trans}.

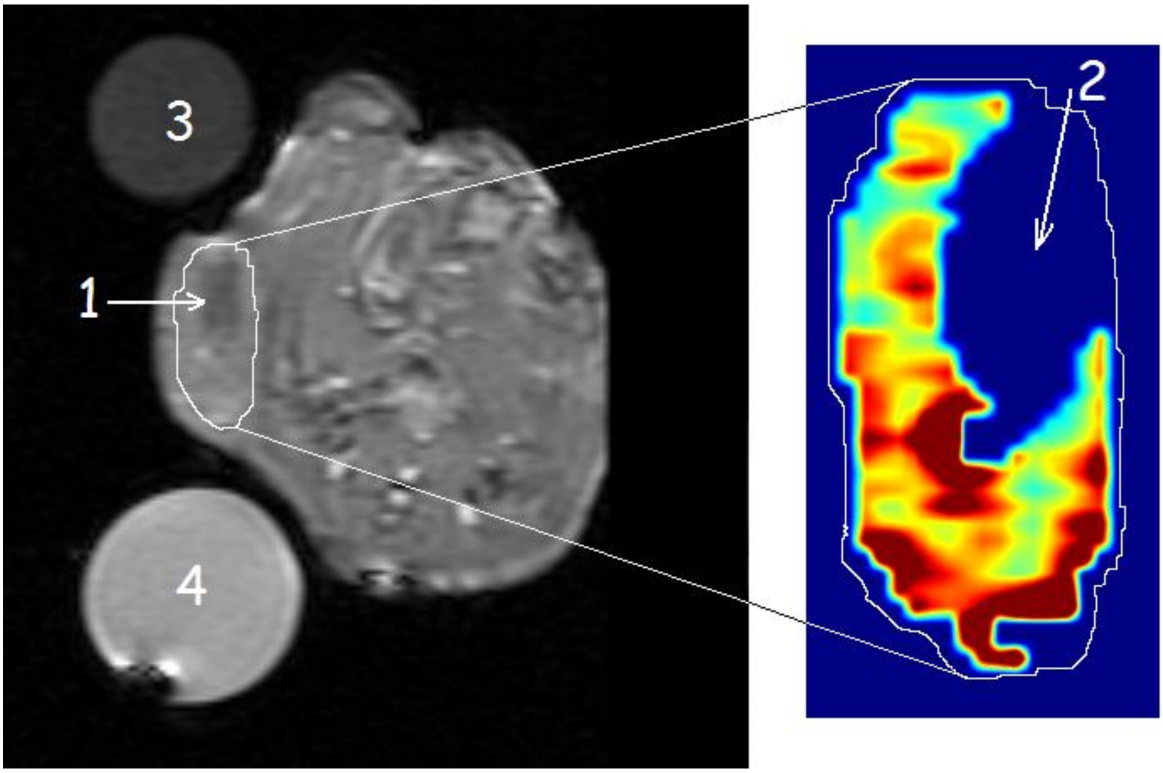

Figure 4.12 A post-contrast anatomical T1-weighted MR image with manually marked ROI and a corresponding K^{trans} parametrical map for a mouse from CWR22 irradiated group (5) at day 9. The necrotic area (arrow 1) on the MR image corresponds to the unfitted area on the parametrical map (arrow 2). Water phantom (3) and phantom with water doped with GD-DTPA (4) placed on 2 opposite sides of the tumor

In figure 4.13. K^{trans} maps for 2 mice from CWR22 control and irradiated groups from day 0, day 1 and day 9 are presented. There was no significant difference in appearance of parametrical maps for CWR22 control group at day 0 and 1. Mean K^{trans} value were $(0.036\pm0.001)\text{x}10^{-3}\text{s}^{-1}$ and $(0,035\pm0,001)\text{x}10^{-3}\text{s}^{-1}$ respectively. There were almost no unfitted voxels, with the fraction of unfitted voxels being 4.3% and 1.5% respectively. On day 9 the fraction of unfitted voxels increased to 23.8%. The value of unfitted voxels was set to 0 and can be seen as dark blue areas on both K^{trans} and V^{e} maps.

These changes can also be observed on concentration-time curves. Fast signal enhancement was observed in the T1-weighted MR images in the peripheral regions of the tumors, whereas signal enhancement in central regions was slower. The mean tumor contrast-enhancement was starting to decrease for all tumors 20 min after Gd-DTPA injection, when the collection of dynamic data was stopped, but not down to pre-contrast values.

The Tofts modeling of concentration – time curves for the same mouse as in figure 4.13 are presented in figure 4.15. The curves have the same shape for day 0 and 1, before it changes at day 9. The initial increase in concentration is slower and wash out of the contrast agent is delayed.

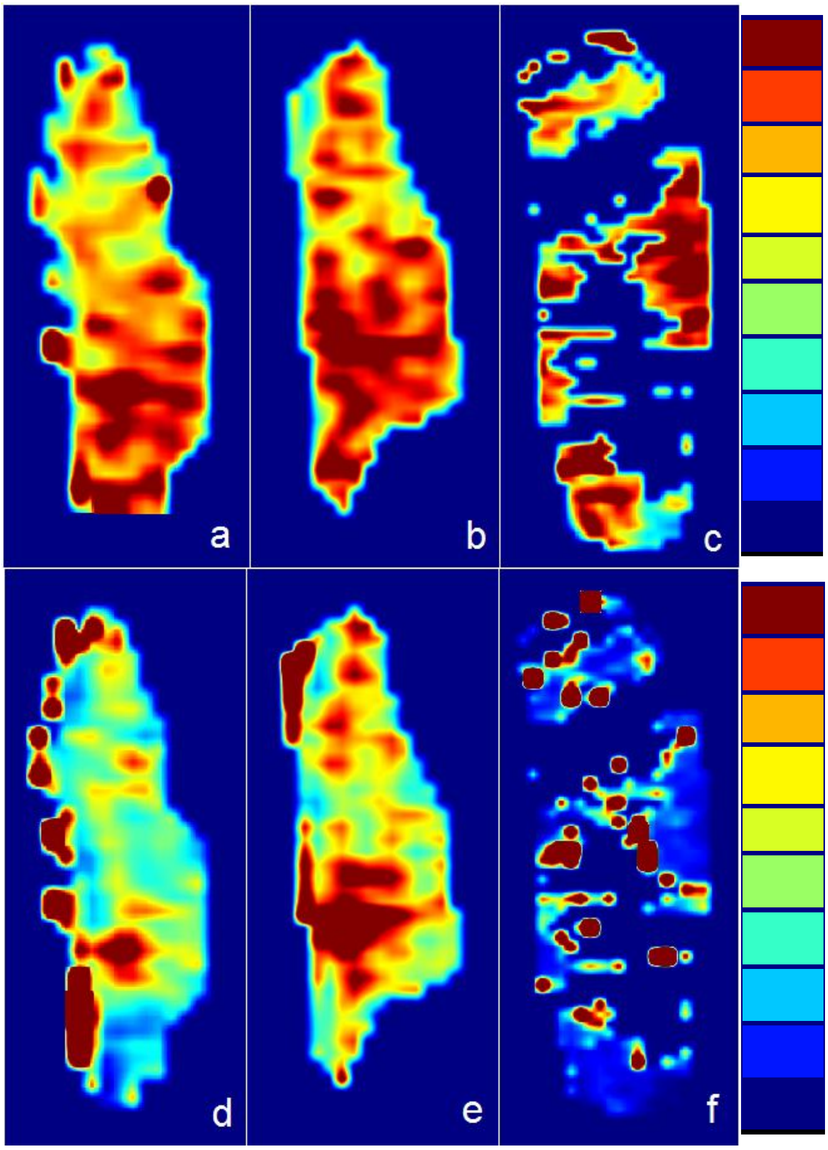

Figure 4.13 Parametrical maps for a mouse from the CWR22 control group. Panels a, b and c shows K^{trans} maps, panel d, e and f shows Ve for days 0, 1 and 9, respectively. Maximum K^{trans} values represented by dark red color were $0.256x10^{-3}s^{-1}$, $0.083x10^{-3}s^{-1}$ and $0.055x10^{-3}s^{-1}$ for panel a, b and c respectively. Minimum K^{trans} value was $0s^{-1}$ and represented by dark blue color. Maximum values for Ve represented by dark red color were 8.46, 0.24 and 38.06 for d, e and f panels, respectively, and minimum was 0 represented by dark blue color.

In figure 4.14, parametrical maps for a mouse from CWR22 irradiated groups are presented. On both K^{trans} and Ve maps a difference can already be observed 24 hours after irradiation, with a formation of an area with low contrast uptake on days 9. Mean K^{trans} values decreased from (0.019±0.001) $x10^{-3}s^{-1}$ to (0.009±0.001) $x10^{-3}s^{-1}$, followed by an increase to (0.024±0.001) $x10^{-3}s^{-1}$. The fraction of unfitted voxels increased from 7% before radiation treatment to 41% 24 hours after radiation, before a 8.6 % decrease on day 9.

Examining concentration-time curves (Figure 4.15) for the same mouse revealed changes in the curve shape already 24 hours after radiation treatment. Both the initial build-up of contrast agent concentration and the wash-out was slower compared with the pretreatment curve.

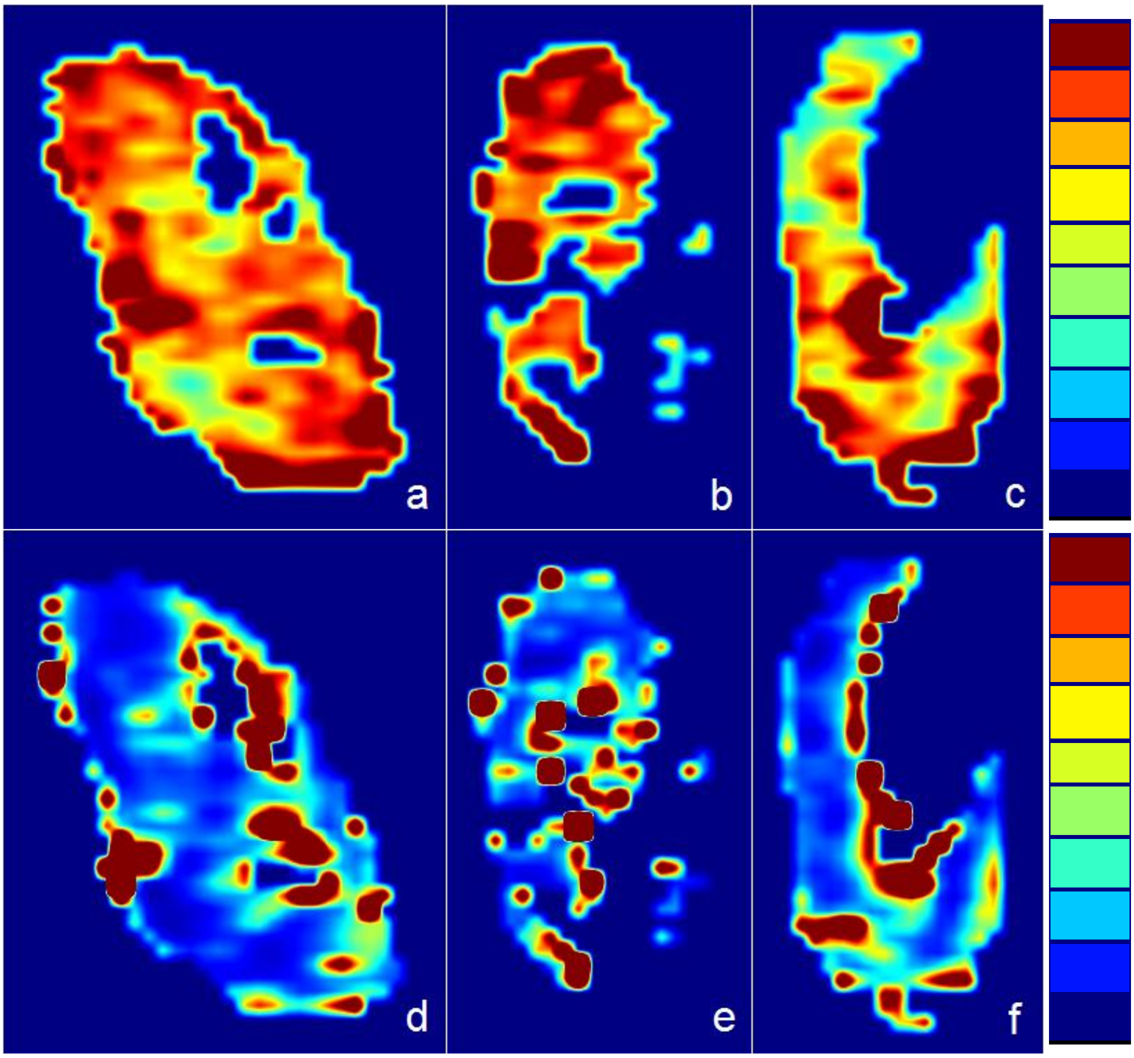

Figure 4.14 Parametrical maps for a mouse from CWR22 irradiated group. Panels a, b and c shows K^{trans} maps, panel d, e and f shows Ve for days 0, 1 and 9, respectively. Maximum K^{trans} values represented by dark red color were $0.052 \times 10^{-3} s^{-1}$, $0.041 \times 10^{-3} s^{-1}$ and $0.111 \times 10^{-3} s^{-1}$ for panel a, b and c respectively. Minimum K^{trans} value was $0 s^{-1}$ and represented by dark blue color. Maximum values for Ve represented by dark red color were 16.58, 20.44 and 5.69 for d, e and f panels, respectively, and minimum was 0 represented by dark blue color.

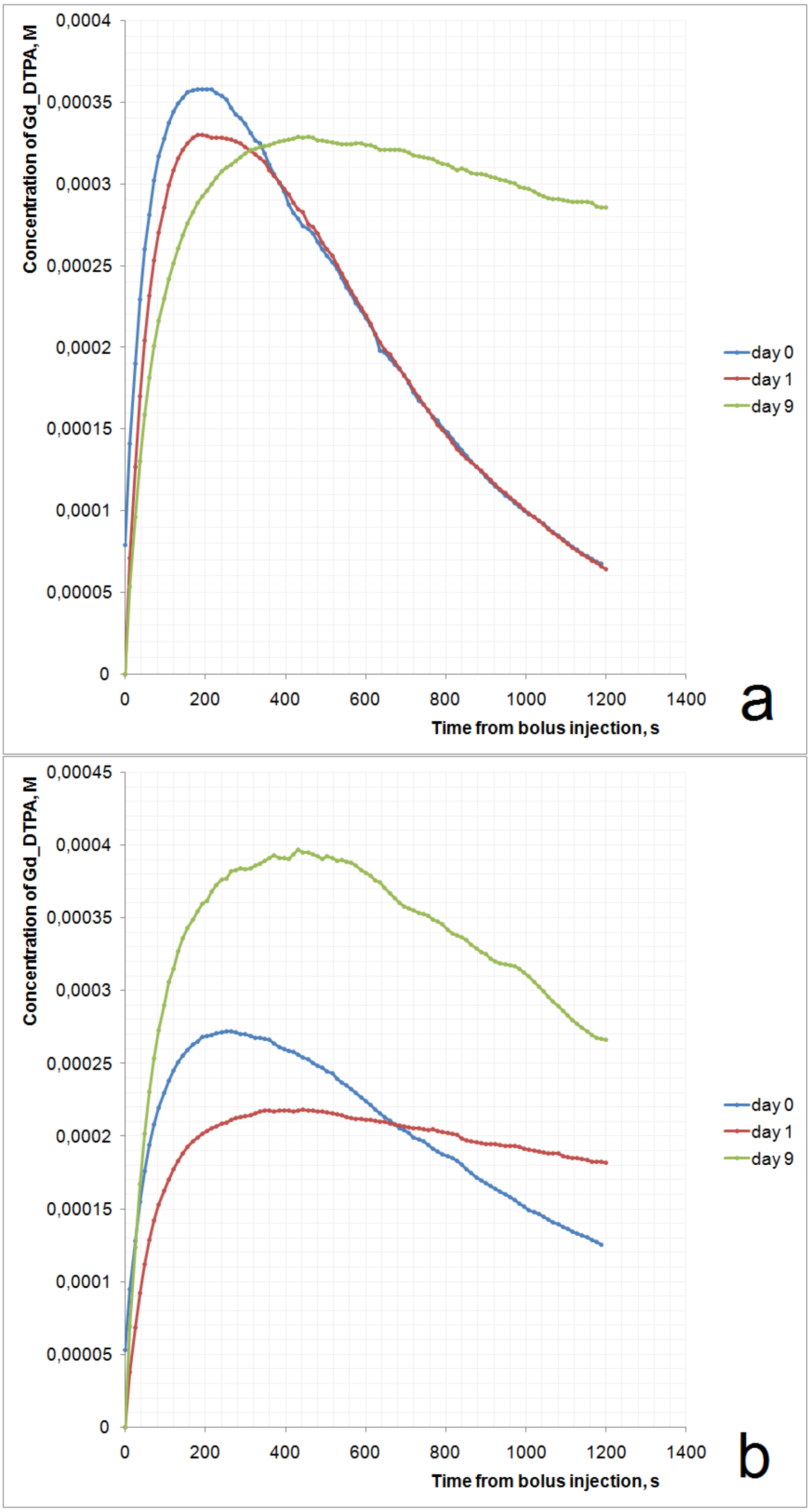

Figure 4.15Tofts modeling of the mean concentration of Gd-DTPA in the tumor’s central slice. Panel a represent the central slice of the tumor in mouse number 6 CWR22 control group, panels b – number 5 CWR22 irradiated group, days0, 1 and 9, respectively.

In Figure 4.16, parametrical maps of the central slice of a tumor from CWR22CA irradiated group are shown. The amount of unfitted voxels in the center of the tumor increased for 3 consecutive days. Mean K^{trans} values decreased from day 0 to day 9 (day 0: $0.0368x10^{-3}$ s^{-1}, day 1: $0.0293x10^{-3}$ s^{-1}, day 9: $0.0124x10^{-3}$ s^{-1}) while the fraction of unfitted voxels increased from 0.12% before irradiation to 16% 24 hours after, followed by a further increase to 66% at day 9. It was an increase in mean V_e from 0.04 at day 0 to 0.47 at day 1, followed by a decrease at day 9 to 0.05.

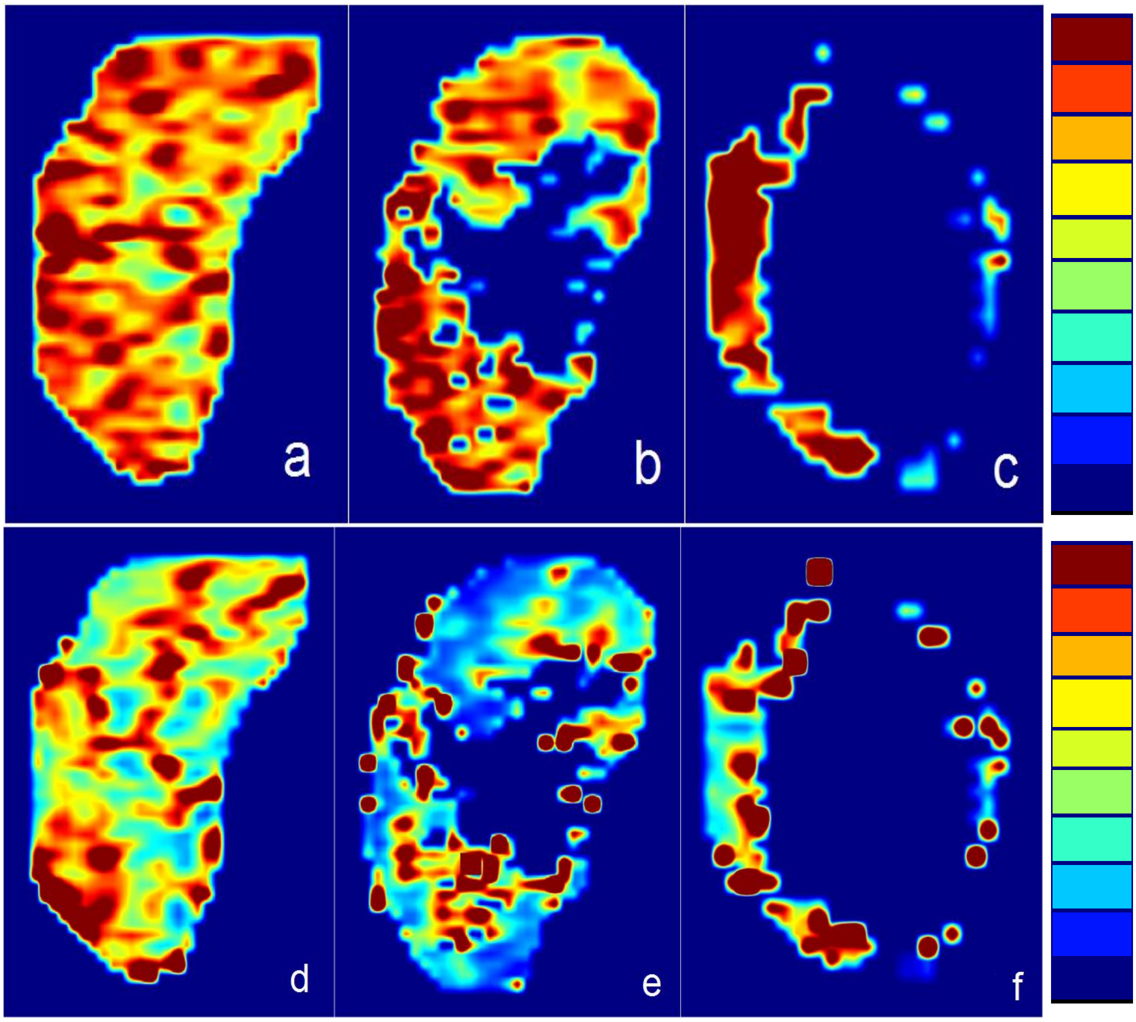

Figure 4.16 Parametrical maps for a mouse from CWR22CA irradiated group. Panels a, b and c shows K^{trans} maps, panel d, e and f shows Ve for days 0,1 and 9, respectively. (IR5) Maximum K^{trans} values represented by dark red color were $0.113x10^{-3}s^{-1}$, $0.144x10^{-3}s^{-1}$ and $0.146x10^{-3}s^{-1}$ for panel a, b and c respectively. Minimum K^{trans} value was $0s^{-1}$ and represented by dark blue color. Maximum values for Ve represented by dark red color were 0.23, 1.19 and 9.24 for d, e and f panels, respectively, and minimum was 0 represented by dark blue color.

The Tofts modeling of concentration – time curves for the same mouse are presented in Figure 4.17 along with concentration – time curves for a mouse from CWR22CA control group for comparison. There are no dramatic changes in curve shape as for tumors without androgen deprivation 24 hours after radiation treatment. Slightly delayed wash out can be observed. But 9 days after treatment a slower Gd-DTPA concentration increase and almost absence of wash-out of contrast agent during acquisition time can be seen when comparing with pre-treatment curve (Figure 4.17.b). In contrast no change is observed in the shape of the Gd-DTPA concentration curves for the control mouse (Figure 4.17.a).

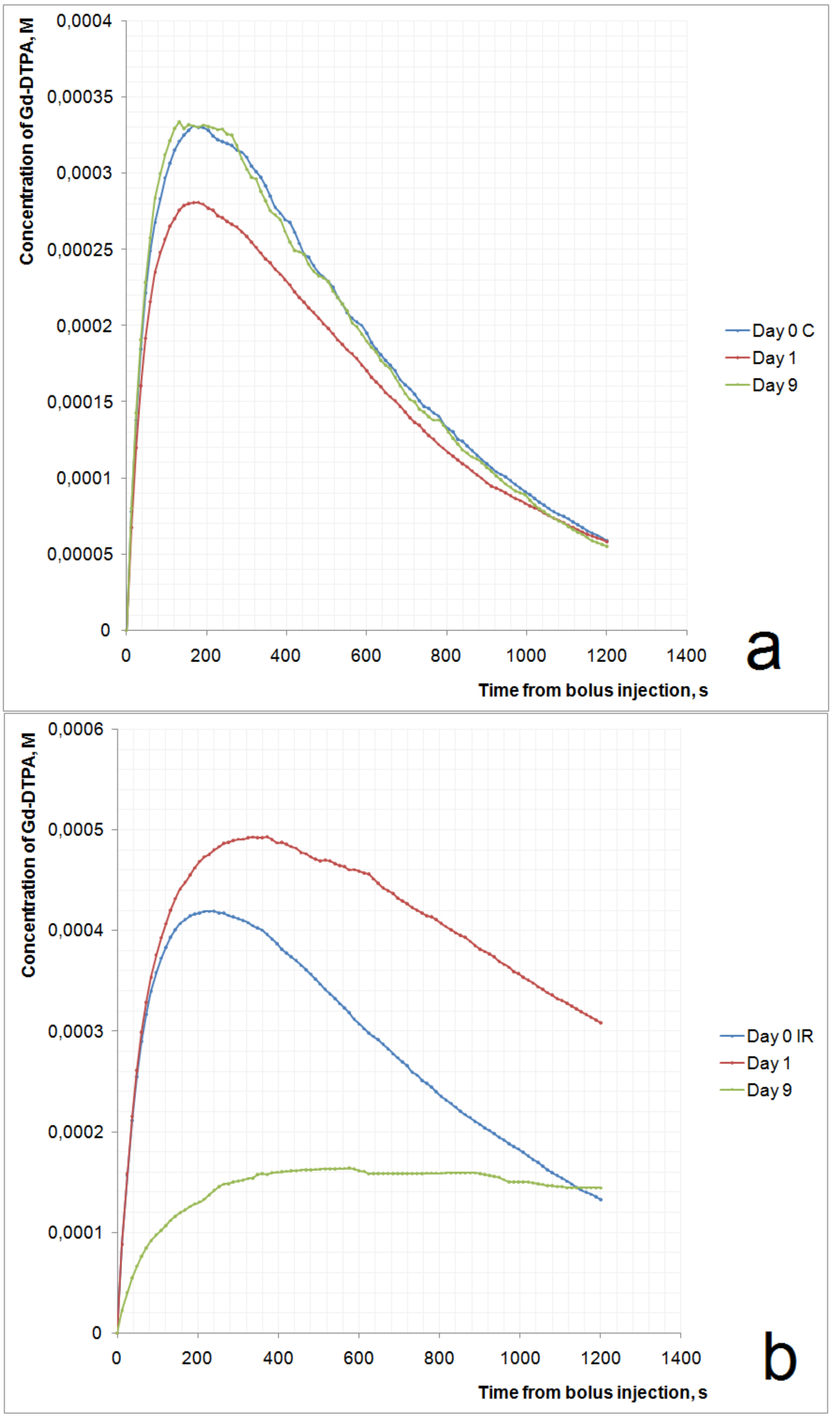

Figure 4.17 Tofts modeling of the mean concentration of Gd-DTPA in the tumor's central slice. Panel a represent central slice of tumor in mouse number 4 CWR22CA control group, panels b – number 4 CWR22CA irradiated group, days 0, 1 and 9, respectively.

4.5.2. Quantitative results of DCEMRI

Figure 4.18 shows mean K^{trans} values for all groups. On day 0 bars represent pre-treatment groups of 16 CWR22 tumors and 16 CWR22CA tumors. Post-radiation, these groups are divided into four bars representing 8 tumors each. Mean pretreatment K^{trans} value for the CWR22CA group was 49% higher than for the CWR22 group ($p < 0.01$). At day 1 and 9 the CWR22CA tumors showed no significant change in K^{trans} values post-irradiation or in control groups compared to pretreatment values. There was no significant difference between control and irradiated groups for CWR22CA tumors for all monitored days.

For irradiated CWR22 tumors a 47% decrease ($p=0.01$) in K^{trans} value was observed on day 1 compared to pre-treatment values, followed by a 110% increase from day 1 to day 9 ($p< 0.01$). Compared to CWR22 control tumors, CWR22 irradiated tumors had a smaller K^{trans} value at day 1 ($p=0.01$) and day 9 ($p=0.08$). CWR22 control tumors showed no significant changes in K^{trans} values compared to pretreatment value.

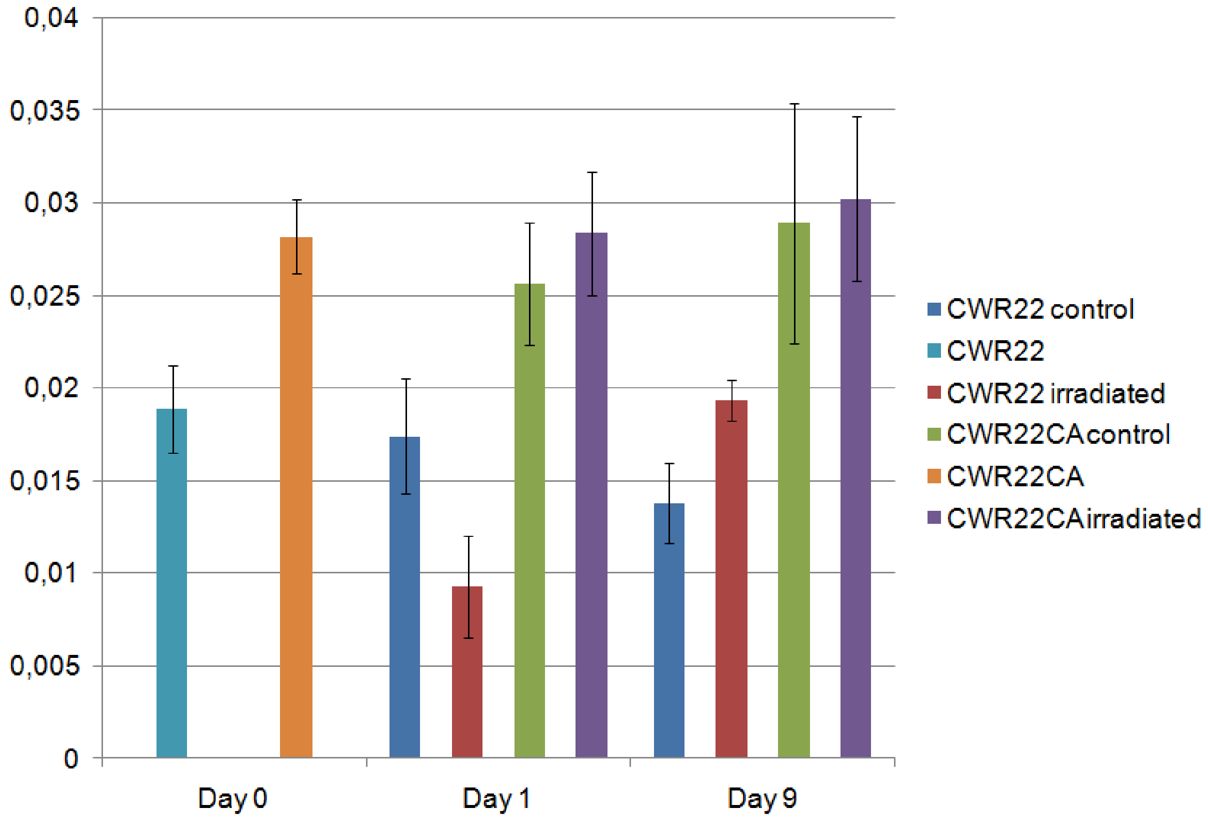

Figure 4.18 Mean ±SEM K^{trans} values (10^{-3} s^{-1}) for CWR22 and CWR22CA control and irradiated groups on the MRI assessment days 0, 1 and 9. On day 0 pre-treatment CWR22 and CWR22CA groups represent 16 tumors each. On the post-treatment days 1 and 9 only control and irradiated groups are representing 8 tumors each. The tumors in the irradiation groups received a single fraction of 15 Gy after the day 0 MRI, followed by post-treatment MRI at day 1 (24 h) and day 9.

In figure 4.19, mean Ve for all the groups are shown. For CWR22 irradiated group a 42% increase (p=0.03) was observed at day 9 compared to pretreatment values. No further significant differences were observed in control or irradiated groups compared to pretreatment values at day 1 and 9.

For CWR22CA control and irradiated groups showed no significant difference whether when comparing to pretreatment value or control to irradiated groups for the same day after treatment.

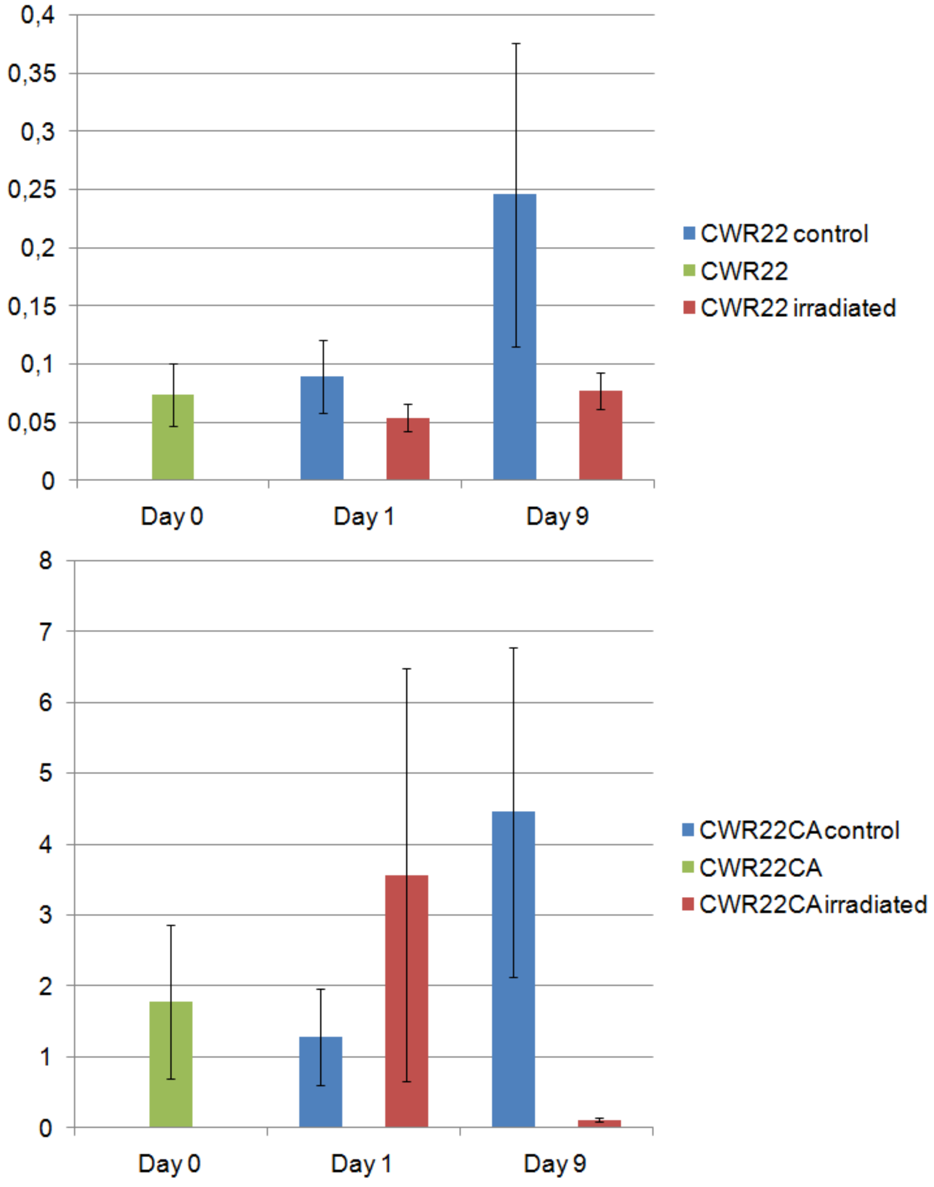

Figure 4.19 Mean ± SEM V_e for CWR22 and CWR22CA control and irradiated groups on the MRI assessment days 0, 1 and 9. On day 0 pre-treatment CWR22 and CWR22CA groups represented 16 tumors each. On the post-treatment days 1 and 9 control and radiation groups are represent 8 tumors each. The tumors in the irradiation groups received a single fraction of 15 Gy after the day 0 MRI, followed by post-treatment MRI at day 1 (24 h) and day 9.

No significant difference in fraction of unfitted voxels was observed for the CWR22 control group compared to pretreatment values. For the CWR22 irradiated group the fraction of unfitted voxels showed a 211% increase in the number of unfitted voxels (p=0.013) followed by a 57% decrease from day 1 to day 9 (p=0.032). No significant difference was observed for the CWR22CA control and irradiated groups compared to pretreatment values, between control and irradiated groups for the same day after treatment or comparing with respective fractions of unfitted voxels for CWR22 tumors.

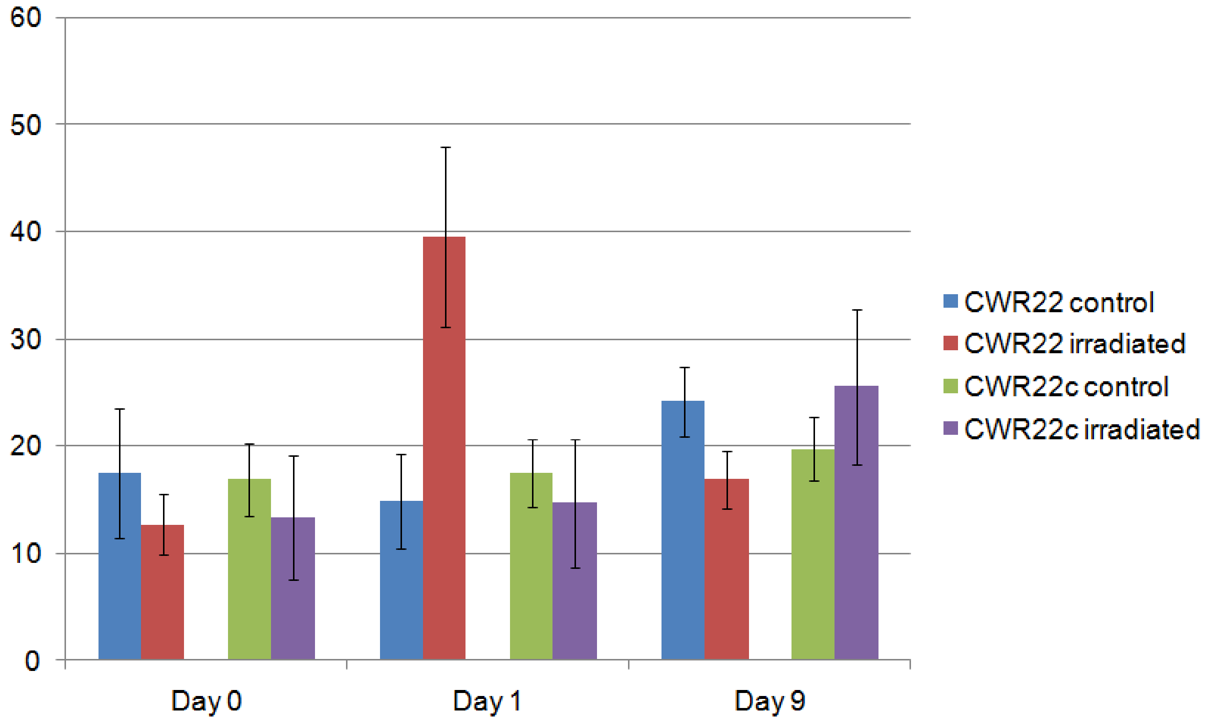

Figure 4.20 Fraction of unfitted voxels (percent) for CWR22 and CWR22CA control and irradiated groups on the MRI assessment days 0, 1 and 9. The tumors in the irradiation groups received a single fraction of 15 Gy after the day 0 MRI, followed by post-treatment MRI at day 1 (24 h) and day 9.

The decrease in K^{trans} from day 0 to day 1 for CWR22 irradiated tumors coincided with a 212% increase in the fraction of unfitted voxels, giving a significant negative correlation between K^{trans} and the fraction of unfitted voxels for this group ($r = -0.69$, $p < 0.01$). K^{trans} was also negatively correlated to the fraction of unfitted voxels ($r = -0.62$, $p < 0.01$) when values from all tumors at all time-points were included in the analyses (Figure 4.21).

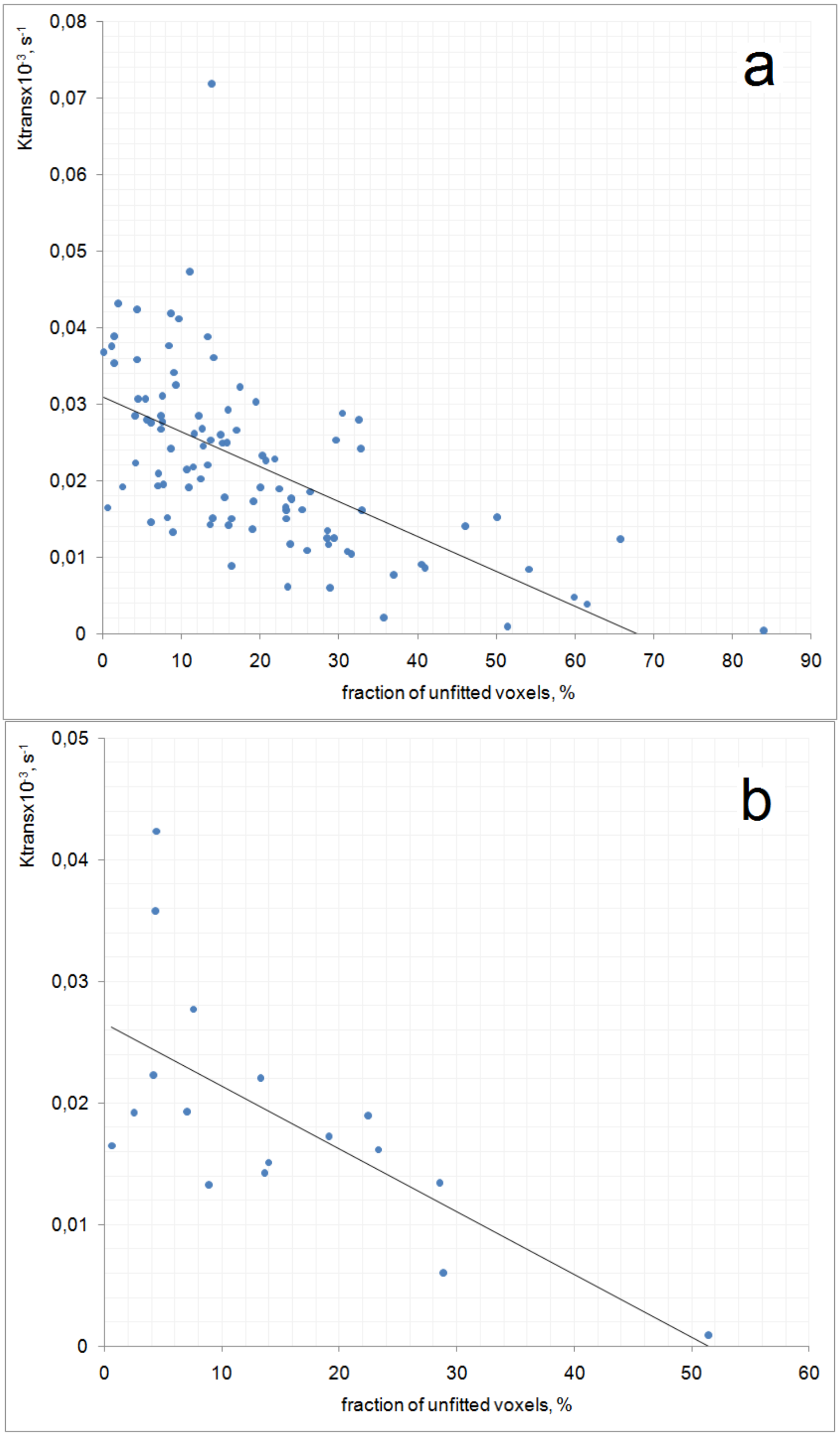

Figure 4.21 The correlation between the fraction of unfitted voxels (%) versus K^{trans} in the CWR22 model using all 4 treatment groups ($r = -0.616$, $p < 0.01$) (a). The correlation was stronger using only control tumors ($r = -0.686$, $p < 0.01$) (b).

4.6 DW-MRI results

Using a b- value of 300 s/m^2, theCWR22 irradiated group showed a 39% ($p<0.01$) and 63% ($p<0.01$) increase in ADC at day 9 compared to pretreatment value and value at day 1, respectively. For b=600 s/m^2 the increase was 35% ($p=0.05$) and 58% ($p<0.01$) (Figure 4.22). For both b-values at day 9 ADC for CWR22 irradiated group was 1.5-($p<0.01$) and 1.6-fold ($p<0.01$) higher than for CWR22 control group (b=300 s/m^2 and b=600 s/m^2 respectively).For b=300 s/m^2 at day 1 ADC for CWR22 control group was 1.2-fold higher ($p=0.02$) than for CWR22 irradiated group. There was no significant difference at b=600s/m^2.

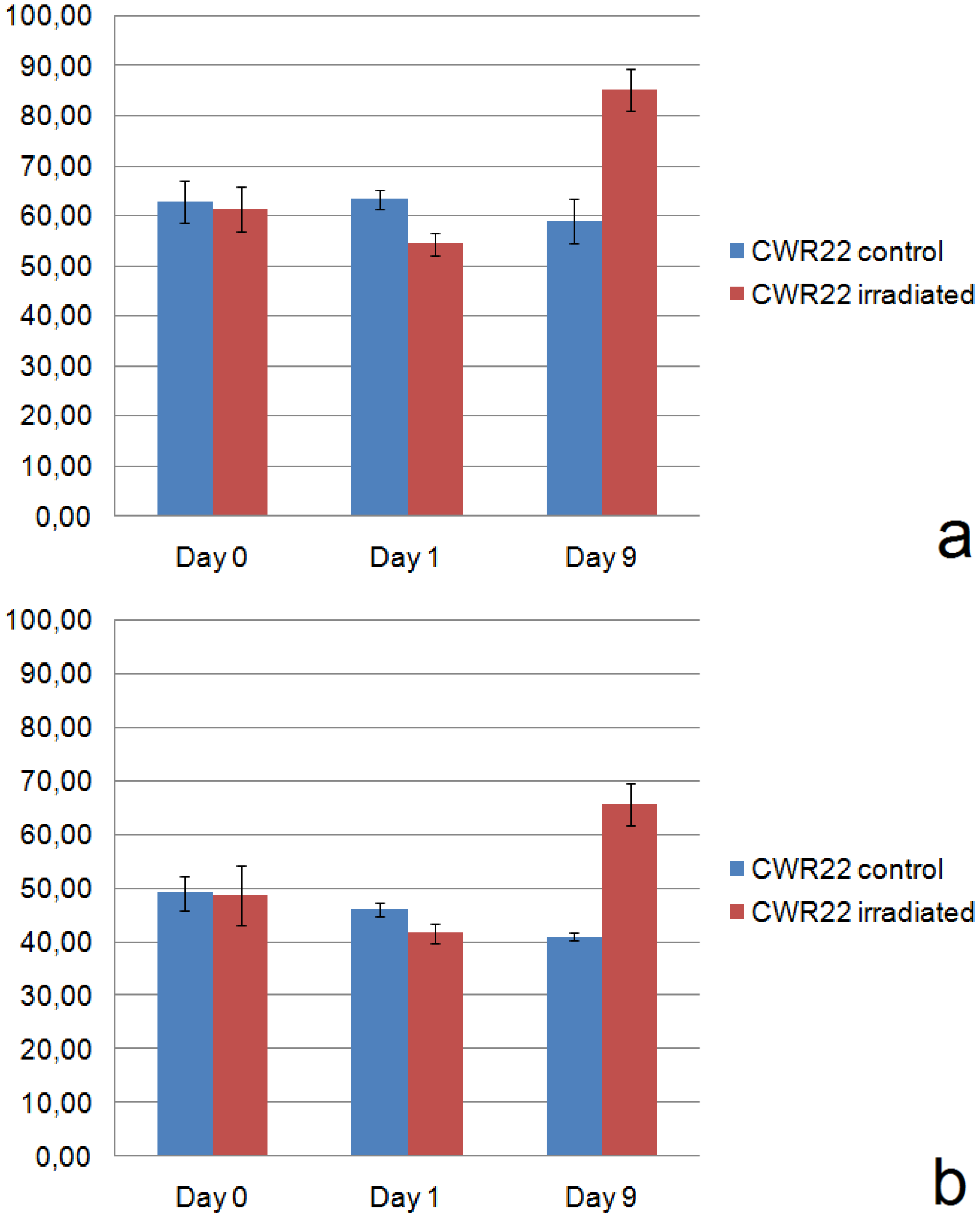

Figure 4.22 ADC values for CWR22 control and irradiated groups normalized to day 0, b values 300s/m^2 (a) and 600 s/m^2 (b)

No significant changes in ADC values for CWR22CA control and irradiated groups were observed (Figure 4.23). Compared with non-castrated mice ADC for CWR22CA irradiated group was 1.5 ($p=0.02$) and 1.6-fold ($p<0.01$) less than for CWR22 irradiated group at day 9 ($b=300$ s/m^2 and $b=600$ s/m^2, respectively).

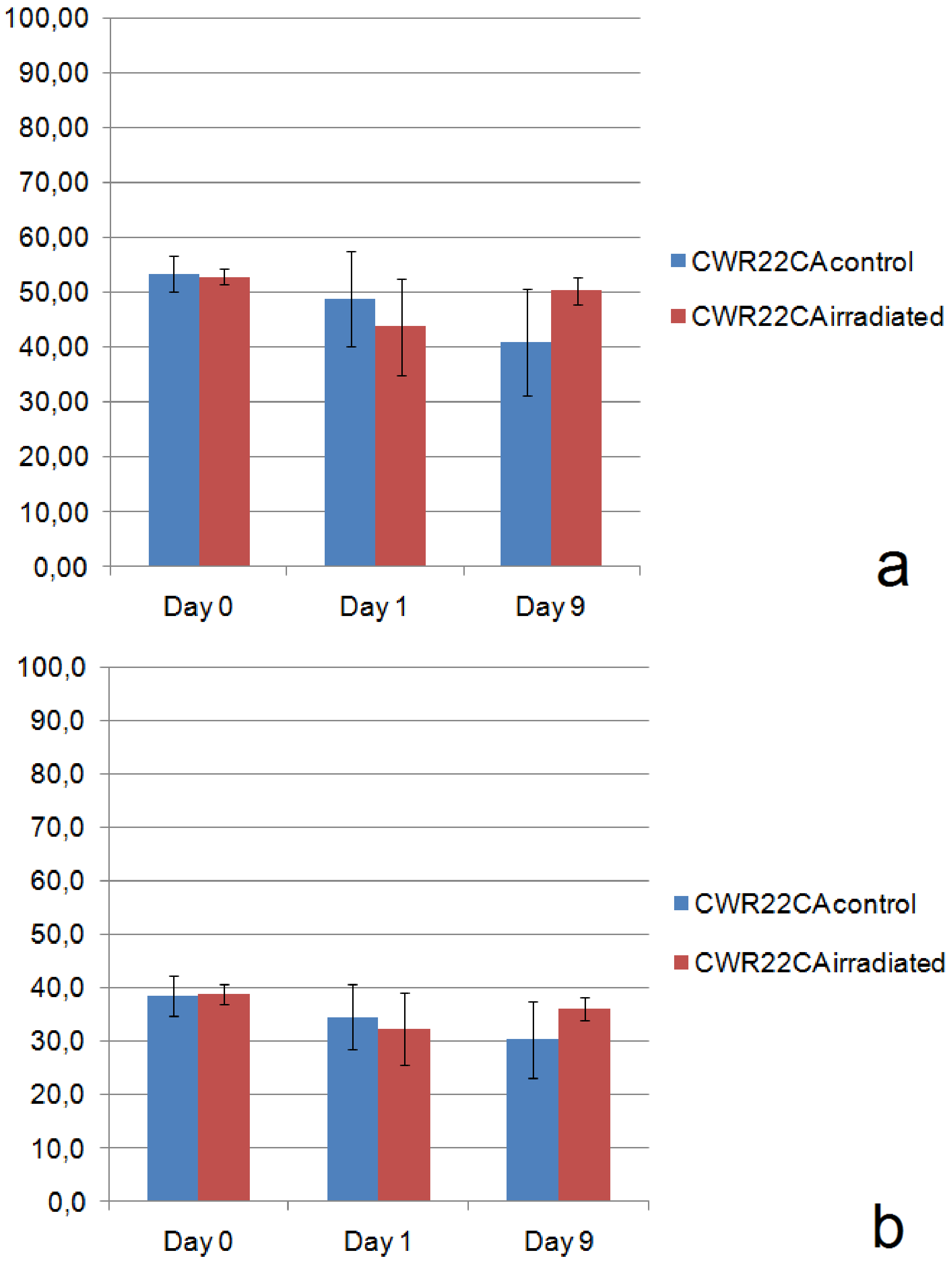

Figure 4.23 ADC values for CWR22CA control and irradiated groups normalized to day 0, b values 300 s/m^2 (a) and 600 s/m^2 (b)

There were no significant correlations for ADC values with total PSA concentration, tumor volume or ratio of unfitted voxels.

Chapter 5

Discussion

The goal of this project was to study the difference between prostate cancer CWR22 xenografts with normal androgen supply and undergoing androgen deprivation treatment in immunedeficient mice by applying noninvasive visualization methods, like DCE-MRI and DW-MRI. The specific aim was to determine if tumor vasculature represented by K^{trans}, fraction of EES represented by Ve and tissue structure represented by ADC in prostate cancer xenografts with full androgen supply will change following androgen deprivation, and if it will affect the radiation response. It was investigated whether the functional MRI methods gave more information about treatment response than classical clinical marker for prostate cancer, like PSA and tumor volume.

5.1. Experimental Animals

As other experimental models, subcutaneous xenografts in nude mice have their benefits and limitations. Xenografts derived directly from patient biopsies largely retain the morphological and molecular properties of the source tumors, and preserve the metabolic and growth patterns. But to be a sufficient model for research purposes it has to satisfy more demands. The tumor has to grow fast, linear or exponential with time, and have low necrotic fraction even with big volumes. The most important characteristics of xenografts for clinical experiments are relevance and opportunity to transfer results from animal to human.

The CWR22 xenograft model is a prostate cancer model that satisfies most of the above discussed limitations. After it was established, it became a popular human xenograft for research groups working within prostate cancer. The reason for this is that it retains androgen dependency, regress when androgen treatment is used and relapses after a period of 3 to 10 months (Nagabhushan et al 1996). Taking into account that the mice metabolism is 5 times faster than in humans (Hall and Giaccia 2006), it has a good correlation with relapse time point in patients, which is 2-5 years after androgen deprivation (Bruchovsky et al 1990, Trachtenberg 1987) The disadvantages of the CWR22 xenograft are uneven growth rate in different mice, even with equal testosterone levels, and a large necrotic fraction in large tumors, which is required for MRI of xenografts when using a clinical 1.5 T scanner.

One of the challenges that influenced this work was the androgen-deprivation treatment. The treatment procedure was carried out by surgical castration. As it is impossible to provide personal care for each mouse after the surgery, 9 mice were lost due to prolapsed intestine. It also appeared that xenografts have to have a certain size to response to androgen deprivation. When xenografts were larger than 16 mm in largest diameter, they failed to regress and additionally 10 mice had to be sacrificed due to exceeding the upper limit for the size of the tumor. Androgen deprivation therapy also prolongs the time in the experiment for each mouse, which increase the probability for infections or physical damages that can lead to animal sacrifice. This led to the loss of 12 mice. At last, it should be noted that castration changes the metabolism of animals, making them weaker. In combination with radiation treatment it resulted in additionally 4 deaths.

During MR experiments the mice were anesthetized. When sleeping, the mice blood pressure and body temperature decreases. To maintain body temperature a heating system ensured equal conditions for all mice in the MRI experiment.

5.2. The xenograft

One of the standard instruments for tumor measurement is a slide caliper. CWR22 xenografts are soft, and the thick skin of male mice compared to female, can reduce the accuracy of tumor volume measurement. In androgen-deprived mice, precise estimation of tumor volume can suffer from additional edema forming around the tumor due to the treatment. This leads to fluctuation in measurements for the same tumor. A large biological variation forces the use of more animals in each experiments group to obtain the necessary statistics in measured parameters, not only for tumor volume but also for other parameters. The large fraction of mice which died after androgen-deprivation treatment dramatically increased the number of animals involved in the experiment.

Due to uneven growth and regress rate the process of randomization of mice into groups was complicated. One of the factors causing uneven take time and growth rate is heterogeneity in tissue samples obtained for inoculation. As it was said above, CWR22 xenografts have a significant necrotic fraction. But in contrast to other xenografts that primary have a necrotic core in the center on the tumor, CWR22 xenografts have necrotic areas distributed all over the volume. This leads to heterogeneity in shape and quality of the implantation material. One of the solutions can be to inoculate xenografts in form of cell suspensions in a growth media, like Matrigel(tm). Another factor that can reduce heterogeneity in growth rate is to insert a time-release testosterone pellet at the time of tumor implantation to ensure constant testosterone levels during tumor growth, and then remove the pellet at the time of surgical castration. Implantation of testosterone pellets suppresses testosterone production by testicles and adrenals (Harkness et al 1975). This will lead to more even distribution of hormone levels between mice used in experiment. But as practice at our institute shows this do not have any significant benefits so far.

Heterogeneity of the tumor and uneven distribution of necrotic areas can also compromise slice selection in MRI. As the tumor is implanted subcutaneously, the tumor can rotate and change slice position between acquisition days. This can lead to selection of different slices used for analysis with different tissue distribution and complicate data comparison between days. This problem will be discussed together with discussion of the MRI analysis.

Mice were included into the experiment when tumor size reached 8 mm at the smallest diameter. Because tumors not grew evenly, the mice were included one by one or in small groups. Despite this, statistical analysis showed that tumor volumes were normally distributed and there was no significant difference between groups. For the CWR22CA group, with time from inoculation to castration being 25 to 56 days, inclusion was also complicated by uneven regress rate (time from castration until first MRI acquisition was 14 to 54 days). The total time from inoculation until the end of experiment varied from 84 to 125 days, with mean time for control group of 93±3 days and 106±5 days for the irradiated group.

Tumors used in the experiment were growing subcutaneously (s.c.), not orthotopic. Despite subcutaneous xenografts being a well established model, the use of an orthotopic model can be more preferable, especially in gene expression experiments, where microenvironment is important. However, it will not allow measurement of tumor volume by slide caliper. It is still possible to measure the size of orthotopic tumors using a three-dimensional ultrasound micro-imaging technique (Kraaij et al 2002), but this technique was not available in this experiment. This fact and unclear benefits from using an orthotopic model for the experiment resulted in the choice of a non-orthotopic s.c. CWR22 xenograft.

5.3 Histology

On histological sections from CWR22 irradiated tumors acellular regions of various shape and size was seen. It is difficult to determine visually whether the empty spaces on the sections are of apoptotic genesis or if it is blood vessels. An experienced pathologist suggested that absence of blood and endothelial cells, ticked edge and high density could support an apoptotic nature of these cavities. On sections from CWR22 control tumors some acellular regions are also present. However, they are smaller, and the edge is smooth and have a round or oval shape. To exclude the possibility that it could be blood vessels an immunostaining using CD31 and anti-VEGF antibodies should have been performed.

Tumors in the CWR22CA irradiated group showed larger decreases in tumor volume as a result of radiation treatment compared to the CWR22 control group, but the difference was not significant. On the histological sections obtained from tumors at day 30, the apoptotic acellular regions can be seen, while control tumors had compact packed cells without spaces. The pattern is similar to the one in CWR22 irradiated group tumors without androgen-deprivation. But as only few samples were collected for the histology, no conclusion about significance of this finding can be made.

5.4. PSA

Total PSA concentration for the CWR22 control group increased with time on all consecutive measurement days, while there was no significant difference in PSA concentration normalized to tumor volume. This can be a result of constant leakage rate and the fraction of viable tissue in a tumor. It was found a strong linear correlation between total PSA concentration and tumor volume. This is consistent with earlier finding by other groups (Wainstein et al 1994). When data from mice with only untreated tumors was used in statistical analysis, the correlation was stronger. This suggests that the result of androgen deprivation or radiation on PSA and tumor volume appears on different time-points following treatment. have different timing.

Radiation or androgen–deprivation treatment changes membrane permeability or even cell death that can affect leakage of PSA from cancer cells. Following radiation treatment, the PSA concentration increased 60% 24 hours after the procedure, but statistical analysis showed only close to significance level with p=0.06. There was no significant difference compared to the control group. This can be explained by biological variation between individual mice as a result of treatment. At day 9, a plateau can be observed, corresponding to the same plateau showed by Dyke and colleagues (Dyke et al 2003) after a single radiation dose of 20 Gy. However, on their first measurement 6 days after treatment, when plateauing started, no significant difference from the control group was found. Only 11 days after treatment a significant difference between control and irradiated groups was achieved. In our experiment the first significant difference between control and irradiated groups appeared 9 days after irradiation. The low time-resolution is one of the major drawbacks of PSA as a marker for early treatment response since it takes time before the cells stop in the G1/G0-phase and they only proceed to apoptotic death when they fail to repair damages before the mitosis (Agus et al 1999). As it will be discussed later, $\mathrm{K}^{\mathrm{trans}}$ values obtained from MRI examinations, showed response to treatment already 24 hours after treatment, thus K^{trans} potentially can be used as an early marker of treatment response.

Comparing radiation treatment response with response to androgen deprivation therapy, some common features could be found. Earlier it has been shown that PSA has a half-life time of 3 to 8 days following mice castration and that PSA increased 3-fold 24 hours after treatment (Nagabhushan et al 1996). It was shown that initially the cells proceed to G1/G0 arrest instead of apoptotic death (Agus et al 1999). At the inclusion of animals into our experiment, the mean concentration of total PSA for the CWR22 groups was almost 2-fold higher than for CWR22CA groups that received androgen-deprivation therapy. Measurement of PSA concentration for the CWR22CA group was performed 14 to 54 (mean 32) days after androgen deprivation. This gives enough time for reduction of not only PSA concentration, but also slowing the metabolism of the cells as a result of PSA production. At the last day of the experiment (39 to 84 days, mean 63 days after castration) total PSA concentration was reduced to 5.29 ng/ml and 0.88 ng/ml for control and irradiated groups, respectively, which gives a 6-fold difference between the groups ($p<0.01$). It can be hypothesized that even it was no significant difference in tumor volume between the groups at the end of experiment, PSA concentration shows that combined androgen-deprivation and radiation therapy was more favorable than androgen-deprivation or radiation alone. As it was no MRI acquisition at this day, there is no data about physiological condition of the tumor to correlate with or support the hypothesis. Mean regrowth time for androgen-deprived tumors is 3 to 10 month. It can be suggested that this time will be longer for tumors that had a combination therapy. As the experiment was time-limited it was not possible to prove this hypothesis in practice for this experiment. However, by coincidence 4 mice that not was used in this experiment, but received the same treatment as CWR22CA irradiated group, showed no relapse 1 year after irradiation.

Free PSA concentration is not a diagnostic parameter itself, but a low proportion of free PSA is associated with increased probability of finding prostate cancer by biopsy in humans. The proportion of free PSA was lower for the CWR22 groups compared to the CWR22CA groups, but the difference was not significant. It has been reported that in humans, free PSA has a half-life time of 110 minutes and therefore can be used as an early marker for treatment response, but no clinical recommendations or reference values have been established (Richordson et al 1996). Analyzing mean free PSA concentration values gave no significant difference in response to radiation or androgen deprivation compared to total PSA.

5.5. Radiation

A single dose of radiation therapy was chosen for this experiment. A total dose of 15 Gy was delivered in approximately 22 minutes. A high dose rate results in acute cell damage. Previously it has been reported metabolic changes in CWR22 tumors following a 20 Gy single dose x-rays radiation treatment (Dyke et al 2003). The dose distribution in the tumor volume should be equal. To compensate for the initial build-up of radiation deposition from the Co-60 source, a 5 mm thick bolus was used.

In experiment design, single-dose radiation treatment has its advantages. The dose-rate effect can be neglected, considering that delivery time is smaller than time needed for reparation and less than the cell cycle time, thus the radiation damage can be considered acute. As the CWR22 xenograft could be hypoxic, single dose radiation could allow maintaining a large fraction of cells due to its radioresistance. Following later reoxygenation a larger fraction of viable cells will be available and then the relapse will occur earlier than in fractionated radiation treatment. When using a fractionated treatment, multiple anesthesia on consecutive days will be needed, which could have increased the mortality of mice during the treatment procedure.

5.6. MRI in cancer

Development of new anti-cancer therapies requires optimization of existing treatment modalities and protocols to understand the regulation processes, therapy results and post-therapeutic processes in individual tumors. A group of methods based on NMR are now being applied to both cell and animal models to assess tumor physiology and metabolism, which later can be available in clinical practice. Among other methods, MR spectroscopy, diffusion-weighted MRI and contrast-enhanced MRI non-invasively provide information regarding tumor metabolism and pathophysiology.

5.6.1 Dynamic contrast enhanced MRI.

Introduction

As any experimental method DCE MRI has its advantages and limitations. DCE MRI is a non-invasive and quantitative method that can be used in investigation of microvascular structure; it do not involve ionizing radiation and gives good spatial resolution. It also provides functional analysis by tracking the pharmacokinetics of injected low-molecular weight contrast agents as they pass through the tumor vasculature. It is sensitive to alterations in vascular permeability, extracellular extravascular and vascular volumes and in blood flow. One of the main apparatus advantages is that it can be performed on standard 1.5 Tesla clinical scanners. The popularity of DCE-MRI increases due to the fact that data obtained in the experiments can have direct clinical use. (O’Connor et al 2007) A correlation between tissue MRI enhancement and immuno-histochemical microvessel density has been showed in many studies (Padhani 2003).

Analysis

Different methods can be applied to analyze DCE-MRI data. Signal intensity enhancement on T_1-weighted DCE-MRI images can be assessed in several ways, both qualitatively and quantitatively. Qualitative parameters of signal intensity-time such as shape, time to maximum enhancement or increase coefficient can be used for characterization of tissue and response to treatment. One of the disadvantages of this analysis is variation between acquisitions and individual examinations, making a direct comparison between animals or experiments difficult. Model free parameters describe tissue enhancement using descriptors such as initial and mean gradient of the rise of enhancement curves, maximum signal intensity, washout gradient and the area under gadolinium contrast concentration (AUGC). Such values have the advantage of being easy to calculate and can be used when quantitative techniques fail. Limitations are that they do not accurately reflect the contrast medium concentration in tissues and do not directly rely to tissue physiology (Alonzi et al 2007).

Converting the signal intensity into contrast agent concentration allows determination of parameters that are more physiologically related and independent of the way they were obtained. The relationship between signal intensity and contrast agent concentration is not linear (Tofts et al, 1999). It was showed by Hittmair and colleagues (Hittmair et al 1994) that a given contrast uptake causes an increase of relaxativity, which is independent of tissue or sequence parameters. However, signal intensity increase depends on native T1 relaxation time and native signal intensity, or in other words that the same uptake of contrast agent causes a higher increase of signal intensity in native hypointence tissues than in native hyperintence tissues. To determine the proportionality constant two water based phantoms, one with pure water, and one with water doped with Gd-DTPA of known concentration was used. As relative signal intensity increase depends on sequence parameters, like flip angle and TR, it complicates comparison between results with different sequence parameters. Hittmair and colleagues (Hittmair et al 1994) suggested that under steady-state conditions with perfect spoiling of transverse magnetization and echo time much less than T2* relaxation time, the signal intensity is exponentially dependent of the T1 relaxativity. Using a parameter called enhancement factor, a differential T1 relaxation rate can be obtained from native and post-contrast images. The enhancement factor is linear with contrast uptake and independent of other tissue and sequence parameters.

To determine physiological characteristics such as flow and capillary endothelial permeability from contrast agent concentration data different pharmacokinetic models can be applied. The most common model parameters that are being used, like K^{trans} and Ve, are independent of acquisition protocol and do only reflect tissue characteristics. The advantage of these parameters is their universality. They are independent of image acquisition protocols and equipments (O’Connor et al 2007, Leach et al, 2005). Another related parameter such as the rate constant Kep, which describes the ratio of K^{trans}/Ve, was not presented in the results of this work as it do not carry additional physiological information. The Tofts and Kermode model was used to fit concentration-time curves. There are several models that can be applied to DCE-MRI data to enable calculation of K^{trans} and Ve, but many of them are similar to the Toft model (Larsson et al, 1990; Tofts and Kermode, 1991). These models make different assumptions. The Larson et al. model in a simple approach assumes that signal intensity is linearly related to contrast agent concentration and concentration increase is not flow limited.

As a result only the ratio of K^{trans}/Ve can be found. The Brix et al model have a practical limitation demanding a long injection time, up to 4 minutes (Tofts 1997). The Tofts and Kermode model (Tofts and Kermode 1991) utilizes a bolus injection, a theoretical expression that only has concentration of contrast agent in tissue as an unknown, and fits well to gradient echo data from both human tumors and transplanted tumors (Tofts 1997). As a result, independent K^{trans} and Ve parameters can be found. However, the use of K^{trans} as a measure of vascularization also assumes that blood flow is not limited and that flow is always greater than permeability (Tofts et al 1999/10). The Tofts and Kermode model assumes that the tissue blood volume negligibly contributes to the signal compared with that arising from the contrast agent in the interstitial space, and that the blood concentration of contrast agent is described by a time varying AIF. As a result, analyzes must be carried out carefully with special interpretation of data from large tumors with big necrotic areas or irradiated tumors. Using K^{trans} values from unfitted voxels that had a zero value takes this into account and results in reduced K^{trans}. The model also assumes that contrast agent is mixed with plasma right after injection. In the experiment this assumption is reasonable as the blood circulation time in mice is short relative to the injection time. Taking into account the assumptions made by the model and for measurement of contrast agent concentration, quantitative kinetic parameters such as K^{trans} and V_e do allow comparisons between and within cohorts and different imaging centers (Tofts 1997)

CWR22 tumors showed a 47% decrease in K^{trans} 24 hours after a single radiation dose of 15 Gy. The specific contribution of radiation-influenced changes in flow, endothelial permeability and endothelial surface cannot be identified only from K^{trans} measurements. When irradiated, permeability of tumor capillary increases. Thus, K^{trans} becomes more flow dependent. A synergistic effect of perfusion, permeability and surface area on K^{trans} changes can be suggested. After irradiation, permeability of capillary membrane increased and a threshold was reached. No increase in Ve was seen for this group, suggesting that it is unlikely that the increase in permeability had a significant effect at this stage. K^{trans} can be considered perfusion-dependent. As a result of blood vessel damage or constriction of the capillary net, the endothelial surface cross-section is reduced. Decreased perfusion can be related to increased hypoxia and impaired nutrient supply. As it will be discussed later, an increase in the proportion of unfitted voxels 24 hours after treatment corresponds to decreased perfusion and formation of areas with acute hypoxia. The K^{trans} values in the unfitted voxels were set to 0 and used in calculation of means, which can explain the decreased K^{trans} values at day 1. As both Ve and tumor volume increased from day 1 to day 9, a formation of edema as a result of hypoxia and radiation damage can be suggested. As K^{trans} showed a 2-fold increase at day 9 compared to day 1 we can say that this increase could be explained by a combination of permeability and perfusion.

CWR22CA tumors in castrated animals had 49 % higher mean K^{trans} than CWR22 tumors in non-castrated animals. CWR22CA tumors were included in the experiment 32 ± 3 days after castration of the animals. It has been reported earlier that 2 weeks after androgen withdrawal for androgen-dependent Shionogi tumor an increase in VEGF, possibly due to hypoxia (Jain et al 1998), leads to renewed blood vessel growth. It is not clear whether this result can be extrapolated to the CWR22 tumor to explain the increased K^{trans} values by increased vascularization. However, increased perfusion combined with increased permeability can explain these elevated K^{trans} values (Nicholson and Theodorescu 2004).. No significant changes in K^{trans} or Ve, as well as tumor volume or PSA, were observed in

CWR22CA tumors after radiation treatment. From previous studies it has been reported that androgen-deprived tumors are hypoxic, thus the absence of response can be explained by a hypoxic start of androgen-deprived CWR22CA tumors. It is known that hypoxic cells are more radioresistant due to absence of oxygen. Oxygen is “fixing” DNA radiation damages by interacting with DNA radicals and forming non-restorable damages that can lead to cell death. In absence of oxygen, cells are able to repair the damage and increase survival. It has been proposed that androgen deprivation induces acute hypoxia (Rothermurd et al 2005, Goonewardene et al 2002). Considering that tumor volume continues to regress due to cell death and that androgen withdrawal happened 32 days before the first MR acquisition, a chronic hypoxic state can be suggested. This controverts with earlier statements about increased vascularisation of CWR22CA tumors. The most reasonable explanation for radioresistant behavior of these tumors, supported by work of Agus and colleagues (Agus et al 1999), is that most of the cells are in G0/G1 arrest. In the clinic, this lack of response to radiation treatment is observed in patients with prostate cancer following androgen-deprivation therapy when an androgen-independent phenotype develops. The presence of hypoxia has been suggested to be an important factor in prostate cancer progression by protecting against tumor cell destruction (Marignol et al 2008). However, in the same work of Agus and colleagues it was shown that androgen-independent proliferation start 80 to 400 days after androgen withdrawal. The latest inclusion of the tumor into our experiment was 54 days after androgen deprivation and formation of the androgen-independent phenotype cannot be an explanation. Anyway, further investigations should be made, including verification of the radiation resistance of CWR22CA tumors after relapse.

As significances were quite large and tumors in the same cohort were heterogeneous, the changes in K^{trans} may also represent different physiological processes in different individuals. Some tumors showed elevation and reduction in K^{trans} on day 1, with a shift to reduction and elevation respectively at day 9. These changes in K^{trans} could be a result of blood flow or permeability changes alone or a combination of both. Therefore, additional information is needed to correctly analyze DCE-MRI data, e.g. immunohistochemistry. A necrotic and hypoxic fraction and vascularization along with K^{trans} should be measured in order to understand the physiological mechanisms of this process. Unfortunately, this method will claim to sacrifice more animals at different time points to collect samples. As one of the principles of animal experiments is reduction of number of animals, it was not considered possible to do this in our experiment due to ethical and unclear benefits.

Data analysis was performed on a defined region of interest that included all parts of the tumor. A highly enhanced strip between the skin and the tumor caused by edema or containing main blood vessels supplying the tumor and connective tissue was not included into measurement. Tofts and Kermode modeling was used to approximate experimental data in each voxel, fitting experimental concentration-time curve to a mathematical model to obtain K^{trans} and Ve. Not every such experimental curve could be approximated correctly and they resulted in fit failures. When so, K^{trans} and Ve values for these voxels were set to 0 and included in calculation of mean tumor K^{trans} and Ve Previously it has been shown that the fraction of fit failures is strongly correlated to tumor necrosis (Bradley et al 2007). They showed that when excluding fit failures set to zero in calculation of mean tumor K^{trans}, no correlation with tumor necrosis was found, but represents the K^{trans} values in perfused viable tissue. Both Bradley and colleagues (Bradley et al 2007) and Galbraith and colleagues (Galbraith et al 2003) proposed that the post-therapy non-enhanced voxels can represent areas of tumor necrosis, supporting the inclusion of these voxels in mean K^{trans} calculation. In our experiment K^{trans} values were negatively correlated to the fraction of unfitted voxels, which can be attributed to treatment-induced increases in necrosis or tumor size-dependent increases in necrosis for untreated tumors.

Imaging protocol

Some models allow quantification of parameters such as flow, extraction fraction, Ve and mean capillary transit time (St Lawrence and Lee 1998). In the St. Lawrence and Lee model it is possible to separate perfusion and the permeability surface area product (PS). Recent experiments have showed that a temporal resolution of 1s is required to model the mean transit time accurately (Jayson et al, 2005; Parker and Buckley, 2005). In our experiment, acquisitions were made using a clinical scanner with a FSPGR sequence. The best time resolution with sufficient spatial resolution was 12 s. Choice of sequence for optimal image acquisition is always a trade-off between spatial resolution, temporal resolution and anatomical coverage. The fast T1-weighted spoiled gradient recalled echo sequence was used as it allows good contrast, medium sensitivity, high signal-to-noise ratio, adequate anatomical coverage and rapid data acquisition (Parker and Buckley, 2005).

The choice of days for data acquisition was determined by previous experience and based on literature data. A time point 24 hours after irradiation was chosen as the most likely time-point to detect early radiation response. A time point 9 days after irradiation was enough to detect late response and recovery of tissue. The choice of this time point was also limited by exponentially growing control tumors, so that they would not be too large and develop necrotic cores that would have sabotaged the data.

Arterial input function

AIF reflects physiological parameters such as cardiac output, vascular tonus, kidney clearance and injection timing. Theoretically, both AIF and tumor contrast agent concentration versus time should have been measured directly for each examination. However, AIF measurements are technically demanding and in the best case it produces an indirect measurement from a nearby large artery that may differ from the vessel supplying the tumor (O’Connor et al 2007). As a practical solution an idealized mathematical function can be used instead. This allows the experiment to be designed with a more freely choice of slice position, sequences and temporal resolution. The disadvantage of this approach is poor reflection of true blood supply (Parker and Buckley, 2005).

In our experiment an alternative approach was used. AIF was measured for 8 mice of the same size and age as the mice used in experiment. It was mature male mice, weighing 30-35 g. The calculated mean AIF of these 8 mice will not be fully true for mice receiving irradiation as weight and physiological conditions can change following treatment. Mice in the radiation groups lost some weight and looked more passive, which can correspond to decreased blood circulation. Castration also had an impact on mice weight and behavior. Despite the fact that AIF measurement has an impact on data analysis and that AIF can be defined for each group separately, the benefits of an increased number of mice used in the experiment are not clear. The alteration in AIF coefficients were suggested insignificant and thus the same AIF were used for all animals.

5.6.2 DW-MRI and ADC

Introduction

One of the approaches for characterization of tissue structure is to measure water diffusion in MR imaging. The practical breakthrough was made when Le Bihan in 1986 (Le Bihan et al 1986) and Moseley in 1990 (Moseley et al 1990) performed animal studies that demonstrated the value of DW-MRI for the early detection of stroke. Using diffusion tensor imaging, the directional dependence of molecular diffusion can be obtained. The main application of this method for cancer imaging is characterization of brain tumors, where ADC maps provide useful information regarding the architecture of the tissue (Charles-Edwards and deSouza 2006). Applications of DW-MRI over the past years include tissue characterization, monitoring of treatment response, diagnosing of acute ischemia, evaluation of brain tumors and detection of drug efficiency (Padhani et al 2009). In a recent report a promising role of DW-MRI in prostate cancer has been shown in detection, localization and assessment of prostate cancer aggressiveness and tumor staging. (Jacob et al 2008).

Inside the cells all the processes occur in small compartments, separated with membranes. As a result, the mean path length is small and the contribution of intracellular water diffusion to signal reduction is low. The main part of signal reduction for different pathologies occurs due to water diffusion in the extracellular volume. Larger and more compact packed cells in cancerous tissue lead to lower ADC values. The use of DW-MRI sequences can complement standard morphological MRI, MR spectroscopy and DCE-MRI and provide additional and supporting information in diagnosis of patients . It can be used for differentiation of highly cellular regions of tumors versus acellular regions and detection of treatment response (Charles-Edwards and deSouza 2006).

Analysis

As DW-MRI is a noninvasive approach, this technique can be used to monitor structural changes in tumor tissue for the same tumor over time. To obtain different diffusion weighting various b-values can be used. Low b-values (50 s/m^2 and 100 s/m^2) do not eliminate perfusion effects. Our results using these b-values gave no significant differences between the groups on the different days. The data we obtained from these acquisitions was of poor signal quality, arising due to technical issues with the scanner. Therefore, data from these b-values was not presented. In the result chapter, data for b=300 s/m^2 and b=600 s/m^2, when only free diffusion (Brownian displacement) and transmembrane transport contributes to signal decrease, was presented.

As it was already discussed above, radiation treatment and androgen-deprivation therapy can result in changes of tissue structure and changes in water diffusion. In the experiment, significant changes in mean ADC values were observed only for CWR22 tumors in non-castrated mice after radiation treatment. An insignificant initial decrease in ADC was observed 24 hours after treatment compared to pre-treatment values, followed by a significant increase at day 9 compared to day 1 and pre-treatment values. Ionizing radiation, causing endothelial apoptosis, leads to increase of vessel permeability for water. The resulting increase of the intracellular volume can be observed as a decreased ADC as compared to the pre-treatment values (Reide and Werner 2004). Rupture of cell membrane following radiation therapy can lead to membrane potential alteration, which is followed by failure of the Na-K-ATPase pump and ion canals, and a cytotoxic edema will form due to a shift of water from the extracellular to intracellular compartments. This will result in decreased mean ADC values. As cells will fail to repair sublethal cell damage or have microenvironment and metabolite failures, the cells will proceed to death. Water mobility will increase and manifest as increased ADC values. This corresponds to the above mentioned increases in Ve and K^{trans} as well as tumor volume on day 1. It has been showed that a high tumor ADC correlates with a high necrotic fraction (Herneth et al 2003). Animal and clinical studies have showed that an increase in ADC values early after treatment initiation is associated with a subsequent reduction in tumor volume. Galons *et al.* (Galons et al 1999) demonstrated a clear, substantial, and early increase in the ADC after successful chemotherapy in breast cancer. One of the reasons why no significant changes in ADC was observed 24 hours after irradiation can be that the observed volume reduction might be a result of decreased cell volume and no formation of necrotic areas. An increase of ADC at day 9 corresponds with the increase of Ve, suggesting that it represents an increase in the extracellular volume.

DW-MRI is being used to assess treatment response (Provenzale et al 2006, Manton et al 2006, Thoeny et al 2005). Mardor *et al.* in 2004 (Mardor et al 2004) demonstrated that pre-treatment ADC values of primary and metastatic malignant brain lesions could predict response to radiotherapy treatment, i.e. tumors with higher ADCs responded less favorably. In patients with locally advanced rectal cancer, low mean pre-treatment tumor ADC predicted a larger percentage size change of tumors after chemotherapy (Dzik-Jurasz et al 2002). Quantitative DW-MRI has also been shown to have potential to predict response of colorectal hepatic metastases to chemotherapy, suggesting that a high pre-treatment ADC predicts for a poor response (Scurr et al 2006). The results of each of these studies are consistent with the hypothesis that a high ADC may be indicative of tumor necrosis and consequently greater resistance to treatment. There was no significant difference between ADC values of CWR22 xenografts and androgen-deprived CWR22CA xenografts following radiation treatment. Moreover, no changes were observed in ADC between the control and radiationCWR22CA xenografts. Previously it has been suggested that tumors that receive androgen-deprivation treatment can be more hypoxic. But in our study, no samples were collected for histological staining to determine the necrotic fraction, cell density and size and compare with tumors with full testosterone supply.

Imaging Protocol

To obtain diffusion-weighted images a SSFSE-based DW-MRI sequence was used. It provides images without the significant degree of spatial distortions that single shot EPI sequences suffers from. EPI utilizes gradient rephasing, which results in spatial distortions from magnetic susceptibility effects, especially near air interfaces. In addition, EPI suffers from geometric image distortions created by significant eddy currents arising from the large magnetic field gradients used. For diffusion tensor imaging, encoding a minimum of six non-collinear diffusion encoding directions are required to measure the full diffusion tensor.

A source of artifact in DW-MRI is different kind of motion not related to diffusion. Body motion due to breathing or internal organ movement can be an example. To reduce motion-related artifacts some precautions were taken. Mice were anaesthetized under the whole procedure and the tumor was implanted on the back in the pelvic region, so no organ movement or breathing motion could affect the tumor. The mouse was placed in a special constructed bed where it was fixed. But even if all motion artifacts are eliminated, the effects of capillary microcirculation could influence the measured ADC values. Reported ADCs for viable tissue have often higher values than expected, as a result of additional signal attenuation caused by perfusion (Harriet et al 2004).

Chapter 6

Conclusion and suggestions for further work

The goal of the project was to investigate whether non-invasive magnetic resonance imaging (MRI) methods can be used to obtain information about changes in structural and physiological conditions of prostate cancer xenografts before and after hormone- and radiation therapy treatment and if parameters such as K^{trans}, V_e, fraction of unfitted voxels and ADC can monitor the treatment response. .

In this project the following results were obtained:

- CWR22 xenografts showed sensitivity to both radiation treatment and androgen deprivation, resulting in reduction of tumor volume. A strong correlation between tumor volume and prostate specific antigen were found, that correlated with earlier findings (Wainstein et al 1994). When data from mice with only untreated tumors was used in statistical analysis, the correlation was stronger. This suggests that the result of androgen deprivation or radiation on PSA and tumor volume appears on different time-points following treatment
- Tumor regrowth after radiation treatment was observed, but due to limited experimental time no relapse after androgen deprivation was achieved
- K^{trans} showed an early decrease 24 hours after radiation treatment and fraction of unfitted voxels increase, while no changes in PSA were observed. It can be suggested that K^{trans} can be used as an early predictor parameter for treatment response. The specific contribution of radiation-influenced changes in flow, endothelial permeability and endothelial surface cannot be identified only from K^{trans}.
- K^{trans} was negatively correlated with fraction of unfitted voxels, which can be attributed to treatment-induced increases in necrosis or tumor size-dependent increases in necrosis for untreated tumors
- No early changes in apparent diffusion coefficient (ADC) were found. An increase of ADC 9 days after irradiation corresponds with the increase of Ve, K^{trans} and tumor volume, suggesting that it represents an increase in the extracellular volume.
- Androgen deprived CWR22CA tumors had higher K^{trans} values and lower PSA levels than the CWR22 tumors at the time of inclusion into experiment. No difference in ADC were observed comparing to pretreatment values
- No significant changes in PSA, K^{trans}, Ve, fraction of unfitted voxels and ADC were observed in the CWR22CA xenografts the first 9 days after treatment. A dramatic decrease in PSA in the irradiated CWR22CA xenografts at the last day of the experiment (62 days after castration) corresponds with earlier findings (Agus et al 1999), where PSA levels for irradiated tumors has showed to be significantly lower than for untreated CWR22CA tumors. The absence of early response to radiation treatment can be suggested to be radiation resistance of CWR22CA.

It was shown that DCE-MRI, unlike DW-MRI, can be successfully applied for non-invasive monitoring of treatment response in an experimental tumor model. The study suggests that K^{trans} can be used as an early predictor for radiation treatment response while mean ADC failed.

As the experiment was conducted according to the rule of 3 R's (Replacement, Refinement and Reduction), the fewest possible number of mice were used. Due to high biological variation between xenografts and few mice in the experiment, one of the problems was to acquire enough data for statistical analyses. Considering this work as a pilot experiment further investigation should be done.

Based on the results of this work, some suggestions for future experiments are:

It was showed that 32 days after androgen deprivation the CWR22 tumor developed a radiation resistant phenotype. No significant changes in K^{trans}, Ve or ADC, as well as tumor volume or PSA, were observed in CWR22CA tumors after radiation treatment. From previous studies it has been reported that androgen-deprived tumors are hypoxic, thus the absence of response can be explained by a hypoxic start of androgen-deprived CWR22CA tumors. Further investigations should be made, including verification of the radiation resistance of CWR22CA tumors after relapse.

Post-radiation and post-castration changes in K^{trans} could be a result of blood flow or permeability changes alone or a combination of both. Therefore, additional information is needed to correctly analyze DCE-MRI data, e.g. immunohistochemistry. Immunohistological examination of histological sections using various antibodies can give information about cell density, apoptosis, necrosis, number of blood vessels, degree of blood flow and hypoxia. For quantification of hypoxia in tumors several exogenous markers can be applied, like pimonidazole, EF5 and CCI-103F (Ljungkvist et al 2007) that can capture normal conditions and treatment-related changes in hypoxia. A necrotic and hypoxic fraction and vascularization along with K^{trans} should be measured in order to understand the physiological mechanisms of K^{trans} changes and the role of hypoxia in this process. To correlate to ADC values, histological samples should be obtained for the same tumor at the same time point that MR acquisition is performed to determine the necrotic fraction, cell density and size and correlate these parameters with ADC values.

Chapter 7

Reference

Abbou CC, Salomon L, Hoznek A, et al. Laparoscopic radical prostatectomy: preliminary results. *Urology* 2000, 55:630-634

Agus DB, Cordon-Cardo C, Fox W, et al. Prostate Cancer Cell Cycle Regulators: Response to Androgen Withdrawal and Development of Androgen Independence *Journal of the National Cancer Institute*, 1999, 91(21)

Alexander AL, Lee JE, Lazar M, et al. Diffusion tensor imaging of the corpus callosum in autism. *Neuroimage*. 2007, 1(34):61–73.

Alexander AL, Tsuruda JS, Parker DL. Elimination of eddy current artifacts in diffusion-weighted echo-planar images: the use of bipolar gradients. *Magn Reson Med*. 1997, 38:1016–1021.

Alonzi R, Padhani A, Allen C Dynamic contrast enhanced MRI in prostate cancer *European Journal of Radiology* 2007, 63(3):335–350

Andersson S.O, Wolk A, Bergström R, et al. Body size and prostate cancer: a 20-year follow-up study among Swedish construction workers. *J Natl Canc Inst* 1997; 89:385-89.

Aus G, Abbou CC, Bolla M, et al. EAU guidelines on prostate cancer. *Eur Urol* 2005; 48:546–51

Aus G, Abbou CC, Bolla M, et al. EAU guidelines on prostate cancer. http://www.uroweb.org/fi leadmin/user_upload/Guidelines/ Prostate%20Cancer.pdf (accessed March 1, 2007).

Basser PJ, Mattiello J, LeBihan D. Estimation of the effective self-diffusion tensor from the NMR spin echo. *J Magn Reson B*. 1994, 103:247–254.

Basser PJ, Mattiello J, LeBihan D. MR diffusion tensor spectroscopy and imaging. *Biophys J*. 1994/2; 66:259–267.

Basser PJ, Pierpaoli C. A simplified method to measure the diffusion tensor from seven MR images *Magn Reson Med.* 1998, 39(6):928-34.

Bettencourt MC, Bauer JJ, Sesterhenn IA, et al. CD34 immunohistochemical assessment of angiogenesis as a prognostic marker for prostate cancer recurrence after radical prostatectomy. *J Urol 1998*; 160(2):459–65.

Bjørnerud A. The Physics of Magnetic Resonance Imaging. Compendie for the spring semester 2008, FYS –KJM 4760, Department of Physics, University of Oslo, 2006

Bloch F, Hansen WW, Packard M. Nuclear induction. *Phys. Rev*. 1946, 69, p.127

Bloch F, Hansen WW, Packard M. The nuclear induction experiment. *Phys. Rev*. 1946, 70, p.474

Bloch F. Nuclear induction, *Phys. Rev*. 1946, 70, p.460.

Bolla M, Collette L, Blank L, et al. Long-term results with immediate androgen suppression and external irradiation in patients with locally advanced prostate cancer (an EORTC study): a phase III randomised trial. *Lancet* 2002; 360: 103–08.

Borre M, Offersen BV, Nerstrom B, et al Microvessel density predicts survival in prostate cancer patients subjected to watchful waiting. *Br J Cancer* 1998; 78(7):940–4.

Bosland MC, Chung LWK, Greenberg NM, et al. Recent advances in the development of animal and cell culture models for prostate cancer research. *Urol Oncol* 1996, 2: 99-128

Bousquet JC, Saini S, Stark DD, et al. Gd-DOTA: characterization of a new paramagnetic complex. *Radiology* 1988, 166, p693

Boxma GC, Custer RP, Bosma MJ. A severe combined immunodeficiency mutation in the mouse. *Nature* 1983, 301: 527-530.

Bradley DP, Tessier JJ, Ashton SE, et al. Correlation of MRI biomarkers with tumor necrosis in Hras5 tumor xenograft in athymic rats. *Neoplasia*. 2007, 9(5):382-91.

Bray F. Cancer in Norway 2006 ISBN: 978-82-90343-69 -82

Bruchovsky N, Rennie PS, Coldman AJ, et al. Effects of androgen withdrawal on the stem cell composition of the Shionogi carcinoma. *Cancer Res* 1990; 50:2275–82.

Cannon L, Bishop DT, Skolnick M, et al. Genetic epidemiology of prostate cancer in the Utah Mormon genealogy. *Cancer Survey*. 1982; 1:47-69.

Carr DH, Brown J, Bydder GM, et al. Gadolinium-DTPA as a contrast agent in MRI: initial clinical experience in 20 patients. *AJR*, 1984; 143, p215

Catalona WJ, Scott WW. Carcinoma of the prostate. In: Walsh PC, Gittes RF, Perlmutter AD, Stamey TA, editors. Campbell’s Urology. vol 5. Philadelphia: WB Saunders Company; 1986. pp. 1463–1534.

Chapelon JY, Margonari J, Vernier F, et al. In vivo effects of high intensity field ultrasound on prostate adenocarcinoma Dunning R3327. *Cancer Res*. 1992, 52(22):6353-6357.

Charles-Edwards EM and deSouza NM. Diffusion-weighted magnetic resonance imaging application to cancer. *Cancer Imaging*, 2006, 6:135–143

Chin JL, Lim D, Abdelhady M. A review of primary and salvage cryoablation for prostate cancer. *Cancer Control*, 2007, 14(3):231-237

Christensson A, Laurell CB, Lilja H. Enzymatic activity of prostate-specific antigen and its reactions with extracellular serine proteinase inhibitors. *Eur J Biochem*. 1990, 194(3):755-63.

Corbett TH, Polin L, Roberts BJ, et al. Transplantable syngeneic rodent tumors. In Teicher BA, ed. Tumor Models in Cancer Research. Totowa, Humana Press, 2002, 41-71

D'Amico AV, Manola J, Loffredo M, et al. 6-month androgen suppression plus radiation therapy vs. radiation therapy alone for patients with clinically localized prostate cancer: a randomized controlled trial. *JAMA* 2004; 292:821–17.

D'Amico AV, Moul JW, Carroll PR, et al. Surrogate end point for prostate cancer-specific mortality after radical prostaectomy or radiation therapy. *J Natl Cancer Inst,* 2003

D'Amico AV, Renshaw AA, Sussman B, et al. Pretreatment PSA velocity and risk of death from prostate cancer following external beam radiation therapy. JAMA 2005; 294:440-47.

D'Amico AV, Whittington R, Malkowicz SB, et al. Biochemical outcome after radical prostatectomy, external beam radiation therapy, or interstitial radiation therapy for clinically localized prostate cancer. *JAMA* 1998; 280:969–74.

Dagnelie PC, Schuurman AG, Goldbohm RA, van den Brandt PA. Diet anthropometric measures and prostate cancer risk: a review of prospective cohort and intervention studies. *BJU Int* 2004; 93:1139-50.

Daldrup HE, Shames DM, Husseini W, et al. Quantification of the extraction fraction for gadopentetate across breast cancer capillaries. *Magn Reson Med* 1998; 40(4):537–43.

Damadian R. Tumor detection by nuclear magnetic resonance. *Science*. 1971, 171, p1151

Damber JE, Aus G. Prostate cancer *Lancet,* 2008; 371(9625):1710-21

Damber JE. Decreasing mortality rates for prostate cancer: possible role of hormonal therapy? *BJU Int* 2004; 93:695–701.

Dearnalay DP, Sydes MR, Graham JD, et al. Escalated-dose versus standard-dose conformal radiotherapy in prostate cancer: fi rst results from the MRC RT01 randomised controlled trial. *Lancet Oncol* 2007; 8:475–87.

Diamandis EP, Yousef GM, Clements J, et al. New nomenclature for the human tissue kallikrein gene family. *Clin Chem*. 2000; 46(11):1855-8.

Duffield-Lilico AJ, Dalkin BL, Reid ME, et al. Selenium supplementation, base line plasma selenium status and incidence of prostate cancer: an analysis of the complete treatment period of the Nutritional prevention of cancer trial. *BJU Int* 2003; 91:608-12.

Dyke JP., Zakian KL, Spees WM, et al. Metabolic Response of the CWR22 Prostate Tumor Xenograft after 20 Gy of Radiation Studied by 1H Spectroscopic Imaging *Clin Cancer Res*. 2003;9(12):4529-36

Dzik-Jurasz A, Domenig C, George M, et al. Diffusion MRI for prediction of response of rectal cancer to chemoradiation. *Lancet* 2002; 360(9329):307–8.

Eccles SA. Models for evaluation of targeted therapies of metastatic disease. In Teicher BA, ed. Tumor Models in Cancer Research. Humana Press, Totowa, 2002, 293-319.

Einstein A. Investigations on the Theory of the Brownian Movement. Dover Publications, Inc; 1956. p. 17

Etminan M, Takkouche B, Caamano-Isorna F. The role of tomato products and lycopenes in the prevention of prostate cancer: ameta-analysis of observational studies. *Cancer Epidemiol Biomarkers Prev* 2004; 13:340-45.

FitzGerald TJ, Simon E, Meyer J. Prostate carcinoma: opportunities for translational research. *J. Cell Biochem*. 2004, 91(3):433-442

FritzGerald TJ, Wang T, Goel HL, et al. Prostate carcinoma and radiation therapy: therapeutic treatment resistance and strategies for targeted therapeutic intervention. *Expert Rev Anticancer Ther*. 2008; 8(6):967-74.

Galbraith SM, Maxwell RJ, Lodge MA, et al. Combretastatin A4 phosphate has tumor antivascular activity in rat and man as demonstrated by dynamic magnetic resonance imaging. *J Clin Oncol* 2003; 21:2831-42

Galons JP, Altbach MI, Paine-Murrieta GD, et al. Early increases in breast tumor xenograft water mobility in response to paclitaxel therapy detected by noninvasive diffusion magnetic resonance imaging. *Neoplasia* 1999; 1:113–17.

Gerber GS, Thisted RA, Chodak GW, et al. Results of radical prostatectomy in men with locally advanced prostate cancer; multi-institutional pooled analysis. *Eur Urol* 1997; 32:385–90.

Giovanella BC, Yim SO, Stehlin JS, et al. Development of invasive tumors in the ‘‘nude’’ mouse after injection of cultured human melanoma cells. *JNCI* 1972, 48, p.1531-1533.

Goonewardene TI, Sowter HM, Harris AL. Hypoxia-induced pathways in breast cancer. *Microsc Res Tech* 2002; 59:41-8

Gospodarowicz M, O'Sullivan B. Prognostic factors in cancer. *Semin Surg Oncol.* 2003; 21(1):13-8.

Gregory CW, Sharief Y, Hamil KG, et al. Apoptosis in an androgendependent xenograft model derived from a primary human prostatic carcinoma. *Mol Biol Cell* 1995, 6:240

Grimm PD, Blasko JC, Ragde H. Ultrasound guided trans-perinealimplantation of iodine-125 and palladium-103 in the treatment of early stage prostate cancer. Technical concepts in planning,operative technique and evaluation. *Urol. Clin. North Am*. 1994, 2:113-125

Grönberg H, Damber L, Damber JE. Familial prostate cancer in Sweden. A nationwide register cohort study. *Cancer* 1996; 77:138-43.

Guillonneau B, Vallancien G. Laparoscopic radical prostatectomy: the Montsouris technique. *J Urol*. 2000; 163:1643-1649.

Hahn EL. Spin echoes. *Phys. Rev.* 1950, 80, p.580

Hall E, Giacca AJ (Eds). Radiology for the Radiologist. Lippincott, Williams & Wilkins 2006, Columbia University, NY, USA

Hall MC, Troncoso P, Pollack A, et al. Significance of tumor angiogenesis in clinically localized prostate carcinoma treated with external beam radiotherapy. *Urology* 1994; 44(6):869–75.

Harkness RA, Kilshaw BH and Hobson BM. Effects of large doses of anabolic steroids. *Br J Sports Med.* 1975; 9(2):70–73.

Harriet C, Thoeny MD, de Keyzer F, et al. Diffusion-weighted imaging of the parotid gland: Influence of the choice of b-values on the apparent diffusion coefficient value. *J Magn Reson Imaging,* 2004, 20:786-790

Harris R, Lohr KN. Screening for prostate cancer: an update of the evidence for the U.S. Preventive Services Task Force. *Ann Intern Med.* 2002;137(11):917-29.

Hartman TJ, Albanes D, Pietinen P, et al. The association between baseline vitamin E, selenium and prostate cancer in the alfa-tocopherol, beta-carotene prevention study. *Cancer Epidemiol Biomarkers Prev* 1998; 7:335-40.

Hasan K, Parker DL, Alexander AL. Comparison of gradient encoding schemes for diffusion-tensor MRI. *J Magn Reson Imaging.* 2001; 13:769–780.

Haselgrove JC, Moore JR. Correction for distortion of echo-planar images used to calculate the apparent diffusion coefficient. *Magn Reson Med*. 1996; 36:960–964.

Hashemi RH and Bradley Jr WG MRI The Basics. Williams and Wilkins, 1997

Hemmila I, Dakubu S, Mukkala VM, et al. Europium as a label in time-resolved immunofluorometry in assays *Anal. Biochem* 1984, 137:335-343

Hendriksen PJ, Dits NF, Kokame K, et al. Evolution of the androgen receptor pathway during progression of prostate cancer. *Cancer Res* 2006, 66:5012 - 5020

Herneth AM, Guccione S, Bednarski M. Apparent diffusion coefficient: a quantitative parameter for in vivo tumor characterization. *Eur J Radiol* 2003; 45:208–13.

Hodge KK, McNeal JE, Terris MK, et al. Random systematicenhancement in predictive accuracy provided by systemic biopsy in versus directed ultrasound-guided transrectal core biopsies of thepredicting outcome for clinically localized prostate cancer. *J Urol prostate*. 1989; 142:71-74.

Hsing AW, Chokkalingam AP. Prostate cancer epidemiology. *Front Biosci*. 2006; 11:1388-413

Hsu CY, Joniau S, Oyen R, et al. Outcome of surgery for clinical unilateral T3a prostate cancer: a single-institution experience. *Eur Urol* 2007; 51:121–28.

Huggins C, Hodges CV. Studies on prostate cancer. The effect of castration, of estrogen and of androgen injection on serum phosphatase in metastatic carcinoma of the prostate. *Cancer Res* 1941; 1:293–97.

Jackson MW, Bentel JM, Tilley WD. Vascular endothelial growth factor (VEGF) expression in prostate cancer and benign prostatic hyperplasia. *J Urol* 1997; 157(6):2323–8.

Jacobs MA, Ouwerkerk R, Petrowski K, et al. Diffusion-weighted imaging with apparent diffusion coefficient mapping and spectroscopy in prostate cancer. *Top Magn Reson Imaging*. 2008; 19(6):261-72

Jain RK, Safabakhsh N, Sckell A, et al. Endothelial cell death, angiogenesis, and microvascular function after castration in an androgen-dependent tumor: Role of vascular endothelial growth factor. *Proc Natl Acad Sci* 1998; 95:10820-25

Jamal K, Patel P, Sooriakumaran P Minimally invasive surgical modalities in the management of localized prostate cancer. *Expert Rev Anticancer Ther*. 2008; 8(6):957-66

Jayson GC, Parker GJ, Mullamitha S, et al. Blockade of platelet-derived growth factor receptor-beta by CDP860, a humanized, PEGylated di-Fab', leads to fluid accumulation and is associated with increased tumor vascularized volume. *J Clin Oncol* 2005, 23:973–981

Jemal A, Siegel R, Ward E, et al. Cancer statistics, 2008 CA *Cancer J Clin*. 2008; 58(2):71-96

Jezzard P, Balaban RS. Correction for geometric distortion in echo planar images from B0 field variations. *Magn Reson Med*. 1995; 34:65–73.

Jones DK, Horsfield MA, Simmons A. Optimal strategies for measuring diffusion in anisotropic systems by magnetic resonance imaging. *Magn Reson Med*. 1999; 42:515–525.

Joseph IB, Nelson JB, Denmeade SR, et al. Androgens regulate vascular endothelial growth factor content in normal and malignant prostatic tissue. *Clin Cancer Res* 1997; 3:2507–11.

Kauppinen RA. Monitoring cytotoxic tumour treatment response by diffusion magnetic resonance and proton spectroscopy. *NMR Biomed* 2002: 15:6-17.

Kelland L.R. Of mice and men: values and liabilities of the athymic nude mouse model in anticancer drug development *European Journal of Cancer* 2004, 40:827-836

Kennedy JE, Ter Haar GR, Cranston D. High intensity field ultrasound: surgery of the future? *Br J Radiol*. 2003, 76(909), 590-599

Khan F.M.. The Physics of Radiation Therapy. Lippincott Williams and Wilkins, 1994

Kolonel LN, Altshuler D, Henderson BE. The multiethnic cohort study: exploring genes, lifestyle and cancer risk. *Nat Rev Cancer* 2004; 4:519-27.

Kraaij R, Van Weerden WM, De Ridder CMA, et al. Validation of transrectal ultrasonographic volumetry for orthotopic prostate tumours in mice. *Lab Anim* 2002, 36:165–172

Larsson HB, Stubgaard M, Frederiksen JL, et al. Quantitation of blood-brain barrier defect by magnetic resonance imaging and gadolinium-DTPA in patients with multiple sclerosis and brain tumors. *Magn Reson Med* 1990; 16:117-31.

Le Bihan D, Breton E, Lallemand D, et al. MR imaging of intravoxel incoherent motions: application to diffusion and perfusion in neurologic disorders. *Radiology* 1986; 161:401–7.

Le Bihan D. Molecular diffusion, tissue microdynamics and microstructure. *NMR Biomed*. 1995; 8:375–386.).

Leach MO, Brindle KM, Evelhoch JL, et al. The assessment of antiangiogenic and antivascular therapies in early-stage clinical trials using magnetic resonance imaging: issues and recommendations. *Br J Cancer* 2005, 92:1599–1610

Lee AK. Radiation therapy combined with hormone therapy for prostate cancer. *Semin Radiat Oncol* 2006; 16:20-8.

Lilja H, Abrahamsson PA, Lundwall A et al. the predominant protein in human semen. Primary structure and identification of closely related proteins in the male accessory sex glands and on the spermatozoa. *J Biol Chem*. 1989; 264(3):1894-900.

Limpens J, Schröder FH, de Ridder CMA, et al. Combined lycopene and vitamin E treatment suppresses the growth of PC-346C human prostate cancer cells in nude mice. *J Nutr* 2006, 136:1287-1293

Ljungkvist ASE, Bussink J, Kaanders JHAM, van der Kogel AJ. Dynamics of tumor hypoxia measured with bioreductive hypoxic cell markers. *Radiat Res* 2007, 167:127-145

Loncaster JA, Carrington BM, Sykes JR, et al. Prediction of radiotherapy outcome using dynamic contrast enhanced MRI of carcinoma of the cervix. *Int J Radiat Oncol Biol Phys* 2002; 54:759-67.

Lovgren T, Hemmila I, Pettersson L, et al in time-resolved fluorometry in immunoassays. In Alternative Immunoassays, editor Collins WP, John Willey and Sons Ltd., England, 1985, p203-217

Lyng H, Dahle GA, Kaalhus O, et al. Measurement of perfusion rate in human melanoma xenografts by contrast-enhanced magnetic resonance. *Magnetic Resonance in Medicine*, 1998; 40:89-98.

Lynn LG, Putnam TJ. Histological and cerebral lesions produced by focused ultrasound. Ann. *J. Pathol*. 1944, 22(11):437-441

Madersbacher S, Pedevilla M, Vingers L, et al. Effect of high intensity focussed ultrasound on human prostate cancer in vivo. *Cancer Res*. 1995, 55(15):3346-3351

Maffezini M, Bossi A, Collette L. Implications of prostate specific antigen doubling time as indicator of failure after surgery or radiation therapy for prostate cancer. *Eur Urol* 2007; 51:605-13.

Maki HE, Saramaki OR, Shatkina L, et al. Overexpression and gene amplification of BAG-1L in hormone-refractory prostate cancer. *J Pathol* 2007, 212:395–401

Manton DJ, Chaturvedi A, Hubbard A, et al. Neoadjuvant chemotherapy in breast cancer: early response prediction with quantitative MR imaging and spectroscopy. *Br J Cancer* 2006; 94:427–35.

Mardor Y, Roth Y, Ochershvilli A, et al. Pretreatment prediction of brain tumors' response to radiation therapy using high b-value diffusionweighted MRI. *Neoplasia* 2004; 6:136–42

Marignol L, Coffey M, Lawler M, Hollywood D. Hypoxia in prostate cancer: A powerful shield against tumour destruction? *Cancer Treat Rev* 2008; 34:313– 27

Marques R, Erkens-Schulze SE, De Ridder CMA, et al. Androgen receptor modifications in prostate cancer cells upon long-term androgen ablation and antiandrogen treatment. *Int J Cancer* 2005, 117:221–229

Marques R, Van Weerden WM, S Erkens-Schulze SE, et al. The human PC346 xenograft and cell line panel: a model system for prostate cancer progression. *Eur Urology* 2006, 49:245–257

Mettlin C. Impact of screening on prostate cancer rates and trends. *Microsc Res Tech* 2000; 51:415-18.

Mettlin CJ, Murphy GP, Ho R, Menck HR. The National Cancer Data Base report on longitudinal observations on prostate cancer. *Cancer* 1996; 77:2162-66.

Millin T. Retropubic Urinary Surgery. London: Livingston; 1947.

Moffat BA, Hall DE, Stojanovska J, et al.. Diffusion imaging for evaluation of tumor therapies in preclinical animal models. *MAGMA* 2003: 17:249-259.

Moreira MV, de Almeida A, Costa RT and Perles LA. FXG mass attenuation coefficient evaluation for radiotherapy routine. *Journal of Physics: Conference Series* 2004, 3:146–149

Mori S, Barker PB. Diffusion magnetic resonance imaging: its principle and applications. *Anat Rec* 1999; 257:102–9.

Moseley ME, Kucharczyk J, Mintorovitch J et al. Diffusion-weighted MR imaging of acute stroke: correlation with T2-weighted and magnetic susceptibility-enhanced MR imaging in cats. *AJNR Am J Neuroradiol* 1990; 11:423–9.

Moule RN and Hoskin PJ. Non-surgical treatment of localised prostate cancer. *Surg Oncol.* 2009 May 11. [Epub ahead of print]

Müller H, Brenner H. Urine markers as possible tools for prostate cancer screening: Review of performance characteristics and practicality. *Clin Chem* 2006; 52:562-73.

Murat FJ, Poissonnier L, Pasticier G,Gelet A. High intensity field ultrasound (HIFU) for prostate cancer. *Cancer Control* 2007, 14(3):244-249

Navone NM, Logothetis CJ, von Eschenbach AC, Troncoso P Model systems of prostate cancer: uses and limitations. *Cancer and Metastatic Rev* 1999, 17: 361 - 371

Nicholson B, Theodorescu D. Angiogenesis and prostate cancer tumor growth. *J Cell Biochem* 2004; 91:125-50

O'Connor JPB, Jackson A, Parker GJM et al DCE-MRI biomarkers in the clinical evaluation of antiangiogenic and vascular disrupting agents *British Journal of Cancer* 2007, 96:189–195

Oberaigner W, Horninger W, Klocker H, et al. Reduction of prostate cancer mortality in Tyrol, Austria after introduction of prostate-specific antigen testing. *Am J Epidemiol* 2006; 164:376-84

Ohori M, Kattan MV, Koh H, et al. Predicting the presence and side of extracapsular extension: a nomogram for staging prostate cancer. *J Urol* 2004; 17:1844-49

Padhani AR, Harvej CJ, Cosqrove DO. Angiogenesis imaging in the management of prostate cancer. *Nat Clin Pract Urol* 2005: 2(12):596-607.

Padhani AR, Liu G, Mu-Koh D, et al. Diffusion-Weighted Magnetic Resonance Imaging as a Cancer Biomarker: Consensus and Recommendations *Neoplasia*. 2009, 11(2):102–125

Padhani AR. Dynamic contrast-enhancedMRIin clinical oncology: current status and future directions. *J Magn Reson Imaging* 2002; 16(4):407–22.

Papadakis NG, Xing D, Huang CL, et al. A comparative study of acquisition schemes for diffusion tensor imaging using MRI. *J Magn Reson*. 1999; 137:67–82.

Parker GJM, Buckley DL. Tracer kinetic modelling for T1-weighted DCE-MRI in dynamic contrast-enhanced magnetic mesonance mmaging in oncology Jackson A, Buckley DL, Parker GJM (eds), p 81–92. Berlin: Springer 2005

Partin AW, Mangold LA, Lamm DM, et al. Contemporary updates of the prostate cancer staging nomograms (Partin Tables) for the new millenium. *Urology* 2001; 58: 843-48

Pasteau O, Degrais P. De l'emploi du radium dans le traitement des cancers de la prostate. *J. D'urologie Medicale et Chirurgicale* 1919, 4:341-366

Petrylak DP, Tangen CM, Hussain MH, et al. Docotaxel and estramustine compared with mitoxantrone and prednisone for advanced refractory prostate cancer. *N Engl J Med* 2005; 351:1513–20.

Pickles T, Pollack A. The case for dose escalation versus adjuvant androgen deprivation therapy for intermediate risk prostate cancer. *Can J Urol* 2006; 13 (suppl 2):68–71.

Plaskon LA, Penson DF, Vaughan TL, Stanford JL. Cigarette smoking and risk of prostate cancer in middle-aged men. *Cancer Epidemiol Biomarkers Prev* 2003; 12:604-09.

Plowman J, Dykes DJ, Hollingshead M, et al.. Human tumor xenograft models in NCI drug development. In:TeicherB, ed, Anticancer Drug Development Guide: Preclinical Screening, Clinical Trials and Approval. Humana Press, Totowa, NJ, 1997, p101-125.

Pollack A, Zagars GK, Starkschall G, et al. Prostate cancer radiation dose response: results of the MD Anderson phase III randomized trial. *Int J Radiat Oncol Biol Phys* 2002; 53:1097–105.

Potosky AL, Feuer EJ, Levin DL. Impact of screening on incidence and mortality of prostate cancer in the United States. *Epidemiol Rev* 2001; 23:181-86.

Pretlow TG, Wolman SR, Micale MA, et al. Xenografts of primary human prostatic carcinoma. *J Natl Cancer Inst* 1993, 85:394-398

Provenzale JM, Mukundan S, Barboriak DP. Diffusion-weighted and perfusion MR imaging for brain tumor characterization and assessment of treatment response. *Radiology* 2006; 239:632–49.

Purcell E.M., H.C. Torrey, R.V. Pound. Resonance absorption by nuclear magnetic moments in a solid. *Phys. Rev*. 1946, 69, p37

Rebillard X, Davin JL, Soulie M. Treatment by HIFU of prostate cancer: a survey of literature and treatment indications. *Prog. Urol*. 2003, 13(6):1428-1456

Reese TG, Heid O, Weisskoff RM, Wedeen VJ. Reduction of eddy-current-induced distortion in diffusion MRI using a twice-refocused spin echo. *Magn Reson Med*. 2003;49: 177–182.

Richardson TD, Wojno KJ, Liang LW, et al. Half-life determination of serum free prostate-specific antigen following radical retropubic prostatectomy. *Urology* 1996, 48:40-44

Riede U., Werner M. Color atlas of pathology: pathologic principles, associated diseases, sequela / ISBN 3-13-127781-5 (GTV) Stuttgart ; Thieme, 2004 457 pages.

Røe K, Muren LP, Rørvik J, et al. Dynamic contrast enhanced magnetic resonance imaging of bladder cancer and implications for biological image-adapted radiotherapy. *Acta Oncol* 2008; 47:1257-64.

Røe K. In vivo Magnetic Resonance Spectroscopy and Diffusion Weighted Magnetic Resonance Imaging for Non-Invasive Monitoring of Treatment Response of Subcutaneous HT29 Xenografts in Mice. *Master thesis, NTNU* spring 2006

Rothermund CA, Gopalakrishnan VK, Eudy JD, Vishwanatha JK. Casodex treatment induces hypoxia-related gene expression in the LNCaP prostate cancer progression model. *BMC Urol* 2005; 5:5

Rubin MA, Buyyounouski M, Bagiella E, et al. Microvessel density in prostate cancer: lack of correlation with tumor grade, pathologic stage, and clinical outcome. *Urology* 1999; 53(3):542–71

Ruizeveld de Winter JA, Janssen PJ, Sleddens HM, et al. Androgen receptor status in localized and locally progressive hormone refractory human prostate cancer. *Am J Pathol* 1994, 144:735–746

Rygaard J, Povlsen CO. Heterotransplantation of a human malignant tumour to the mouse mutant ‘‘nude’’. *Acta Pathology Microbiol Scand* 1969, 77:758-760

Schroder FH, Kranse R, Barbet N, et al. Prostate-specific antigen: A surrogate endpoint for screening new agents against prostate cancer? *Prostate* 2000, 42:107–115

Schuessler WW, Schulam PG, Clayman RV, et al. Laparoscopic radical prostatectomy: initial short-term experience. *Urology*. 1997; 50:854-857

Scurr E, Collins DJ, Kanber B, et al. Detection of colorectal liver metastases by diffusion-weighted imaging. *Proc Int Soc Mag Reson Med* 2006; 14:401

Seierstad T, Røe K, Høvik B. Construction of a modified capacitive overlap MR coil for imaging of small animals and objects in a clinical whole-body scanner. *Phys Med Biol*. 2007; 52(22):513-22

Shimony JS, McKinstry RC, Akbudak E, et al. Quantitative diffusion-tensor anisotropy brain MR imaging: normative human data and anatomic analysis. *Radiology*. 1999; 212:770–784.

Shrager RI, Basser PJ. Anisotropically weighted MRI. *Magn Reson Med*. 1998; 40:160–165.

Simmons MN, Stephenson AJ, Klein EA. Natural history of biochemical recurrence after radical prostatectomy: risk assessment for secondary therapy. *Eur Urol* 2007; 51:1175–84.

Sobin LH Wittekind C, editors. TNM classification of malignant tumours 6th edition. New-York: Wiley-Liss, 2002

Soini E and Kojola H. Time-resolved fluorometer for lanthanide chelated – a new generation og nonisotropic immunoassays. *Clin. Chem* 1983, 29:65-68

Sowery RD, So AI, Gleave ME. Therapeutic options in advanced prostate cancer: present and future. *Curr Urol Rep* 2007; 8:53–59.

St Lawrence KS, Lee TY.An adiabatic approximation to the tissue homogeneity model for water exchange in the brain: I. Theoretical derivation. *J Cereb Blood Flow Metab*. 1998; 18(12):1365-77

Steinberg GD, Carter BS, Beaty TH, et al. Family history and the risk of prostate cancer. *Prostate* 1990; 17:337-47.

Stejskal E.O., J.E. Tanner.Spin diffusion measurements: spin echoes in the presence of a time-dependent field gradient. *J. Chem. Phys*. 1965, 42, p288

Stenman UH, Abrahamsson PA, Aus G, et al. Prognostic value of serum markers for prostate cancer. *Scand J Urol Nephrol* 2005; 39:64-81

Stenman UH, Leinonen J, Alfthan H, et al. A complex between prostate-specific antigen and alpha 1-antichymotrypsin is the major form of prostate-specific antigen in serum of patients with prostatic cancer: assay of the complex improves clinical sensitivity for cancer. *Cancer Res*. 1991; 51(1):222-6.

Tannock IF, de Wit R, Berry WR, et al. Doxetaxel plus prednisone or mitoxantrone plus prednisone for advanced prostate cancer. *N Engl J Med* 2004; 351:1502–12.

Thalmann GN, Sikes RA, Chang SM, et al. Suramin-induced decrease in prostate-specific antigen expression with no effect on tumor growth in the LNCaP model of human prostate cancer. *J Natl Cancer Inst* 1996, 88:794 – 801

Thoeny HC, De Keyzer F, Chen F, et al. Diffusion-weighted MR imaging in monitoring the effect of a vascular targeting agent on rhabdomyosarcoma in rats. *Radiology* 2005; 234:756–64.

Thompson I, Trasher JB, Aus G, et al. Guideline for the mangement of clinically localized prostate cancer: 2007 update. *J Urol* 2007; 177:2106–131.

Tofts PS Modeling tracer kinetics in dynamic Gd-DTPA MR imaging. *J Magn Reson Imaging* 1997, 7:91–101

Tofts PS, Brix G, Buckley DL, et al. Estimating kinetic parameters from dynamic contrastenhanced T^1-weighted MRI of a diffusable tracer: standardized quantities and symbols. *J Magn Reson Imaging* 1999, 10:223–232

Tofts PS, Brix G, Buckley DL, et al. Estimating kinetic parameters from dynamic contrast-enhanced T1-weighted MRI of a diffusible tracer: Standardized quantities and symbols. *J Magn Reson Imaging* 1999;1 0:223-32

Tofts PS, Kermode AG. Measurement of the blood–brain barrier permeability and leakage space using dynamic MR imaging. 1. Fundamental concepts. *Magn Reson Med* 1991, 17:357–367

Tomlins SA, Rhodes DR, Perner S, et al. Recurrent fusion of TMPRSS2 and ETS transcription factor genes in prostate cancer. *Science* 2005; 310:644-48.

Trachtenberg J. Experimental treatment of prostatic cancer by intermittent hormonal therapy. *J Urol* 1987; 137:785–88.

Van Bokhoven A, Caires A, Maria MD, et al. Spectral karyotype (SKY) analysis of human prostate carcinoma cell lines. *Prostate* 2003, 57:226-244

Van Weerden WM, Bangma C, de Wit R. Human xenograft models as useful tools to assess the potential of novel therapeutics in prostate cancer. *Br J Cancer*. 2009; 100(1):13-8.

Van Weerden WM, De Ridder CMA, Verdaasdonk CL, et al. Development of seven new human prostate tumor xenograft models and their histopathological characterization. *Am J Pathol* 1996, 149:1055–1062

Veldscholte J, Berrevoets CA, Ris-Stalpers C, et al. The androgen receptor in LNCaP cells contains a mutation in the ligand binding domain which affects steroid binding characteristics and response to antiandrogens. *J Steroid Biochem Mol Biol* 1992, 41:665-669

Vlietstra RJ, van Alewijk DC, Hermans KG, et al. Frequent inactivation of PTEN in prostate cancer cell lines and xenografts. *Cancer Res* 1998, 58:2720-2723

Wainstein MA, He F, Robinson D, et al. CWR22: Androgen-dependent xenograft model derived from a primary human prostatic carcinoma. *Cancer Res* 1994, 54:6049-6052

Wainstein MA, He F, Robinson D, et al. CWR22: androgen-dependent xenograft model derived from a primary human prostatic carcinoma. *Cancer Res.* 1994; 54(23):6049-52.

Wallner K, Merrick G, True L, et al. Iodine-125 versus Palladium-103 for low risk prostate cancer: morbidity outcomes from a prospective randomised multi-center trial. *Cancer J.* 2002, 8(1):67-73

WHO http://www.who.int/mediacentre/factsheets/fs297/en/

Widmark A, Klepp O, Solberg A, et al. Endocrine treatment, with or without radiotherapy, in locally advanced prostate cancer (SPCG-7/SFUO-3): an open randomised phase III trial. *Lancet* 2009; 373:301-8.

Wolf GL, Fobben ES The tissue proton T1 and T2 response to gadolinium DTPA injection in rabbits. A potential renal contrast agent for NMR imaging. *Invest Radiol.* 1984; 19(4):324-8.

Wong YN, Mitra N, Hudes G, et al. Survival associated with treatment vs observation of localized prostate cancer in elderly men. *JAMA* 2006; 296:2683–93

Yagoda A, Petrylak DP Cytotoxic chemotherapy for advanced hormone-resistant prostate cancer. *Cancer* 1993, 71:1098–1109

Young HH. The early diagnosis and radical cure of carcinoma of the prostate: being a study of 40 cases and presentation of a radical operation which was carried out in four cases. *Bull Johns Hopkins Hosp.* 1905, 16:315.

Zietman AL, DeSilvio ML, Slater JD, et al. Comparison of conventional-dose vs high-dose conformal radiation therapy in clinically localized adenocarcinoma of the prostate: a randomized controlled trial. *JAMA* 2005; 294:1233–39.

Chapter 8

Appendix 1

Based on some of the results from this thesis, a manuscript has been prepared for submission.

Vascularization and radiation response in androgen-sensitive prostate carcinoma xenografts under androgen-exposed and androgen-deprived conditions

[1,2]Kathrine Røe, [1,3]Therese Seierstad, [1]Alexandr Kristian, [1]Gunhild Mari Mælandsmo, [4]Albert J. van der Kogel, [1,5]Anne Hansen Ree, [1,2]Dag Rune Olsen

[1]Institute for Cancer Research, Oslo University Hospital, Oslo, Norway,

[2]Faculty Division The Norwegian Radium Hospital, University of Oslo, Oslo, Norway,

[3]Buskerud University College, Department of Health Sciences, Drammen, Norway,

[4]Department of Radiation Oncology, Radboud University, Nijmegen Medical Center, Nijmegen, The Netherlands,

[5]Faculty Division Akershus University Hospital, University of Oslo, Oslo, Norway

Running title: Vascularization in androgen-sensitive prostate cancer

Keywords: CWR22, prostate cancer, K^{trans}, radiation therapy, androgen deprivation therapy

Abstract

Purpose: Most prostate cancers (PCa) show initial favorable response following androgen-deprivation therapy (ADT). Clinical evidence suggests that combining neoadjuvant or adjuvant ADT with radiation therapy improves local control and disease-free survival for PCa patients as compared to radiation therapy alone. We investigated whether tumor vasculature in androgen-sensitive CWR22 PCa xenografts is altered following ADT and whether ADT affects radiation response.

Experimental design: Mice bearing androgen-sensitive CWR22 PCa xenografts were allocated into four groups receiving combinations of ADT by castration (CWR22c) and radiation delivered as a 15 Gy single dose at day 0. Non-invasive visualization of tumor vasculature by dynamic contrast-enhanced magnetic resonance imaging (DCE MRI) was performed pre-radiation (day 0) and twice after radiation (days 1 and 9). The hemodynamic transfer constant K^{trans}, reflecting vascular permeability, vascular surface area and flow, was calculated voxel-wise from DCE MRI.

Results: K^{trans} of pre-radiation CWR22c tumors was 47 % higher than of pre-radiation CWR22 tumors ($p = 0.01$). Androgen-deprived CWR22c tumors showed no significant changes in K^{trans} following radiation, whereas K^{trans} in androgen-exposed tumors decreased from day 0 to day 1 ($p = 0.04$), followed by an increase from day 1 to day 9 ($p = 0.01$). There was a positive correlation between prostate specific antigen (PSA) and tumor volume ($r = 0.59$, $p < 0.01$).

Conclusions: Vascularization differs between androgen-exposed CWR22 xenografts and androgen-deprived CWR22c xenografts, with these two phenotypes also presenting different

radiation response. The study suggests serial monitoring of K^{trans} to be a useful indicator of therapy responses in PCa.

Introduction

Androgens are the primary regulators of prostate cancer (PCa) growth and proliferation (1). The effects of androgen-deprivation therapy (ADT) on prostatic carcinoma are significant, particularly for clinically localized disease. ADT results in cytological changes and a reduction in tumor cells due to a shift to quiescence and apoptosis (2, 3). Although ADT effectively causes dormancy and reduced tumor burden, complete eradication of PCa rarely occurs and biochemical progression in high-risk PCa patients receiving ADT is usually evident within 2 years. The mechanisms involved in the early transition from androgen-sensitive to androgen-resistant PCa are not fully understood, with the androgen-resistant state remaining incurable.

Dynamic contrast-enhanced magnetic resonance imaging (DCE MRI) allows repeated, non-invasive visualization of tumor vasculature and has been suggested to become a tool in clinical response monitoring of increased and inhibited angiogenesis. Signal enhancement in DCE MRI is a function of microvessel density, vessel structure and rate of blood flow, and thus has the potential of assessing treatment-induced biological effects on tissue vasculature. Average tumor signal enhancement following contrast administration has been anticipated to decrease with increasing tumor volume due to insufficient vascular supply and development of regions of hypoxia and necrosis. However, studies have shown that tumor signal enhancement is independent of tumor volume (4, 5) and that DCE MRI provides supplementary information of intratumoral conditions not available using standard, anatomical MRI.

Radiation therapy is an important treatment modality for PCa, although its efficacy decreases with increasingly advanced stage. Clinical trials have shown that combining neoadjuvant or adjuvant ADT with radiation therapy improves local control and disease-free survival for PCa patients as compared to radiation therapy alone, especially for high-risk patients (6, 7). Technological advances have brought intensity-modulated radiation therapy and high dose-rate brachytherapy into the clinic, allowing increased tumor doses while sparing normal tissues. These techniques require non-invasive imaging modalities, such as DCE MRI, for accurate localization of tumor masses. Radiation therapy failure includes extensive tumor masses, androgen-resistant metastatic disease and inherent radioresistance, warranting the use of DCE MRI to obtain information of vascular structure that can become useful in evaluation of radiation therapy response for PCa patients.

In this study the contrast agent gadolinium diethylenetriamine pentaacetic acid (Gd-DTPA) was employed because of its wide availability and established clinical use. Using quantitative pharmacokinetic modeling of contrast agent uptake in a tissue of interest, vascular kinetic biomarkers associated with underlying physiological processes can be derived and used in monitoring response to treatments. The forward volume transfer constant between blood plasma and extravascular extracellular space (EES), K^{trans}, has been shown to reflect acute treatment-induced changes in tumor vascularization (8). Although K^{trans} can be derived using a range of compartmental models, the model of Tofts and Kermode is the most commonly used both in clinical and preclinical models (8 - 10). The Tofts and Kermode model is based on contrast moving passively between two compartments, plasma and EES, and the transfer constant, K^{trans}, between these two compartments, is dependent on a combination of blood flow, vascular density, vascular surface area and permeability of the vasculature.

The specific aims of the present study were to investigate if tumor vasculature in androgen-sensitive CWR22 PCa xenografts grown in mice is altered following ADT by castration and if ADT affects radiation response.

Materials and Methods

Animals and xenografts

Male, sexually mature BALB/c nude mice (25 – 35 g, 6 - 8 weeks old) were used in this study. The Institutional and National Committee on Research on Animal Care approved the protocol, and the experiment was performed according to Interdisciplinary Principles and Guidelines for the Use of Animals in Research, Marketing and Education (New York Academy of Science, New York, NY). The mice were bred at the animal department of our institute and kept under specific pathogen-free conditions at constant temperature (21.5 – 22.5 °C) and humidity (50 – 60 %), and given sterilized food and water *ad libitum*.

Xenografts were generated by subcutaneous (s.c.) implantation of $(\sim 2\text{ mm})^3$ tumor tissue from the human androgen-sensitive CWR22 xenograft into one flank of each mice. Procedures for implantation, growth and harvesting of CWR22 xenografts in mice were as described in (11, 12). Animals with CWR22 xenografts were included into the experiment when their shortest tumor diameter reached 8 mm. Androgen-deprived CWR22 xenografts, denoted CWR22c, were obtained by castration of animals bearing CWR22 xenografts. The surgical castration was performed at a shortest tumor diameter of 13 mm, and the animals were included into the experiment when the CWR22c xenografts had regressed to a shortest tumor diameter of 8 mm. The time from castration to inclusion was 36 ± 4 days.

Thirty-two animals were randomly allocated into 4 groups of 8 animals: CWR22 control, CWR22 irradiation, CWR22c control and CWR22c irradiation. For the CWR22 groups, all animals in the group were sacrificed when the longest tumor diameter of two of the tumors in the group reached 16 mm. Animals with CWR22c tumors were sacrificed 30 days after inclusion into the experiment.

To determine a mean vascular input function needed in pharmacokinetic modeling of contrast enhancement curves, eight separate male mice with identical weight and age as the other 32 animals were subjected to left ventricular DCE MRI examinations.

Tumor tissue sections from control and 1 day post-radiation CWR22 xenografts (n = 8) were used in immunohistochemistry to assess acute radiation-induced changes in tumor vascularization, perfusion and hypoxia.

Tumor volume

Tumor volumes were estimated using caliper measurements from implantation until the end of the experiment using the formula *(length* × *length* × *width)/2*, with *length* being the longest diameter across the tumor and *width* the corresponding perpendicular.

Radiotherapy

Tumors in the two radiation groups received a single dose of 15 Gy on day 0 (after pre-radiation MRI) using a ^{60}Co source (Mobaltron 80, TEM Instruments, Crawley, UK) with a dose rate of 0.8 Gy/min. Only the tumor was irradiated, while keeping the rest of the body outside the radiation field. A homogenous tumor dose deposition was achieved by placing a 5 mm polystyrene bolus on top of the tumors to avoid the initial dose buildup from the cobalt source.

Anesthesia and analgesia

Animals were anesthetized with s.c. injections of a mixture of 2.4 mg/ml tiletamine and 2.4 mg/ml zolazepam (Zoletil vet, Virbac Laboratories, Carros, France), 3.8 mg/ml xylazine (Narcoxyl vet, Roche, Basel, Switzerland), and 0.1 mg/ml butorphanol (Torbugesic, Fort Dodge Laboratories, Fort Dodge, IA), diluted 1:5 in sterile water. A dose of 50 µl/10 g of body weight was given prior to radiation, and 75 µl/10 g of body weight before MRI acquisitions and castration. Analgesia was provided to castrated animals by s.c. injections of buprenorphine (Temgesic; Schering-Plough, Brussels, Belgium) in a dose of 0.1 mg/kg.

DCE MRI acquisition

DCE MRI of the tumors' central slice was acquired at day 0 (prior to radiation), day 1 (24 h after radiation) and day 9 using a 1.5 T GE Signal LS clinical scanner (GE Medical Systems, Milwaukee, WI). Weight of individual animals determined the amount of contrast agent (Gd-DTPA; Magnevist®, Schering, Berlin, Germany) diluted in heparinized saline to 0.06 M) to be administrated. Prior to MRI, a heparinized 24-gauge catheter attached to a cannula containing 0.01 ml g^{-1} body weight saline-diluted Gd-DTPA, was inserted into the tail vein. The animals were placed in a special cradle and put into an in-house built MR mouse coil (13) before the coil was placed in the scanner. The animals' temperature was maintained at 38°C during the acquisition.

MRI included axial fast spin-echo T2-weighted images (TE_{eff} = 85 ms; TR = 4000 ms; echo train length (ETL) = 16; image matrix = 256 × 256; field of view (FOV) = 4 cm; slice thickness = 2 mm) to localize tumor, and dynamic fast spoiled gradient-recalled (FSPGR) T1-weighted images (TE = 6.3 ms, TR = 120 ms, image matrix = 256 × 128, FOV = 6 cm, slice thickness = 1 mm, flip angle (FA) = 80°) to investigate contrast kinetics. Following 5 pre-contrast images, Gd-DTPA was manually injected during 3 s before continuing dynamic post-contrast imaging for 20 minutes with 12 s time resolution. Reconstructed voxel size of T1-weighted images was $0.23 \times 0.47 \times 1$ mm^3. Corresponding proton density images (TE = 4.4 ms, TR = 360 ms, image matrix = 256 x 128, FOV = 6 cm, slice thickness = 1 mm, FA = 10°) were acquired prior to and after DCE MRI.

Mean vascular input functions (VIFs) were obtained from DCE MRI of the left ventricle in eight separate male mice. The imaging protocol was identical to the one above except for TR = 200 ms for the proton density images, and TR = 80 ms, image matrix = 512 × 256, and slice thickness = 2 mm for the T1-weighted images (voxel size $0.11 \times 0.23 \times 2$ mm^3). T1-weighted imaging consisted of 120 post-contrast images acquired every 10 s. Acquired images were stored in DICOM format and transferred to a remote PC for further data analysis.

DCE MRI analysis

DCE MRI analysis was performed using in-house written programs in IDL (Interactive Data Language v6.2, Research Systems Inc., Boulder, CO). Gd-DTPA concentrations were calculated from signal intensities and proton density images using the method of Hittmair *et al* (14). Individual VIFs were determined by fitting a biexponential function to concentration curves from the left ventricle according to the following formula:

$$VIF = A \exp(-Bt) + C \exp(-Dt) \qquad \text{(Eq. 1)}$$

with A and B representing equilibration of Gd-DTPA between plasma and extracellular space, C and D representing kidney clearance of Gd-DTPA and $(A + C)^{-1}$ (l/kg) representing plasma volume of the mouse per unit of body weight. Mean VIF for the eight mice were found to be characterized by the following constants: A = 3.57 ± 0.34 mM, B = 0.025 ± 0.005 s^{-1}, C = 1.45 ± 0.15 mM, D = 0.0074 ± 0.0036 s^{-1}. This VIF was assumed to be valid for all mice in the experiment.

A region-of-interest (ROI) was manually delineated around the solid tumor in T1-weighted images, excluding surrounding skin and connective tissue. Using the mean VIF parameters and contrast enhancement curves for individual voxels within the selected ROI, each voxel was fitted to the model of Tofts and Kermode (10). This allowed voxel-by-voxel estimations of the forward volume transfer constant for Gd-DTPA between blood plasma and the EES, K^{trans} (s^{-1}) (8), across the tumor.

Unfitted voxels represent voxels were the fit failed to converge due to low Gd-DTPA uptake or voxels with negative values ($K^{\mathrm{trans}} < 0$). All unfitted voxels were set equal to 0 and included in K^{trans} maps and in calculation of mean tumor K^{trans}. The fraction of unfitted voxels, scored as the sum of unfitted voxels versus the total number of voxels within the tumor ROI, was monitored.

PSA

Blood to PSA analysis were collected from the tail vein of each animal at days 0, 1 and 9 and at the time of sacrifice. Blood samples were allowed to coagulate before being centrifuged and frozen at -80°C until analysis. Free and total PSA were assayed using the fluoroimmunonometric AutoDELFIA ProStatus$^{\mathrm{TM}}$ PSA Free/Total kit (PerkinElmer Life and Analytical Sciences, Wallac Oy, Turku, Finland).

Immunohistochemistry

Hypoxia was determined by injecting 80 mg/kg pimonidazole hydrochloride (1-[(2-hydroxy-3-piperidinyl)propyl]-2-nitroimidazole hydrochloride, Natural Pharmaceuticals, International Inc., Research Triangle Park, NC, USA) in 0.5 ml saline intraperitoneally (i.p.) 60 min before sacrificing the animals. Five minutes prior to sacrifice, 15 mg/kg Hoechst 33342 (Sigma Chemical Co., St Louis, MO, USA) in 0.1 ml saline was injected i.v. for determination of tumor perfusion. Immediately after dissection, tumors were cut in two halves, frozen in liquid nitrogen and stored at -80°C until they were shipped to the Department of Radiation Oncology, Radboud University, Nijmegen Medical Center, Nijmegen, The Netherlands, for staining and imaging.

The central slice of the one half was cut before staining, and scanned according to procedures identical to as in (15) to obtain triple immunofluorescent images of tumor vasculature (9F1; TCL image, TNO, Delft, The Netherlands), perfusion (Hoechst) and hypoxia (pimonidazole).

Statistical analysis

Statistical analysis was performed using SPSS 16.0 (SPSS, Cary, NC). Differences between groups and time-points were analyzed using two-sided t-tests under conditions of normality. Pearson’s correlation test analyzed whether correlations between variables were significant. Results are presented as mean ± standard error of the mean (SEM) and a significance level of 5 % were used in all statistical analyses.

Results

Tumor growth

Pre-treatment tumor volumes were normally distributed ($p = 0.60$) with a mean tumor volume of 392.1 ± 37.7 mm^3. Figure 1 shows normalized tumor volumes for control and irradiated CWR22 and CWR22c tumors.

Exponentially growing CWR22 control tumors showed a 2.5-fold increase ($p < 0.01$) from day 0 to day 9. At the completion of the study (day 65), volumes of these tumors had increased 9.6-fold as compared to baseline. Radiation of CWR22 tumors induced an initial 0.3-fold ($p < 0.01$) tumor volume regression at day 1, followed by 1.3-fold tumor re-growth at day 9. Irradiated CWR22 tumors showed growth inhibition before slowly relapsing from day 51 and onwards. At day 30, mean normalized tumor volumes of irradiated CWR22 tumors were 12-fold less ($p < 0.01$) than tumor volumes of control CWR22.

Volumes of tumors in the CWR22c cohorts decreased continuously as long as the experiment lasted. Thirty days after initiation of the study, volumes of control and irradiated tumors had decreased to 0.6-fold ($p < 0.01$) and 0.4-fold ($p < 0.01$) of pre-treatment values, respectively.

PSA

Figure 2a shows total PSA measured in the four groups at days 0, 1 and 9 and at the day of sacrifice. Mean pre-treatment total PSA was 30.7 ± 6.0 µg/ml for animals bearing CWR22 tumors, whereas total PSA for castrated animals bearing CWR22c tumors was 18.3 ± 3.2 µg/ml. For animals bearing control CWR22 tumors, total PSA increased to 88.2 ± 12.5 µg/ml

($p < 0.01$) and 212.4 ± 13.8 µg/ml ($p < 0.01$) after 9 days and at the end of the experiment, respectively. For comparison, total PSA measured in animals with irradiated CWR22 tumors was 50.5 ± 10.7 µg/ml ($p = 0.02$) at day 9 and 75.8 ± 17.4 µg/ml ($p = 0.02$) at the completion of the experiment. In animals bearing CWR22c tumors, total PSA was reduced on all subsequent measurement days, with the decrease from day 9 to the end-point being significant for both control and irradiated animals (63.3 % decrease, $p < 0.01$ and 94.3 % decrease, $p = 0.01$, respectively). There was a significant positive correlation between total PSA and tumor volume ($r = 0.59$, $p < 0.01$) (Figure 2b). The correlation was stronger for animals with CWR22 tumors ($r = 0.74$, $p < 0.01$) than for animals with CWR22c tumors ($r = 0.27$, $p = 0.03$). The correlation between total PSA and tumor volume was strong for both CWR22 and CWR22c tumors when only subjecting control tumors to analysis ($r = 0.74$, $p < 0.01$ and $r = 0.73$, $p < 0.01$, respectively).

Qualitative assessment of DCE MRI

An example of an anatomical T1-weighted MR image through the centre of a tumor and matched slice of K^{trans} are shown in Figure 3a. The black areas within the tumor ROI are unfitted voxels. Rapid contrast enhancement was detected in the dynamic T1-weighted MR images in the peripheral regions of the tumors, whereas signal enhancement in central regions was slower. Within 20 minutes after contrast agent administration, wash-out of contrast agent was manifested for all tumors; however, pre-contrast signal intensity levels were not restored.

Treatment monitoring using DCE MRI

Figure 4 summarizes mean tumor K^{trans} prior to treatment and 1 and 9 days post-radiation, for CWR22 and CWR22c tumors. Pre-treatment K^{trans} was 47.1 % higher for CWR22c tumors compared to CWR22 tumors ($p = 0.01$). Following radiation, K^{trans} of CWR22c tumors was unchanged when comparing with pre-treatment values. Furthermore, there were no significant differences in K^{trans} between irradiated and control CWR22c tumors at days 1 or 9. For irradiated CWR22 tumors, K^{trans} was reduced by 45.7 % from day 0 to day 1 ($p = 0.04$), followed by an 87.7 % increase from day 1 to day 9 ($p = 0.01$). No significant day-to-day variations were found for the CWR22 control tumors. Parametrical K^{trans} maps from day 0, day 1 and day 9 of an irradiated CWR22 tumor are shown in Figure 3b.

The decrease in K^{trans} from day 0 to day 9 for control CWR22 tumors coincided with a 38.6 % increase in the fraction of unfitted voxels, giving a significant negative correlation between K^{trans} and the fraction of unfitted voxels for this group ($r = -0.79$, $p < 0.01$). K^{trans} was also negatively correlated to the fraction of unfitted voxels ($r = -0.61$, $p < 0.01$) when values from all tumors at all time-points were included in the analyses (Figure 5). Table 1 shows the fraction of unfitted voxels within each group at the time-points for DCE MRI.

Immunohistochemistry

Figure 6 shows triple immunofluorescent images of tumor tissue sections obtained from control and irradiated CWR22 tumors. Qualitative analysis revealed different microenvironmental characteristics between the two groups. Control tumors were well-vascularized with increased perfusion centrally, and hypoxia appeared equally distributed across the tumor. Radiation altered the vascular pattern, with large areas of hypoxia in the tumor core confining the vessels.

Discussion

In the present study, we have shown that vascularization is different in androgen-sensitive CWR22 xenografts under androgen-exposed and androgen-deprived conditions and that the resulting PCa phenotypes have differential response to radiation.

CWR22c tumors in castrated animals had 47.1 % higher mean K^{trans} than CWR22 tumors in non-castrated animals. CWR22c tumors were included in the experiment 36 ± 4 days after castration of the animals and increased vascularization following castration is consistent with findings in other studies demonstrating elevated VEGF expression, microvessel density and vascular permeability (1, 16), all attributes affecting the K^{trans} measurement.

CWR22 tumors showed a 45.7 % decrease in K^{trans} one day after receiving a single radiation dose of 15 Gy, which might result from radiation-induced reductions in blood flow, endothelial surface area, and/or vessel permeability. Together these factors contribute to compromised inflow of contrast agent, thereby leading to slowly- or non-enhancing regions in DCE MRI and reduced tumor K^{trans}. We hypothesize that this decreased K^{trans} might be related to increased hypoxia, as immunohistochemical staining of tumor tissue sections showed increased areas of hypoxia in irradiated CWR22 tumors compared to the control counterpart. The irradiated tumors showed a more centrally distributed hypoxic pattern surrounding blood vessels, as opposed to the more peripheral and equally distributed hypoxia in the control tumor. Thus, the low K^{trans} values one day post-radiation might reflect reduced blood flow, and impaired oxygen- and nutrient supply corresponding to increased levels of hypoxia.

Following radiation, no significant vascular changes were observed in CWR22c tumors. Such lack of response is also observed in PCa patients receiving radiation therapy when the androgen-resistant phenotype develops. It has been proposed that ADT induces acute hypoxia (17, 18). Then, the radioresistant appearance of these tumors, as demonstrated by the persistently high K^{trans} values, could be the result of CWR22c tumors already being hypoxic at the time of radiation. Hypoxia creates a microenvironment in which tumor cells become less dependent on angiogenesis and more resistant to apoptosis (19), and the presence of hypoxia has been suggested to be an important factor in PCa progression by protecting against tumor cell eradication (20).

In our study, fit failures were set to zero and included in calculation of mean tumor K^{trans}. It has previously been shown that the fraction of fit failures is strongly correlated to tumor necrosis and, oppositely, that exclusion of fit failures from mean tumor K^{trans} calculation eliminates this correlation (21). Thus, by excluding fit failures, the K^{trans} is essentially determined from the viable tumor rim, excluding necrotic hypoperfused cores resulting from successful treatments. Bradley *et al* (21) and Galbraith *et al* (22) proposed that these post-therapy low-enhanced voxels can be a useful non-invasive biomarker of tumor necrosis, providing support for including these voxels in our K^{trans} calculation.

K^{trans} values were negatively correlated to the fraction of unfitted voxels, which can be attributed to treatment-induced increases in necrosis or tumor size-dependent increases in necrosis for untreated tumors, expelling well-vascularized tumor regions and reducing blood flow. The significant increase in the fraction of unfitted voxels in irradiated CWR22 tumors from day 0 to day 1 may also reflect elevated hypoxic fractions, as observed in the immunohistochemical stains.

The model of Tofts and Kermode assumes the contrast agent to be instantly mixed in the plasma. In our experimental study, this assumption is reasonable as the blood circulation time in mice is short relative to the injection time. The use of K^{trans} as a measure of vascularization also assumes that blood flow is not limited and that flow is always greater than permeability (8). Thus, especially for large tumors with necrotic cores or irradiated tumors, precaution should be taken when analyzing and interpreting results. However, much of the low flow areas in the center of the tumors were unfittable, and thus, this is taken into account by including these voxels in the mean tumor K^{trans} calculations.

In this study we found that total PSA in CWR22 xenografts was positively correlated to tumor volumes. Furthermore, blood levels of PSA were decreasing following ADT. This is in accordance with findings from other groups using CWR22 xenografts in preclinical studies (11, 23). The use of functional imaging technologies, such as positron emission tomography (PET) and MRI, has revealed that changes in tumor biology and physiology precede changes in PSA. The rapid post-radiation decrease of K^{trans} in our CWR22 tumors was not coinciding with decreased PSA values, suggesting the possible utility of K^{trans} as an early predictor of treatment response. Rather than showing reduced PSA values, the CWR22 tumors demonstrated a slow increase after radiation. This has also been shown by others (23), and is explained by that an eventual transient decrease in PSA could have been missed due to low time-resolution of PSA measurements. However, the increase in K^{trans} of CWR22 tumors at day 9 fits with the increased PSA.

The CWR22 xenograft model is derived from the primary tumor in a patient with metastatic PCa (11, 12, 24), providing a valuable model of the clinical situation of PCa since this xenograft regresses following ADT and shows stability before recurring growth in the androgen-resistant state is evidenced.

Our interest in using DCE MRI to investigate the hemodynamic parameter K^{trans} was to make longitudinal, non-invasive measurements of tumor vascular characteristics following ADT by castration of the CWR22 PCa xenografts, which could preselect for differences in radiation outcomes. This imaging modality enables repeated monitoring and hopefully prediction of ADT and radiation treatment responses, providing additional contributions towards individualized cancer therapy. Future investigations are warranted to expand the present preclinical study into more advanced stages of PCa following ADT, and also incorporate investigations of the role of hypoxia in the transition from androgen-sensitive to androgen-resistant disease.

References

1. Nicholson B, Theodorescu D. Angiogenesis and prostate cancer tumor growth. J Cell Biochem 2004; 91:125-50.
2. Westin P, Stattin P, Damber JE, Bergh A. Castration therapy rapidly induces apoptosis in a minority and decreases cell proliferation in a majority of human prostatic tumors. Am J Pathol 1995;146:1368–75.
3. Pollack A, Joon DL, Wu CS, et al. Quiescence in R3327-G rat prostate tumors after androgen ablation. Cancer Res 1997,57:2493-2500.
4. Loncaster JA, Carrington BM, Sykes JR, et al. Prediction of radiotherapy outcome using dynamic contrast enhanced MRI of carcinoma of the cervix. Int J Radiat Oncol Biol Phys 2002;54:759-67.
5. Røe K, Muren LP, Rørvik J, et al. Dynamic contrast enhanced magnetic resonance imaging of bladder cancer and implications for biological image-adapted radiotherapy. Acta Oncol 2008;47:1257-64.
6. Lee AK. Radiation therapy combined with hormone therapy for prostate cancer. Semin Radiat Oncol 2006;16:20-8.
7. Widmark A, Klepp O, Solberg A, et al. Endocrine treatment, with or without radiotherapy, in locally advanced prostate cancer (SPCG-7/SFUO-3): an open randomised phase III trial. Lancet 2009;373:301-8.
8. Tofts PS, Brix G, Buckley DL, et al. Estimating kinetic parameters from dynamic contrast-enhanced T1-weighted MRI of a diffusible tracer: Standardized quantities and symbols. J Magn Reson Imaging 1999;10:223-32.

9. Tofts PS, Kermode AG. Measurement of the blood-brain barrier permeability and leakage space using dynamic MR imaging. 1. Fundamental concepts. Magn Reson Med 1991;17:357-67.

10. Larsson HB, Stubgaard M, Frederiksen JL, et al. Quantitation of blood-brain barrier defect by magnetic resonance imaging and gadolinium-DTPA in patients with multiple sclerosis and brain tumors. Magn Reson Med 1990;16:117-31.

11. Wainstein MA, He F, Robinson D, et al. CWR22: androgen-dependent xenograft model derived from a primary human prostatic carcinoma. Cancer Res 1994;54:6049-52.

12. Nagabhushan M, Miller CM, Pretlow TP, et al. CWR22: the first human prostate cancer xenograft with strongly androgen-dependent and relapsed strains both in vivo and in soft agar. Cancer Res 1996;56:3042-6.

13. Seierstad T, Røe K, Høvik B. Construction of a modified capacitive overlap MR coil for imaging of small animals and objects in a clinical whole-body scanner. Phys Med Biol 2007;52:N513-22.

14. Hittmair K, Gomiscek K, Langenberger K, et al. Method for the quantitative assessment of contrast agent uptake in dynamic contrast-enhanced MRI. Magn Reson Med 1994;31:567-71.

15. Schuuring J, Bussink J, Bernsen HJJA, Peeters W, van der Kogel AJ. Effect of carbogen breathing on the radiation response of a human glioblastoma xenograft: Analysis of hypoxia and vascular parameters of regrowing tumors. Strahlenther Onkol 2006;182:408-14.

16. Jain RK, Safabakhsh N, Sckell A, et al. Endothelial cell death, angiogenesis, and microvascular function after castration in an androgen-dependent tumor: Role of vascular endothelial growth factor. Proc Natl Acad Sci 1998;95:10820-25.

17. Rothermund CA, Gopalakrishnan VK, Eudy JD, Vishwanatha JK. Casodex treatment induces hypoxia-related gene expression in the LNCaP prostate cancer progression model. BMC Urol 2005;5:5.

18. Goonewardene TI, Sowter HM, Harris AL. Hypoxia-induced pathways in breast cancer. Microsc Res Tech 2002;59:41-8.

19. Woodward WA, Wachsberger P, Burd R, Dicker AP. Effects of androgen suppression and radiation on prostate cancer suggest a role for angiogenesis blockade. Prostate Cancer Prostatic Dis 2005;8:127-32.

20. Marignol L, Coffey M, Lawler M, Hollywood D. Hypoxia in prostate cancer: A powerful shield against tumour destruction? Cancer Treat Rev 2008;34:313– 27.

21. Bradley DP, Tessier JJ, Ashton SE, et al. Correlation of MRI biomarkers with tumor necrosis in Hras5 tumor xenograft in athymic rats. Neoplasia 2007;9:382-91.

22. Galbraith SM, Maxwell RJ, Lodge MA, et al. Combretastatin A4 phosphate has tumor antivascular activity in rat and man as demonstrated by dynamic magnetic resonance imaging. J Clin Oncol 2003;21:2831-42.

23. Dyke P, Zakian KL, Spees WM, et al. Metabolic response of the CWR22 prostate tumor xenograft after 20 Gy of radiation studied by 1H spectroscopic imaging. Clin Cancer Res 2003;9:4529-36.

24. Pretlow TG, Wolman SR, Micale MA, et al. Xenografts of primary human prostatic carcinoma. J Natl Cancer Inst 1993;85:394-8.

Acknowledgement

We thank Professor E. Paus and coworkers at Central Laboratory, Department of Medical Biochemistry, Oslo University Hospital, for technical assistance with PSA analysis, and Professor F. Saatcioglu at Department of Molecular Biosciences, University of Oslo, for providing the CWR22 xenograft.

Tables

Table 1: Fraction of unfitted voxels from pharmacokinetic modeling

	Day 0	Day 1	Day 9
CWR22, C	17.5 ± 6.0 %	14.9 ± 4.4 %	24.2 ± 3.2 %
CWR22, IR	12.6 ± 3.2 %	*34.0 ± 7.2 %	†17.1 ± 3.2 %
CWR22c, C	16.9 ± 3.3 %	17.5 ± 3.1 %	19.7 ± 2.9 %
CWR22c, IR	13.4 ± 5.8 %	14.7 ± 6.0 %	25.5 ± 7.8 %

The fraction of unfitted voxels from Tofts and Kermode pharmacokinetic modeling of DCE MRI data for each group on the three imaging time-points. *The increase in the fraction of unfitted voxels from day 0 to day 1 in irradiated CWR22 tumors was significant (p = 0.02). †The increase in the fraction of unfitted voxels from day 1 to day 9 in irradiated CWR22 tumors was close to significant (p = 0.06). C = control tumors, IR = irradiated tumors receiving a single fraction of 15 Gy after the MRI at day 0, and 24 h before the MRI at day 1.

Figures

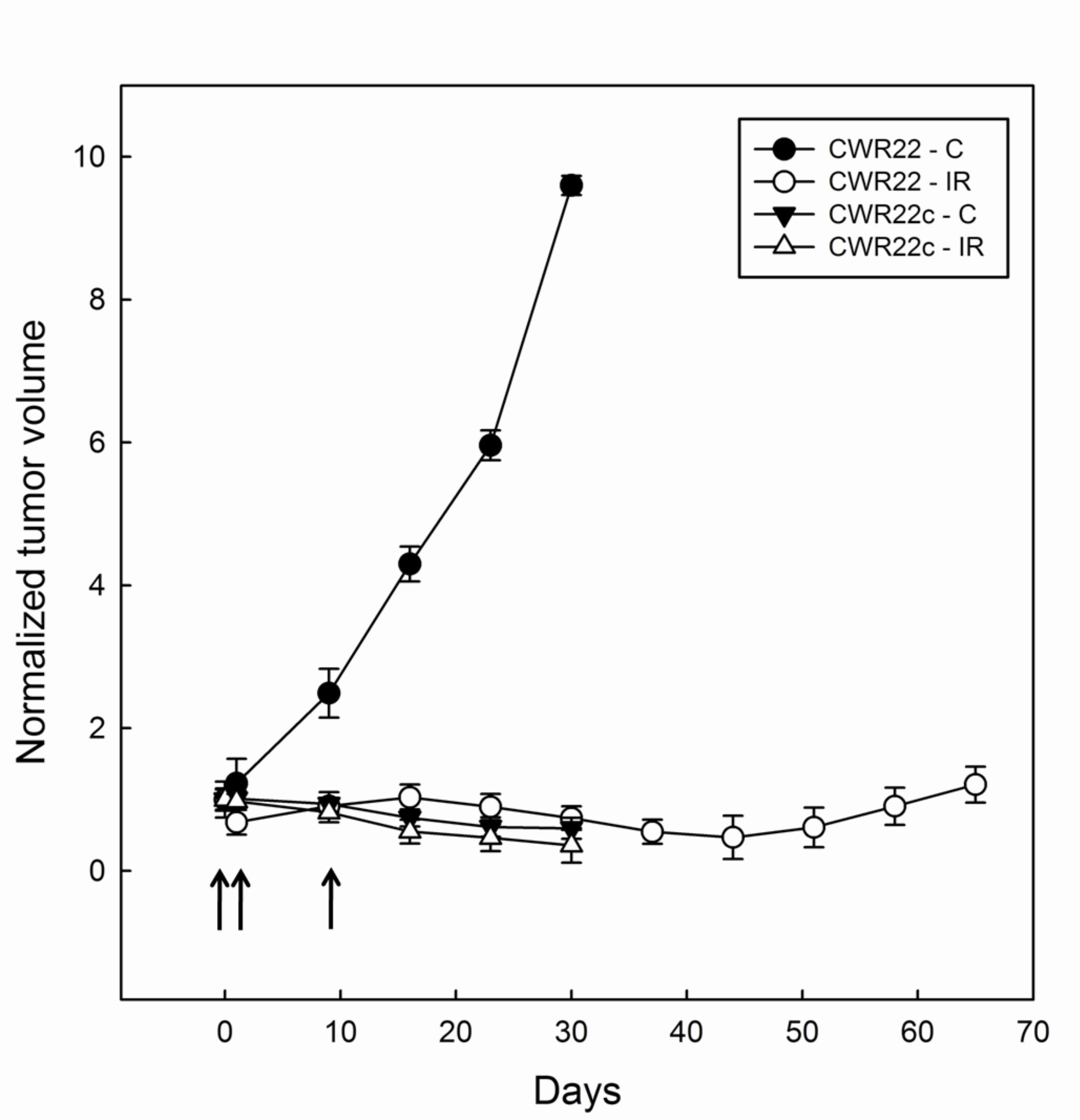

Figure 1: Tumor volumes of CWR22 and CWR22c normalized to day 0 (day of inclusion). Days for MRI are indicated by arrows. Each time-point represents normalized mean and SEM values. C = control tumors, IR = irradiated tumors receiving a single fraction of 15 Gy after the MRI at day 0.

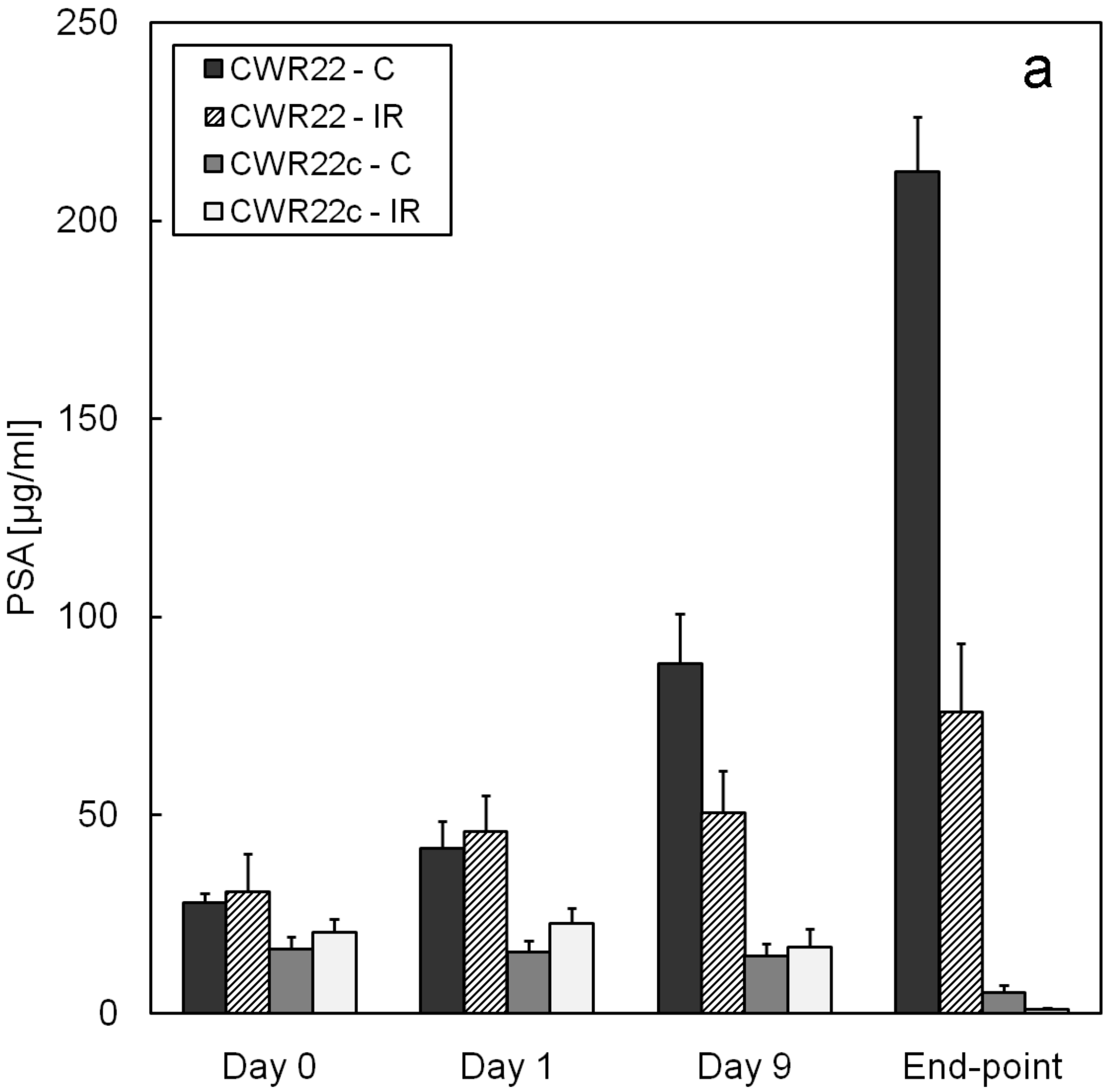
250
200
150
100
50
0
PSA [µg/ml]
■ CWR22 - C
▨ CWR22 - IR
■ CWR22c - C
□ CWR22c - IR
a
Day 0
Day 1
Day 9
End-point

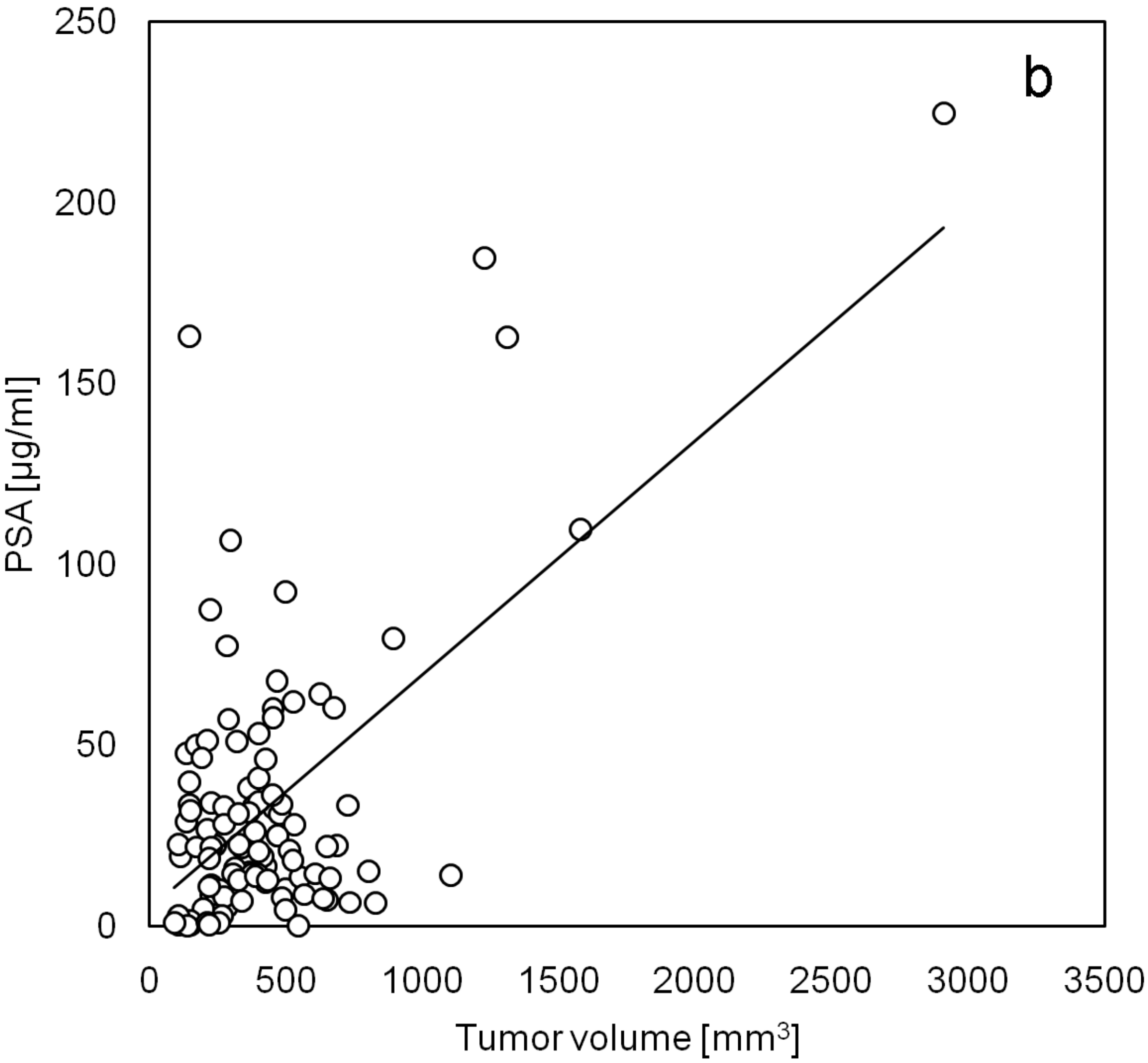

Figure 2: Total PSA in blood (mean ± SEM) at days 0, 1, 9 and the end of the experiment for the four treatment groups (a). C = control tumors, IR = irradiated tumors receiving a single fraction of 15 Gy after the MRI at day 0. Total PSA in blood versus tumor volume ($r = 0.59$, $p < 0.01$) (b).

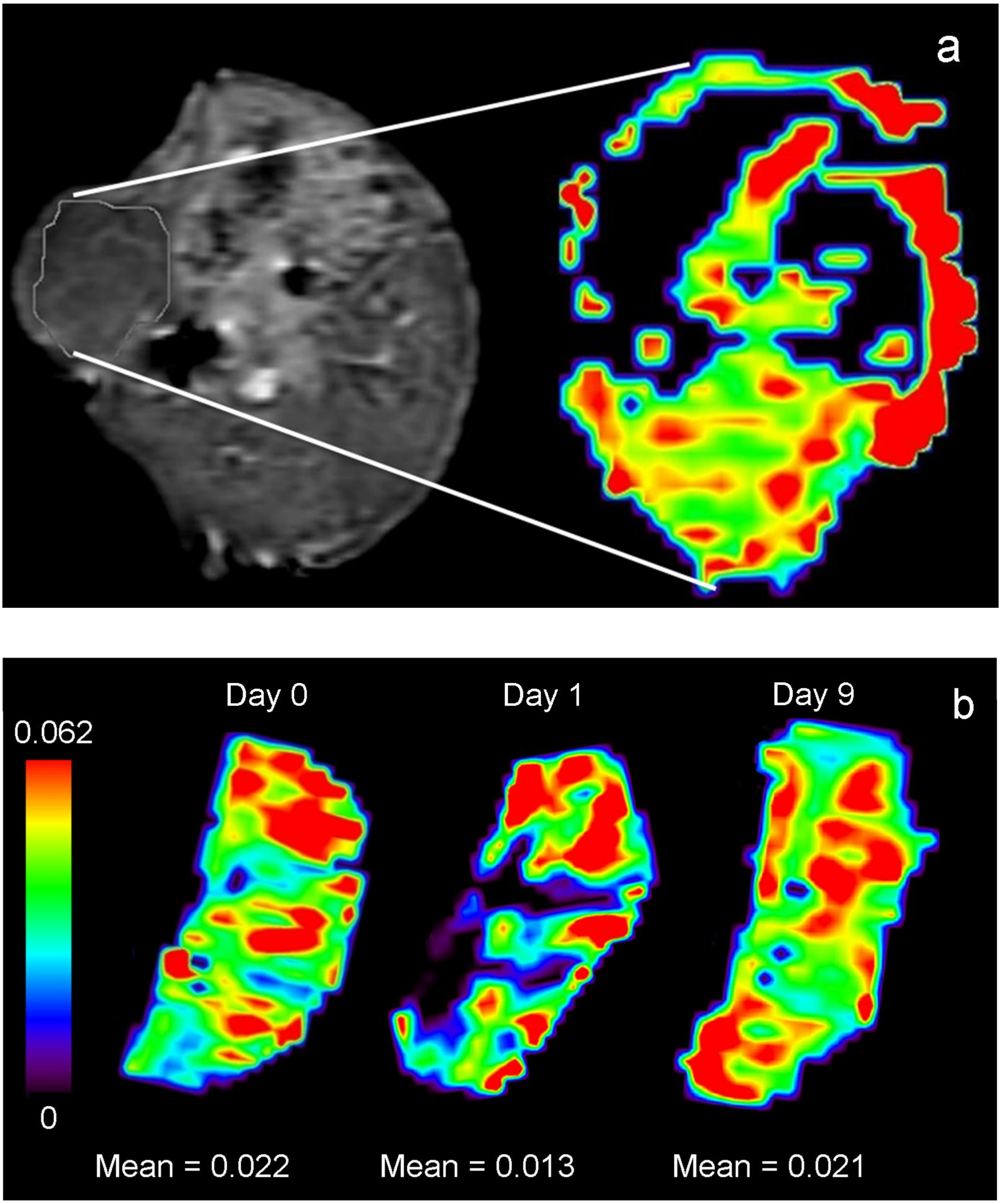

Figure 3: Anatomical T1-weighted image through the centre of a CWR22 tumor with illustration of the delineation of tumor ROI, and the corresponding K^{trans} ($\times 10^{-3}$ s^{-1})

parametrical map within the selected ROI. The black areas within the tumor ROI are unfitted voxels (a). K^{trans} (× 10^{-3} s^{-1}) maps and mean values of a CWR22 tumor pre-radiation (day 0) and post-radiation (day 1 and day 9) (b).

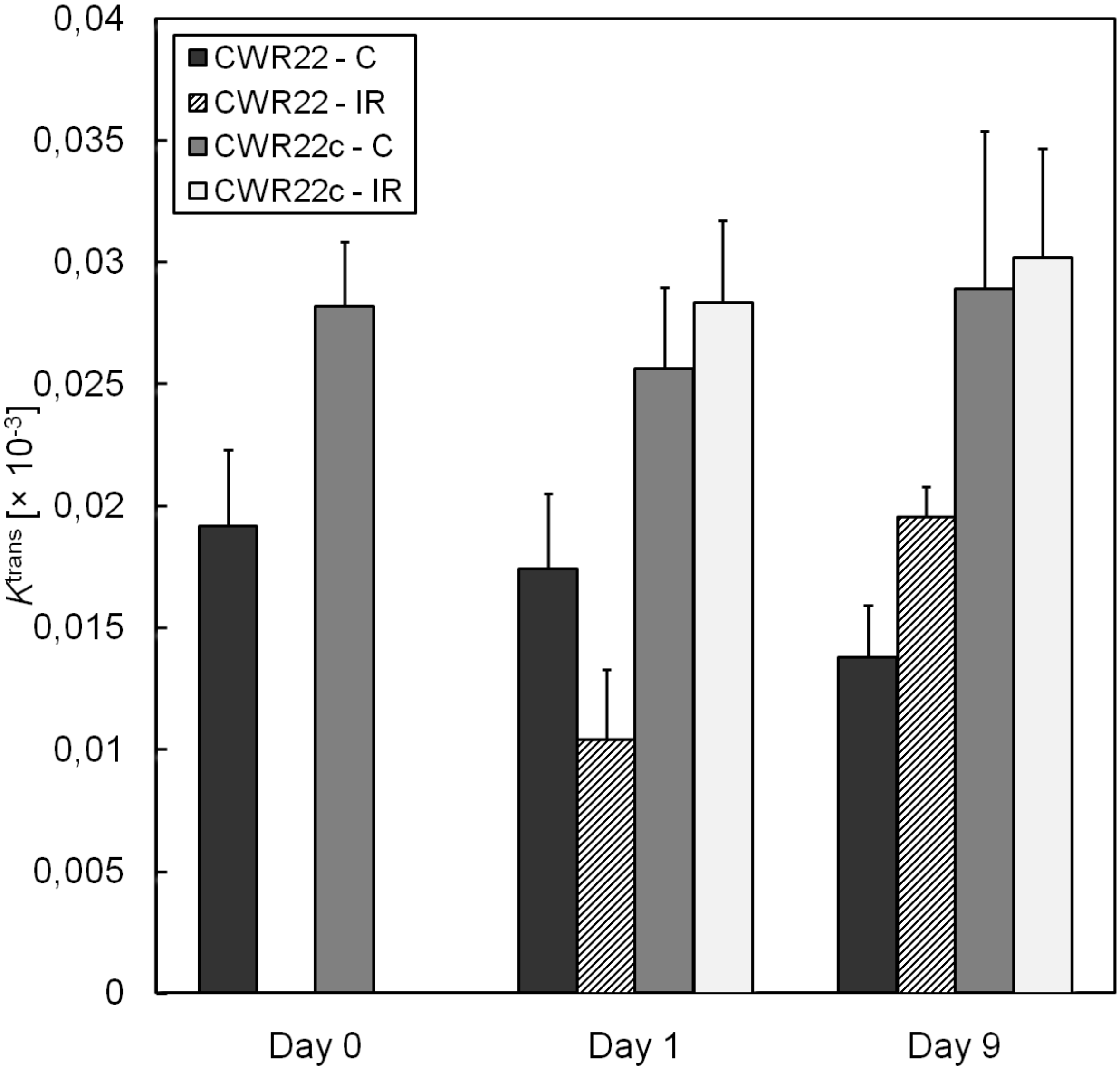

Figure 4: K^{trans} (mean ± SEM) values pre-radiation (day 0) and 1 and 9 days post-radiation. Bars on day 0 represent pre-treatment groups for 16 CWR22 tumors and 16 CWR22c tumors. Post-radiation, these groups are divided into four bars representing 8 tumors each. C = control tumors, IR = irradiated tumors receiving a single fraction of 15 Gy after the MRI at day 0.

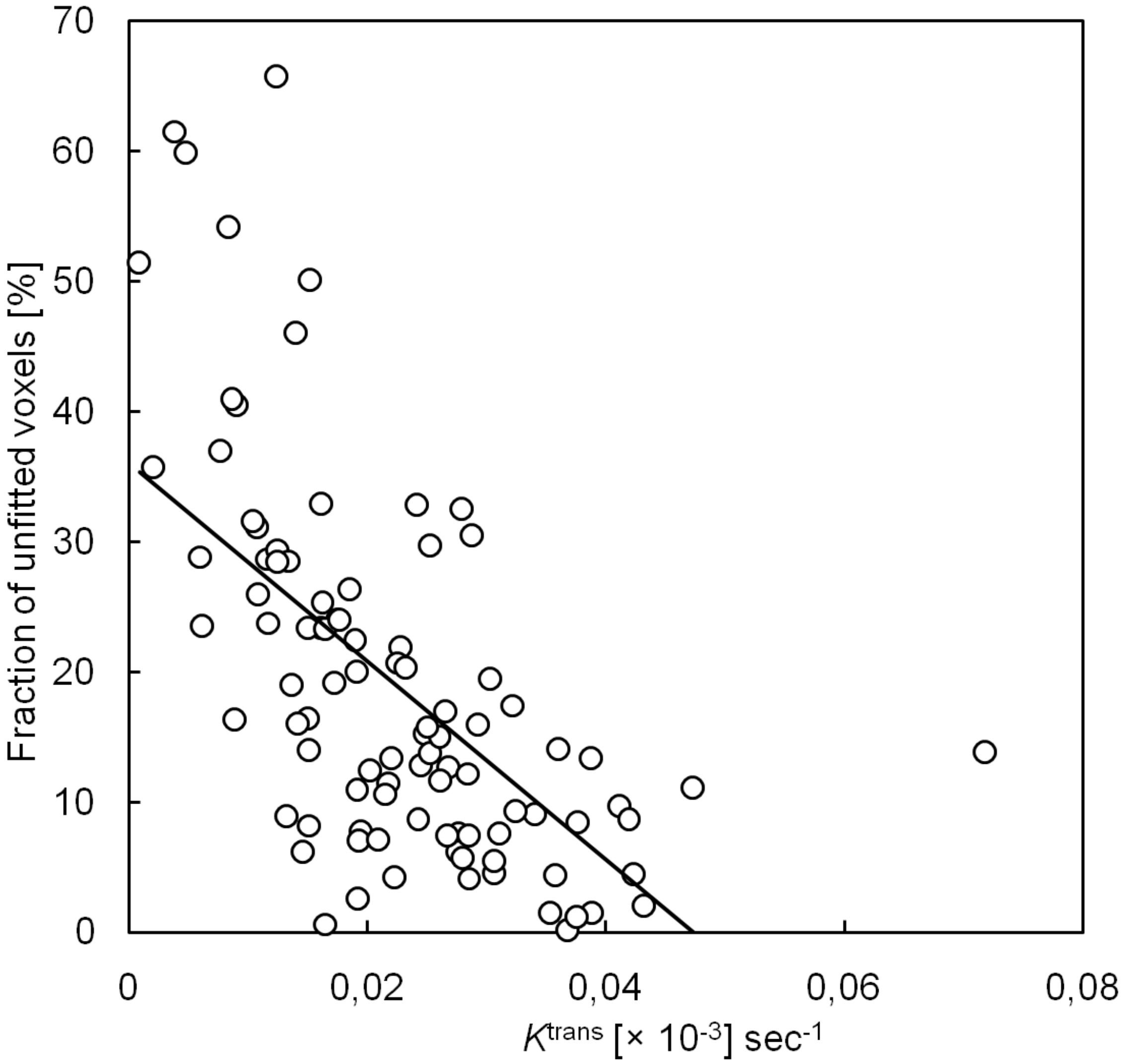

Figure 5: Correlation between the fraction of unfitted voxels and mean K^{trans} using all four treatment groups at all time-points ($r = -0.61$, $p < 0.01$).

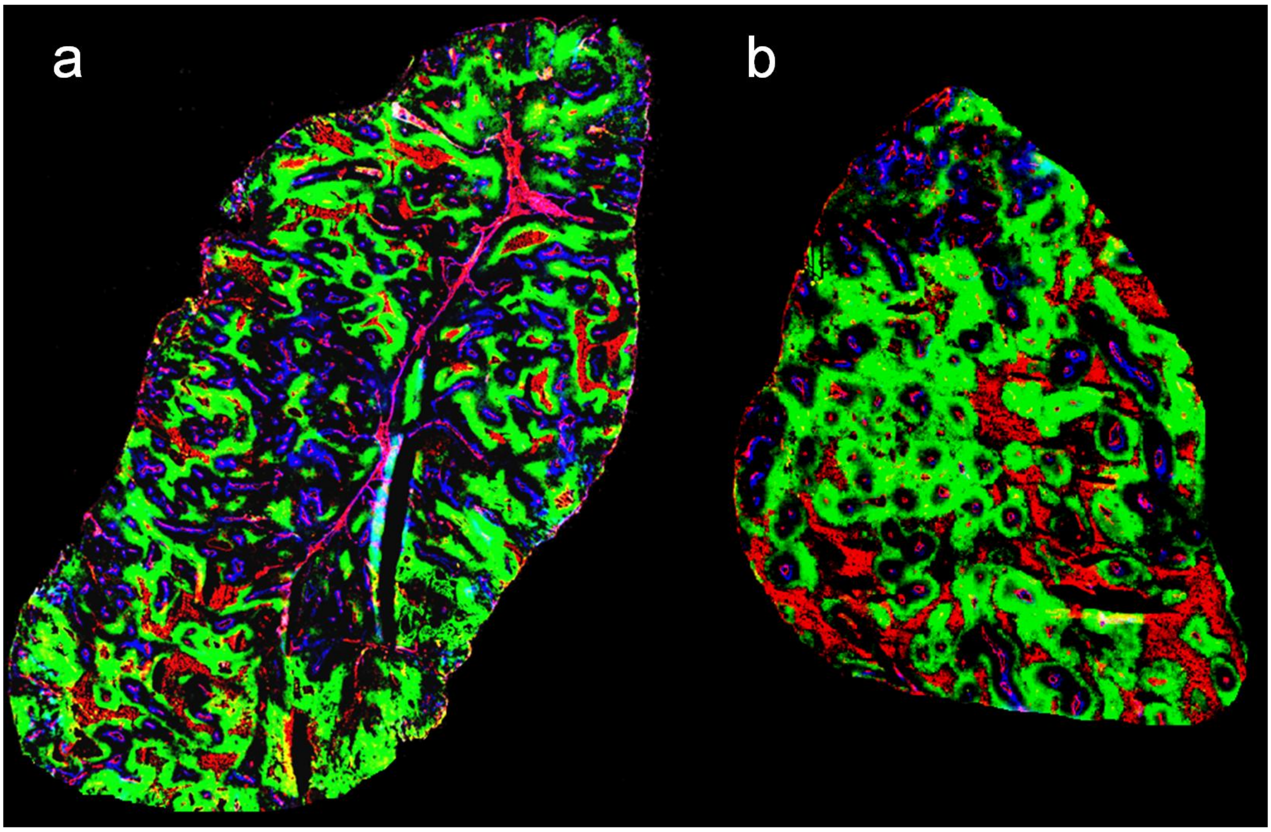

Figure 6: Triple immunofluorescent images showing vascular architecture (9F1, red), perfused vessels (Hoechst 33342, blue) and hypoxic areas (pimonidazole, green) in control (a) and 1 day post-radiation (b) CWR22 tumors.